TÉCNICO LISBOA

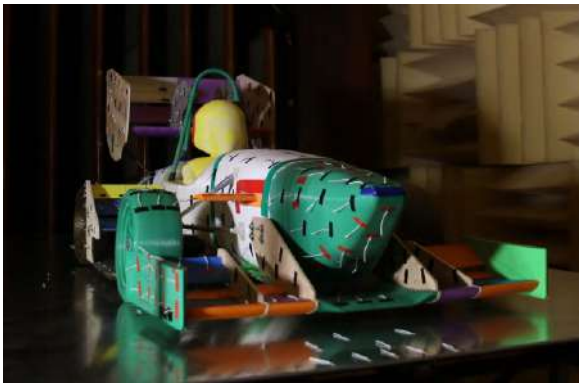

Wind Tunnel Testing of a Complete Formula Student Vehicle

Jaime Rafael Martins Pacheco

Thesis to obtain the Master of Science Degree in

Mechanical Engineering

Supervisor(s): Prof. André Calado Marta
Prof. Luís Rego da Cunha Eça

Examination Committee

Chairperson: Prof. José Manuel Da Silva Chaves Ribeiro Pereira
Supervisor: Prof. André Calado Marta
Member of the Committee: Prof. Edgar Caetano Fernandes

June 2022

Dedicated to my mother Glória

Declaration

I declare that this document is an original work of my own authorship and that it fulfills all the requirements of the Code of Conduct and Good Practices of the Universidade de Lisboa.

Acknowledgments

First of all, I would like to express my gratitude to both my supervisors, professor André Marta and professor Luis Eça, whose expertise were crucial in formulating the research. Your guidance pushed me forward and brought my work to a higher level.

I would also like to thank Formula Student Técnico, in particular the aerodynamics team members. A sincere thanks to Paulo Clemente for the help during the manufacture of the wind tunnel structures and the car model, and also during the wind tunnel experiments. I want to give a special thanks to my CNC saviours, José Luciano and Rodrigo Ferreira, I would be still trying to machine the plates without your insight. A special thanks goes towards Miguel Carreira and João Morgado for helping me with their CFD skills. I also want to express my eternal gratitude to Tiago Rocha and António Oliveira for being available whenever problems related with the model manufacturing and balance setup came up.

Several people deserve a special mention for the materials and qualified labour provided. A special thanks goes towards professor Luís Sousa and researcher Sérgio Gonçalves (*Laboratório de Biomecânica dos Tecidos e Biomateriais* supervisors) for guiding me throughout the wind tunnel model manufacturing and for providing access to the 3D printers and materials. Thanks to Pedro Alves, the supervisor of *Laboratório de Turbomáquinas*, for his guidance and support manufacturing the wind tunnel supports and testing model. Finally, I would also like to thanks professor Agostinho Fonseca and professor Ana Carrelhas for the guidance and apparatus provided to perform the wind tunnel tests.

My biggest gratitude goes towards my family, particularly to my mother Glória Frade, for the uncountable support throughout, not only this work, but also my whole life. My achievements would not be possible without your love. In addition, I must express my gratitude to my sister Elisa Pacheco for her valuable grammar corrections and assistance during these long months, your support meant the world to me. Finally, to my girlfriend Mafalda Cardoso, I will always be grateful for your unconditional support and encouragement.

Resumo

A aerodinâmica tem se tornado um pilar cada vez mais forte na performance dos carros de *Formula Student*. Para desenvolver um pacote aerodinâmico não basta desenhar conceitos, mas também é necessário serem avaliados através de modelos numéricos (CFD) e físicos (túneis de vento ou testes em pista). Normalmente, a comparação de ambos modelos é deixada para segundo plano, deixando em dúvida a qualidade do modelo numérico.

Esta tese apresenta um primeiro trabalho de comparação das duas alternativas de modelação para o último carro projetado pela equipa da Formula Student Técnico: CFD e túnel de vento. O objetivo principal é a avaliação da qualidade das simulações numéricas através da verificação e validação. Respetivamente à verificação, os erros numéricos foram estimados através de um estudo de convergência de malha. Para a validação, um modelo do último protótipo com 1/3 de escala foi construído e testado. Os testes no túnel de vento permitiram não só obter as forças aerodinâmicas de interesse (*lift*, *drag* e *pitching moment*), mas também uma comparação da física simulada com métodos de visualização de escoamento.

Inicialmente, na caracterização do túnel de vento foram retiradas várias leituras de velocidade que permitiram uma primeira análise da qualidade das simulações numéricas.

Por último, o modelo foi testado em seis configurações diferentes. No geral, as tendências e sensitividades registadas no túnel de vento foram também captadas pelos métodos numéricos. Além disso, os fios de lã colocados no carro permitiram realçar a correlação fiável já mencionada.

As simulações numéricas provaram a sua utilidade no estudo do comportamento da performance aerodinâmica para diferentes geometrias. Mesmo assim, as simulações não apresentam resultados precisos por si só, os ensaios em túnel de vento revelaram ser essenciais para validar esses comportamentos.

Palavras-chave: Validação, Túnel de vento, Ensaios experimentais, Ensaios numéricos, Formula Student, Performance aerodinâmica

Abstract

Formula Student teams are putting a great effort into aerodynamics as it is an important feature to enhance car performance. They focus on designing the best aerodynamic concept through numerical simulations. Before being manufactured, the final concept should pass an experimental test phase which is usually overlooked but essential to build trust in the numerical results.

This work presents a first evaluation of the numerical methods adopted by the Formula Student Técnico team. The objective is to verify the quality of CFD results by using verification (quantification of numerical errors) and validation (quantification of modelling errors). First, the numerical errors were estimated through a mesh convergence analysis. Then, to validate the numerical models, a 1/3 scale model of the latest prototype FST10e was built and tested. The wind tunnel tests were performed not only to obtain measurements of quantities of interest (lift, drag and pitching moment) but also to evaluate the physics of the CFD simulations by using flow visualization techniques.

First, the wind tunnel facility was characterized by taking speed measurements inside its test section. The data was then used to perform an initial evaluation of the numerical simulations. Finally, the model was tested in six different configurations, in which aerodynamic forces were recorded. In general, the qualitative evaluation of the results revealed that the numerical simulations captured the experimental trends and the sensitivity of each coefficient studied. Also, wool tufts were used as a flow visualization technique, which enhanced the agreement between the numerical simulations and the wind tunnel testing.

Despite capturing the wind tunnel results trends and physics, the CFD simulations still need time investment and more testing to provide accurate data. However, they proved to be useful in assessing how the geometry changes affect the aerodynamic performance of the car.

Keywords: Validation, Wind tunnel, Experimental tests, Numerical simulation, Formula Student, Aerodynamic performance

Contents

List of Tables

List of Figures

Glossary

BC	Boundary Condition
CAD	Computer Aided Design
CAM	Computer Aided Manufacturing
CFD	Computational Fluid Dynamics
CNC	Computer Numerical Control
CoG	Center of Gravity
CoP	Center of Pressure
DES	Detached Eddy Simulation
DNS	Direct Numerical Simulation
EFD	Experimental Fluid Dynamics
FST	Formula Student Técnico
IST	Instituto Superior Técnico
LASER	Light Amplification by Stimulated Emission of Radiation
LiDAR	Light Detection and Ranging
MG	Moving Ground
PLA	Polylactic Acid
RANS	Reynolds-averaged Navier Stokes
RH	Ride Height
RPM	Rotations Per Minute
RW	Rotating Wheels
SST	Shear Stress Transport
TKE	Turbulent Kinetic Energy
TST	Total Solver Time

Chapter 1

Introduction

This chapter introduces the work by providing a brief explanation related to the framework of the thesis and the expected deliverables and objectives. Finally, the thesis outline is presented to provide a better understanding of its structure.

1.1 Motivation

Since the beginning, competition motivates Humans to push boundaries to overcome barriers and opponents. As expected, with the first car also came the first race, giving birth to motorsport. As time progressed, various racecar systems evolved, supported by large investments.

In the late 1960s, aerodynamic devices were introduced in this industry, proving their value with significant lap time gains. Rapidly, aerodynamics took a big portion of racecar development, especially in the motorsport pinnacle, Formula 1.

In that early phase, on track tests were the only option to develop aerodynamic designs since computational capability was almost non-existent. Nevertheless, even with the substantial computational improvement, computational fluid dynamics (CFD) simulations still do not have the capability to entirely replace experimental tests.

CFD simulations are still not completely reliable on their own, they act as a complement to wind tunnel testing. However, the latter is the only reliable alternative to obtain experimental data that allows the assessment of the CFD modelling error. A wind tunnel recreates on track conditions in a controlled environment in such a way that it is possible to reproduce the different relative velocities between components. In other words, instead of having zero velocity, the air motion simulates the movement of the car. Moreover, the testing facilities can be complemented with a moving ground providing rotational motion to the model wheels, to recreate realistic on track conditions.

Usually in motorsport, wind tunnel tests uses racecar models to reduce costs, ease manufacturing and testing and also due to the limited test dimensions. Having customizable test conditions and advanced technologies makes it possible to acquire not only physical data (pressure readings, forces and moments sustained by the model surface, etc) but also information relative to the airflow around the

model by applying visualization techniques (tufts, smoke, etc). However, wind tunnel testing presents some limitations as well, which affect the results, such as scale effects, boundary conditions, etc. The limitations are discussed in detail in Sec. 2.3.

Formula Student Técnico (FST) is a racing team that competes globally with a formula like racecar against other university teams. Their car aerodynamics have been stagnated for a long time because CFD simulations and rare on track tests (with a lack of instruments) have been the only tools available for the team to develop the aerodynamics of its cars. As such, the motivation for this thesis is to test the newest racecar from FST in the aeroacoustic wind tunnel located at Instituto Superior Técnico (IST). In this way, not only can the team address the quality of its numerical simulations but also the wind tunnel instrumentation and setup will be updated to make feasible these new experimental works.

1.2 Formula Student

Formula Student is an international engineering competition where students are challenged to design, manufacture and compete with a single seater formula racecar, as illustrated in Fig. 1.1.

Figure 1.1: FST competing in Germany with the FST09e prototype.

The competition gave its first steps in 1981 (Formula SAE - Society of Automotive Engineers) with the first competition at the University of Texas in the United States of America. In 1998, the competition was brought to Europe caring some changes. Nowadays, there are several competitions around the world. Despite existing different rules, they are pretty similar allowing Formula Student teams to attend many competitions with few or even no changes to their prototype [1].

1.2.1 Formula Student Competition

Currently, the prototypes are divided into three categories: Combustion (FSC), Electric (FSE) and Driverless (FSD).

Constructing the fastest car is not enough to achieve top score since each competition is divided into static and dynamic events. Teams are awarded points according to their performance at the events.

There are three static events that evaluate the technical knowledge, economic and communication abilities [2]:

- Business Plan - present a business model for the prototype to a fictitious company, showing why their design fulfil the demands of the company, demonstrating its marketability;
- Cost and Manufacturing - approach the racecar design and manufacture from a financial perspective;
- Engineering Design - present the engineering process behind the car design.

The dynamic events are designed to put the cars to the limit. The racetrack performance of the cars are accessed at six events:

- Acceleration - the car accelerates over $75\,\mathrm{m}$ from a standing start;
- Skid Pad - the car drives an 8 figure circuit, intended to evaluate the lateral acceleration that the car is capable of reaching;
- Autocross - sprint race to demonstrate the maximum performance of the car;
- Endurance (Combustion and Electric only) - main race for FSE and FSC, a $22\,\mathrm{km}$ event where durability and reliability are tested;
- Track Drive (Driverless only) - main race for FSD, a 10 laps event;
- Efficiency - during the main events, the consumption of fuel or energy relative to speed is evaluated.

After each event, the teams are awarded points according to the competition score system (Tab. 1.1). Dynamic events are the main focus for the teams (675 points available) however, due to the variety of events, different philosophies are adopted by each team resulting in interesting car designs [2].

1.2.2 Aerodynamics of Formula Student Prototypes

In the last few years, aerodynamics took a fundamental share of the formula student racecar performance. Nowadays, almost every team develops an aerodynamic package to better balance the car and improve its handling. To do so, the downforce (negative lift force) is treated as a priority for the design of the devices, being the drag force considered secondary. It is usual to deal with downforce, drag and pitching moment values as dimensionless numbers, lift, drag and pitching moment coefficients, respectively,

$$C_L = \frac{L}{\frac{1}{2}\rho V^2 S}, \tag{1.1}$$

Table 1.1: Maximum points awarded for each event at Formula Student competition

	Event	FSC, FSE	FSD
Static	Business Plan	75	75
	Cost and Manufacturing	100	100
	Engineering Design	150	300
Dynamic	Accelaration	75	75
	Skid Pad	75	75
	Autocross	100	100
	Endurance	325	–
	Track Drive	–	200
	Efficiency	100	75
Total		1000	1000

$$C_D = \frac{D}{\frac{1}{2}\rho V^2 S}, \tag{1.2}$$

$$C_M = \frac{M_y}{\frac{1}{2}\rho V^2 S b}, \tag{1.3}$$

where L is the lift force, D is the drag force, M_y is the pitching moment[1], V is the uniform incoming airflow speed, ρ is the air density, S is the reference area and b the reference chord length.

Like every other system in the car, aerodynamic devices also have rules to comply too, which are shown in Fig. 1.2 in terms of allowable regions.

There are not two equal aerodynamic packages but, fundamentally, a Formula Student aerodynamic package is divided into four major sub-assemblies (Fig. 1.3):

- Front wing - located at the most forward point of the car, it creates downforce with a high efficiency value. Nevertheless, its main purpose is to redirect the air to the other aerodynamic devices in a beneficial way for the overall concept;
- Underbody - creates a low pressure underneath the car by accelerating the airflow and consequently sucking it to the floor. Usually, a diffuser is used at the back of the underbody promoting, even more, the airflow acceleration. Depending on the aerodynamic philosophy, the shape of the underside and the form of the diffusers vary;
- Side Elements - correspond to all elements on the side of the car, they produce downforce and redirect the airflow according to the aerodynamic design;
- Rear Wing - the most rearward component that produces high downforce levels. Nonetheless, it also produces high drag due to its relative placement to the incoming airflow, leading to a small efficiency.

[1] In this work, the pitching moment was calculated around the model-balance support, refer to Sec. 3.2.1.

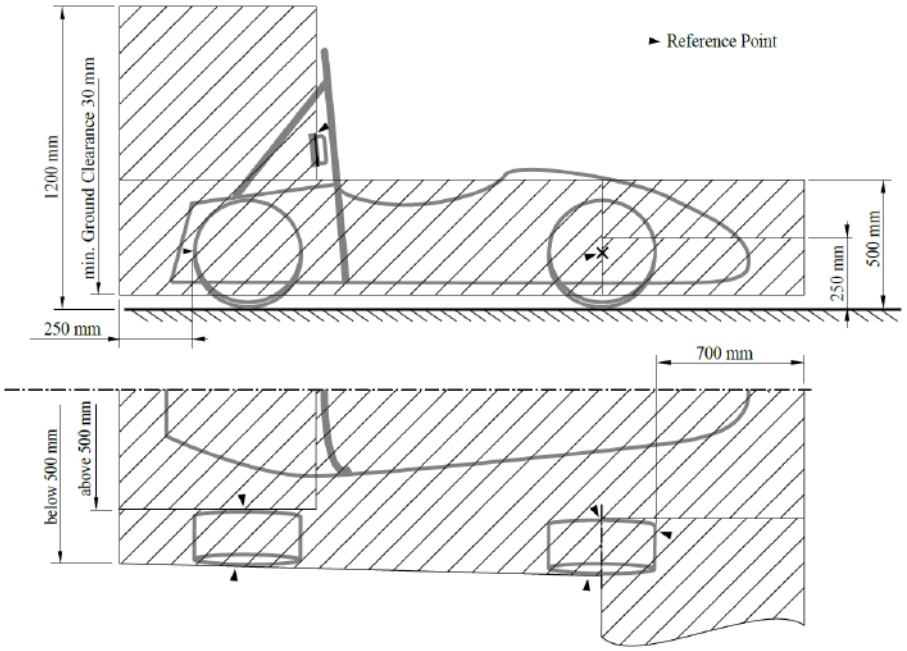

Figure 1.2: Maximum dimensions and positioning of aerodynamic devices [2].

Figure 1.3: Aerodynamic concept of the FST10e prototype.

1.2.3 Formula Student Wind Tunnel Testing

Generally, in the car industry, wind tunnel testing is quite usual even when competition is not involved. However, in Formula Student, it is seldom used so teams must blindly trust their CFD simulations.

Since CFD simulations emerged, huge developments were made. The improvement in numerical models and numerical techniques as well as the increasing computation capability raised the reliability and accuracy of the results. In CFD simulations, the governing transport equations are replaced by algebraic equations to obtain a numerical solution in space and time [3]. At this point, there are several models developed, each suited for a different problem. Thus, an experimental approach should be

considered to establish CFD as a trustful tool [4].

Wind tunnels are costly and complex facilities, so it is unusual for a group of students to get access. Nevertheless, in the last years, more teams are investing time and money to surpass this problem and build a trustful correlation between wind tunnel testing, CFD simulations and on track testing.

Formula Student Técnico

Until this point, the FST has already designed and developed 10 prototypes. However, only from the fifth car onwards, an aerodynamic package was integrated. Since then, the team has developed some knowledge in wind tunnel testing. However, these efforts have been intermittent over the years and wind tunnel testing was never a priority.

For the first ever wind tunnel experiment a 40% scale model of the rear wing was tested in the Low-Speed Wind Tunnel at IST (Fig. 1.4.(a)) to measure lift changes with increasing endplate size. The tests were made at $10\,\mathrm{m\,s^{-1}}$ which represented a 3.75 lower Reynolds number than what the wing was design for, this was appointed as the main cause for the unexpected results when compared to CFD simulations.

(a) Rear wing testing.

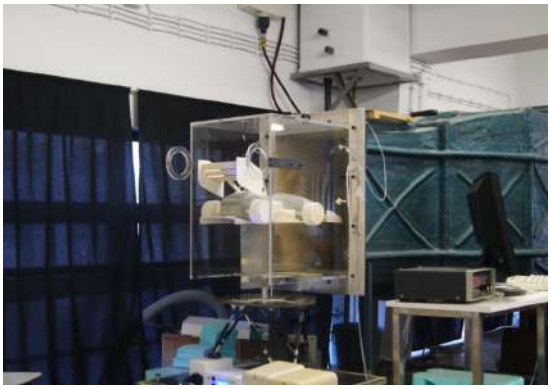

(b) Model testing.

Figure 1.4: FST06e wind tunnel testing.

Later, a 25% scale model of the complete FST06e was 3D printed (Fig. 1.4.(b)) and tested. Due to the low allowable weight of the aerodynamic force balance, the car model had to be printed with $1\,\mathrm{mm}$ thick surfaces, which caused further problems related to aeroelastic deformations.

Reenteam Uni Stuttgart

A Formula Student race car can be up to $3\,\mathrm{m}$ long, $1.5\,\mathrm{m}$ wide and $1.2\,\mathrm{m}$ tall, which reduces considerably the wind tunnels that have the capability to test it.

ReenTeam Uni Stuttgart was capable of testing their real racecar in a wind tunnel (Fig. 1.5) that was equipped with a moving ground and front wheels rotation. Both quantitative and qualitative tests were performed to correlate wind tunnel testing with CFD simulations. As presented by Racecar Engineering [5], deviations of 3% regarding the aerodynamic efficiency were obtained when compared to transient Detached Eddy Simulation (DES), although the value increases to 7% when compared to the

Figure 1.5: ReenTeam Uni Stuttgart wind tunnel testing to validate CFD and track data. From [5].

average steady state simulations. The next step was to compare the data gathered with on track testing. Analysing the the movement of the spring due to the aerodynamic forces, it was possible to estimate the vertical force (downforce) and the aerobalance[2]. For this study, the aero balance was evaluated with a change in a flap angle of attack (Fig. 1.6).

Overall the results of CFD and Wind tunnel testing present a high affinity with on track testing.

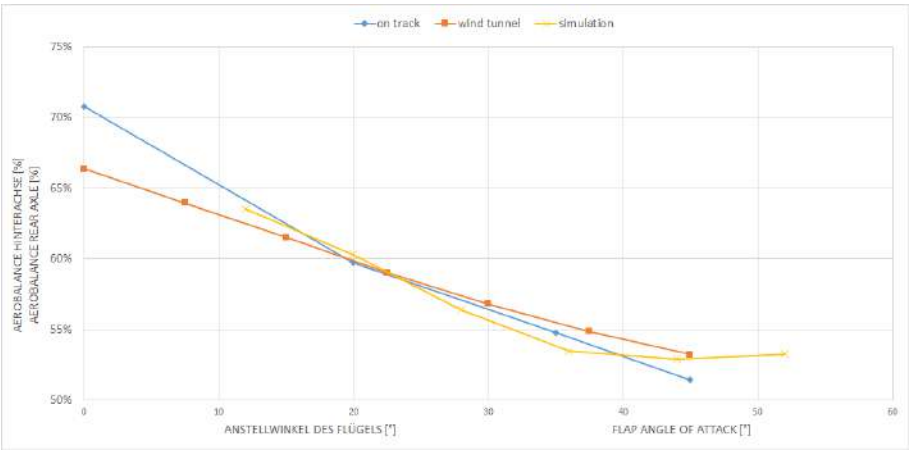

Figure 1.6: ReenTeam Uni Stuttgart comparison between CFD, wind tunnel testing and on track testing. From [5].

AMZ Racing

Partnering with *streamwise GmbH*[3], AMZ Racing tested its prototype in a Wind Tunnel with a procap system [6]. This component is a human operated hand-held probe that records instantaneous velocity fields while the system keeps track of the probe position (Fig. 1.7). With this data, it was possible to

[2]In motorsport typically aerobalance is defined as the percentage of the downforce acting on the front axle line
[3]Developers of ProCap System, a tool that measures 3D real time velocity measurements.

visualize flow fields in real time and consequently to map out streamlines and entire airflow sections (Fig. 1.8).

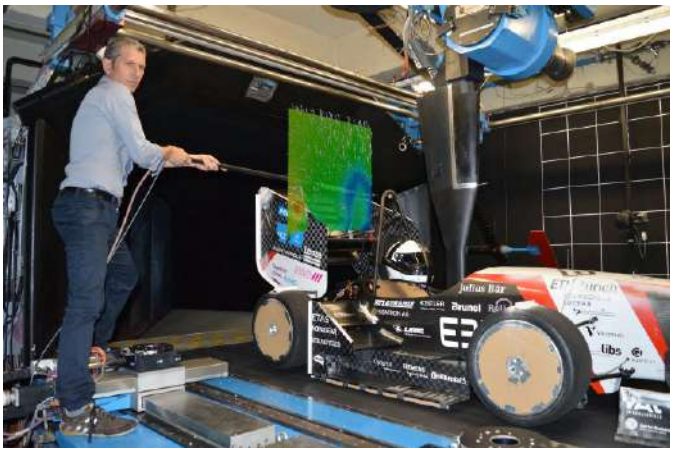

Figure 1.7: PropCap flow measurement using a tracking system by AMZ Racing. From [6].

Once again, CFD simulations used DES average over 1.2 seconds to take into account the transient behaviour of the airflow. Despite some local inconsistencies, the CFD matched the wind tunnel results.

Southampton University Formula Student Team (SSUFS)

The SSUFS constructed a modular wind tunnel model with built-in actuation to evaluate the aerodynamic concept across several configurations achieved during on track testing [7]. Through CFD studies, the blockage effects were taken into special attention to define a scale for the model taking also into account that the model would protect the data acquisition and motion systems.

Some sensitivity studies were performed to understand which car behaviours variables have a large impact on the aerodynamic performance. A control system was developed to adjust the car roll, pitch and ride heights. Finally, a representative suspension was also developed to fully correlate to the real prototype. This model was a pioneer in the Formula Student universe (Fig. 1.9). Some tests were already performed, however, no results are available yet.

1.3 Objectives and Deliverables

Reviewing the investment of FST in wind tunnel testing, a long journey is still ahead to make this experimental process an indispensable tool for the team.

The main objective of this thesis is to close that gap by evaluating the quality of the numerical methods used by the team. To do it, a 1/3 scale model of the newest prototype (FST10e) should be manufactured and tested with different configurations. Thus, an experimental procedure must be formalized for future tests. This work redefines the beginning of the validation adventure for the FST aerodynamics, by running experimental tests in the Aeroacoustic wind tunnel in Aerospace Laboratory at IST. However, this facility is not intended/prepared to test racecars nor to recreate on track conditions. Naturally, the first step should be to upgrade the facility with the necessary tools for the experiments: an adjustable

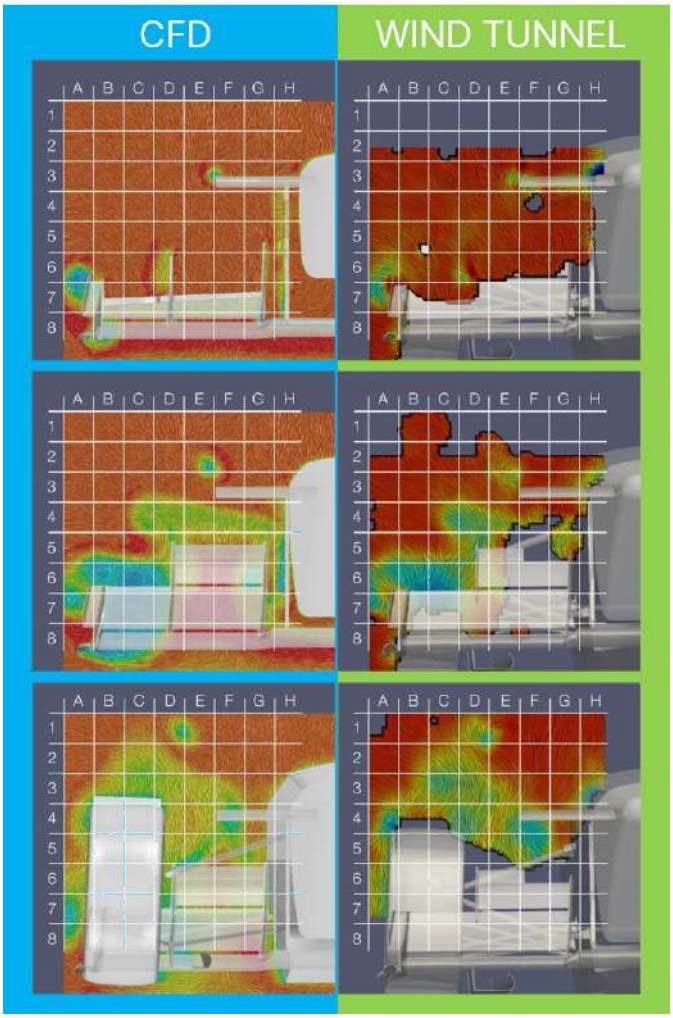

Figure 1.8: Total pressure comparison between CFD and wind tunnel testing in three consecutive planes by AMZ Racing. From [6].

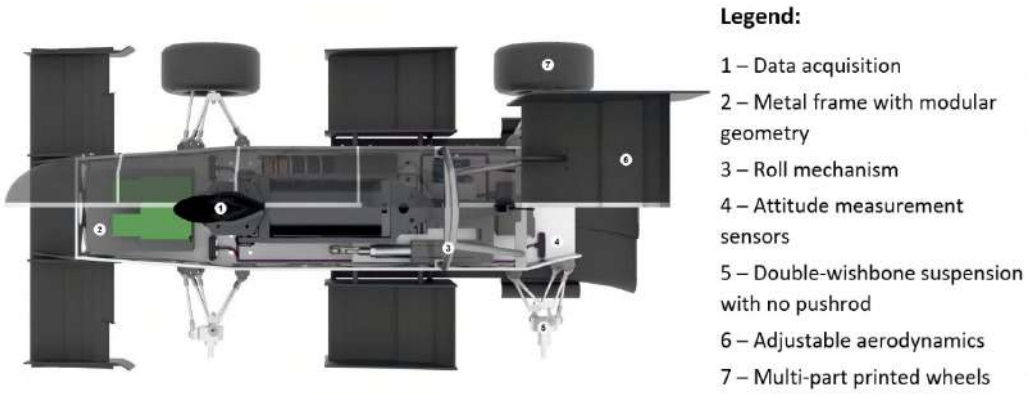

Figure 1.9: SSUFS wind tunnel model scheme. From [7].

frame to support the aerodynamic force balance and also a ground plate, which would allow the FST team to test different car configurations.

The expected deliverables of this thesis are:

- Correlation between wind tunnel and CFD - assessment of the numerical error present in the CFD

setup. Comparison between wind tunnel experimental loads and CFD simulations. Qualitative comparison between flow visualization tests with CFD simulations physics. Evaluation of the quality of the numerical simulations;

- Wind tunnel characterization (Anemometry) - perform a hot film anemometry to measure the velocity fluctuations in several sections. Obtain the velocity profile and the turbulence intensity along the test facility.
- Wind tunnel and parametric computer aided design (CAD) - a complete model of the wind tunnel test section and car model must be elaborated. The CAD should have adjustable parameters to enable the study of distinct car behaviours;
- Wind tunnel facility upgrade - an aerodynamic balance frame support should be built-in the concrete floor under the test section to minimize vibrations and deformations. Also, an adjustable support must be manufactured to enable tests with different apparatus;
- CFD setup - an automatic macro will be developed to simplify the setup process and to make the process less susceptible to errors. The macro script will have some inputs to define the wind tunnel conditions such as model scale, car speed, refinement index, and also it should export results data and figures;

1.4 Thesis Outline

This thesis is divided in six chapters.

Chapter One introduces the work that was performed as well as its objectives and deliverables.

Chapter Two contains the physical formulation for the development of this work as well as the description and characterization of the wind tunnel used for testing.

Chapter Three refers to the mathematical formulation of this thesis. The CFD setup is addressed, which includes the mathematical models and boundary conditions chosen, the mesh convergence and the assessment of the numerical error.

Chapter Four relates to the wind tunnel model manufacture as well as the studies that defined its scale and position within the airflow jet. A brief study of the structural integrity of the force balance is presented in this chapter too.

Chapter Five presents the qualitative comparison between the wind tunnel experiments and the CFD simulations. The numerical simulation quality is evaluated by flow visualization techniques and experimental aerodynamic loads.

Chapter Six concludes this work by presenting the Achievements and also the Future Work to improve the experimental tests.

Chapter 2

Wind Tunnel Model Testing

This work presents two different formulations to successfully achieve the objectives: one physical and another mathematical. This chapter covers the former which includes the wind tunnel testing and the theoretical fundamentals behind it. This background proves essential to justify the decisions taken throughout the wind tunnel preparation, the model manufacture and the experimental part.

2.1 Wind Tunnel

A wind tunnel is a facility that creates controlled environments to simulate real world aerodynamic conditions. Since on-road testing can be extremely expensive, wind tunnel testing began to gain a lot of momentum within the motorsport industry.

According to the airflow speed achieved inside the test section, a wind tunnel can be classified as low or high speed wind tunnel, depending on the Mach number,

$$Ma = \frac{V}{c} \quad c = \sqrt{\gamma_h RT}, \tag{2.1}$$

where V is the object velocity, c the speed of sound, γ_h the ratio of specific heats, R the gas constant and T is the gas temperature. Low speed wind tunnels operate at $Ma < 0.4$, which corresponds to a maximum velocity around $134\,\mathrm{m\,s^{-1}}$ (the speed of sound differs depending on the fluid medium, it is approximately $c = 343.3\,\mathrm{m\,s^{-1}}$ for dry air at 20 ℃). For this type of wind tunnels, is reasonable to consider constant air density [8].

A common wind tunnel scheme can be seen in Fig. 2.1, a fan motor drives the air throw the test section where the body of interest is located.

2.2 Wind Tunnel Type

Regarding the wind tunnel type, it can have open circuit or closed circuit.

In an open section wind tunnel (Fig. 2.2.a) the air follows a straight line from the entrance until the exit. It goes through a contraction section (nozzle) and a fan that can be located before or after the test

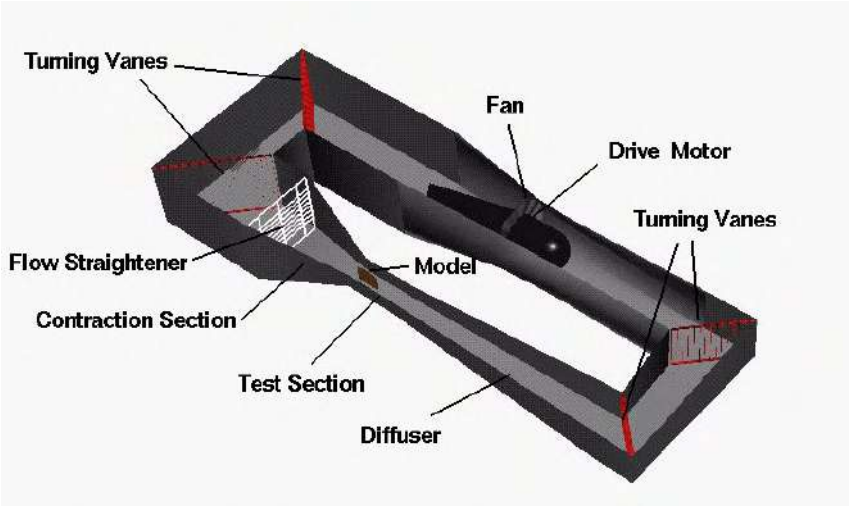

Figure 2.1: Wind tunnel general schematic. From [9].

section [8, 10].

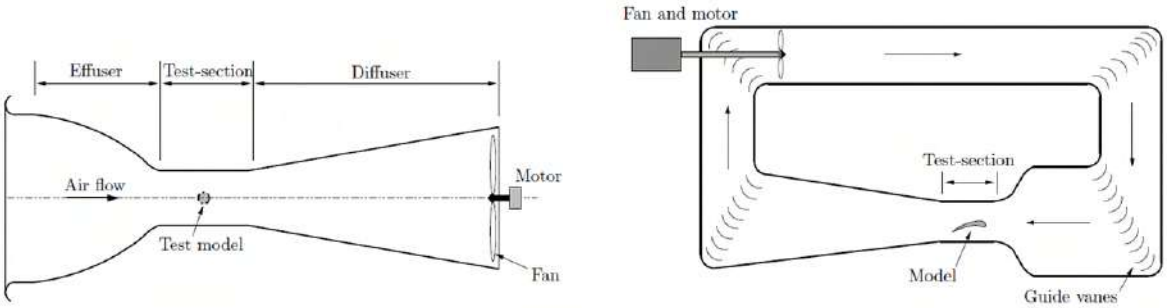

(a) Open return.

(b) Closed return.

Figure 2.2: Wind tunnel schematic. From [11].

The air in a closed section wind tunnel (Fig. 2.2.(b)) is continuously recirculated. This type of wind tunnel is more costly due to the different features/components necessary to achieve a high quality airflow. Generally, the air leaving the test section passes through a diffuser, fan and a nozzle before entering once again inside the test section. Turning vanes are used to promote a smoother airflow through the return duct corners resulting in higher flow quality [8].

2.3 Test Section Configuration

Considering the test section, a wind tunnel can have an open test section (open jet test section) or a closed test section.

Wind tunnels for automotive studies are designed to simulate the on-road performance. Nevertheless, it is impossible to achieve 100% accuracy on the results due to scale effects and boundary conditions. So, correction factors must be applied depending on the test section characteristics. Moreover, simulating on-road performance can be complicated since it is necessary not only to control the environmental conditions but also to measure the forces and moments produced by the model. For instance,

the major difficulties are the removal of the wind tunnel boundary layer, the wheel motion reproduction and its contact with the ground.

2.3.1 Road Representation and Boundary Layer Removal

When a car moves, in a region near the car surface the air becomes disturbed due to inertial and viscous forces. This region is a thin layer where speed is lower than the free-stream speed. On the road, the car is moving and the air has no relative motion to the ground. However, these conditions are impossible to replicate in a wind tunnel. Usually, the test section is used as a road (Fig. 2.3.(a)), where the car is stationary and it is the fluid that presents motion. Thus, the relative speed between the air and the ground is not zero anymore, a boundary layer is created and it interferes with the boundary layer created by the car. This produces a different flow field, particularly for models with low ground clearance and ground effect.

Several boundary layer control techniques were studied to remove or re-energize the boundary layer low momentum flow. At first, a moving belt (Fig. 2.3.(c)) that replicates a moving ground seems the ideal solution. Nonetheless, it can be costly and extremely complex, the model must have wheel motion[1] and the aerodynamic balance (used to measure the forces) has to be compatible with the moving ground.

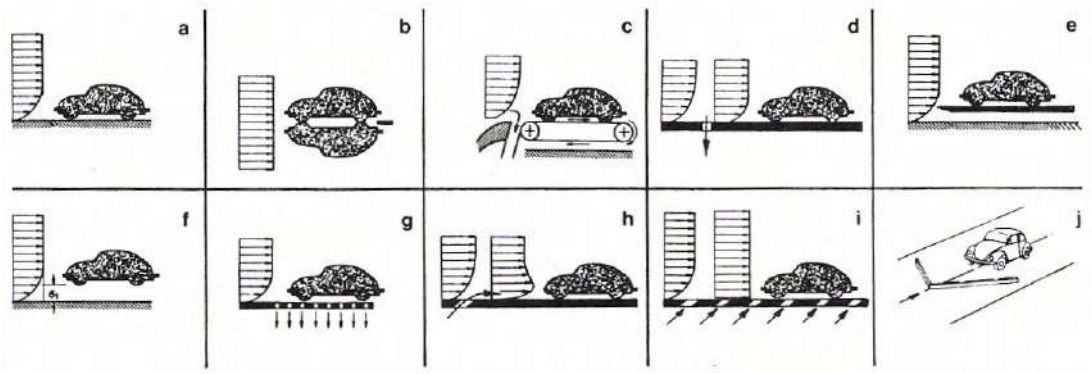

Figure 2.3: Boundary layer control system. From [12].

Other solutions can be used as Fig. 2.3 illustrates. Theoretically, the reflection model method (Fig. 2.3.(b)) should give a true representation of the on road airflow, but it is not used very often since two models and a large test section are required, which is costly. Another solution is to re-energize the boundary layer (Fig. 2.3.(h),(i)) using blowing systems to inject high momentum flow, inducing higher flow velocity near the wall than the free-stream. Also, suctions systems (Fig. 2.3.(d),(g)) are used to remove the floor boundary layer (low momentum airflow). Simpler solutions are also commonly used, disturbing the boundary layer with a fence (Fig. 2.3.(j)), an elevated model (Fig. 2.3.(f)) or the most common an elevated model with a ground plate (fig. 2.3.(e)) to reduce boundary layer.

Despite improving the test conditions, there will be differences regarding forces when comparing with on track results since the conditions related to the road (and the wheels) are not reproduced. Fago et al. [13] draw some conclusions related to ground effect in how ground clearance affects the forces of the

[1] If the model does not have the capability for wheel motion it can be elevated until the tyres do no contact with the moving ground. However, this brings other problems that can be resolved with correlations

vehicles when testing with a moving belt or a stationary ground underneath. Experiments illustrated in Fig. 2.4 conducted at $20\,\mathrm{m\,s^{-1}}$ revealed that, for short vehicles[2], at low clearances, the disparity of C_L and C_D is at the highest point, the fixed ground changes the flow field causing a higher lift and drag force. However, as the ground clearance increases, only the lift coefficient presents a noticeable discrepancy between both conditions.

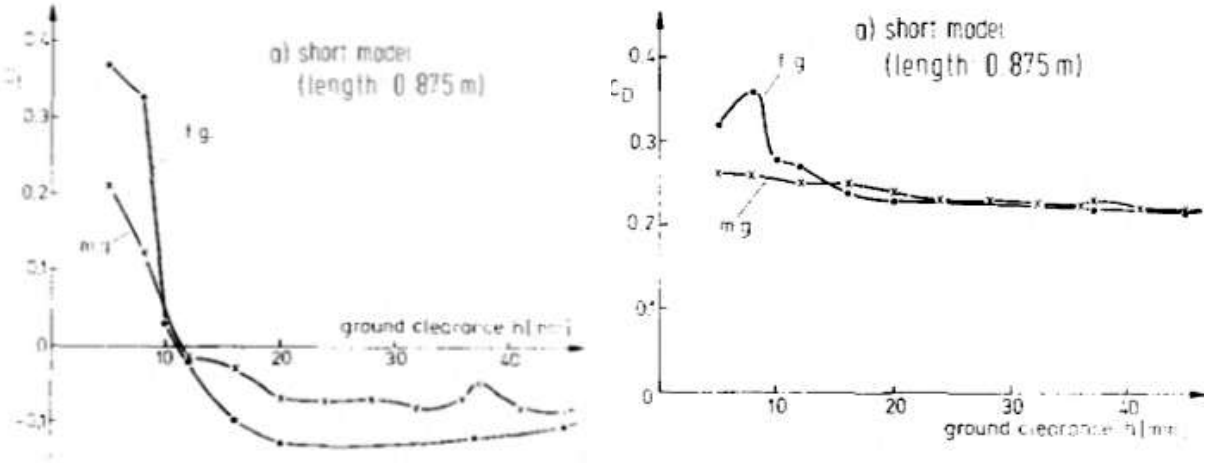

(a) Lift coefficient.

(b) Drag coefficient.

Figure 2.4: Lift and drag variation due to the ground clearance for a short model (length $0.875\,\mathrm{m}$) with a moving and fixed ground. From [13].

2.3.2 Reproduction of On Track Wheel Motion

In wind tunnel conditions, it is extremely difficult to reproduce the wheel performance seen on the road. There are two main forms to treat the wheel assembly: fixed or free suspension system. Regarding the latter, the system adopts a similar attitude as a real car, when the wheels are in contact with the ground, the tyres deform and the contact patch increases with speed. To recreate this feature in the wind tunnel, the wheels have to touch the ground and the contact patch forces must be measured.

If it is not possible to measure them, the wheels should be lifted off the ground (fixed suspension), creating a gap between the tyre and the ground. If not sealed properly, it interferes with the forces measured. The presence of a gap causes greater differences in pressure. Instead of higher pressure, the gap creates lower pressure in front of the wheel. However, when rotating motion is applied, it causes a lift change, from positive to negative (Fig. 2.5) [14].

Usually wheel motion is not taken into account during wind tunnel testing because its influence on the moments and forces acting on the vehicle is negligible. For open wheel cars, the rotating movement causes a forward displacement of the separation, which can be easily reproduced by adding a stall strip (Fig. 2.6).

[2]Definition given by Fago et al.[13] to a model with a length of $0.875\,\mathrm{m}$, which is close to the length of the FST10e model.

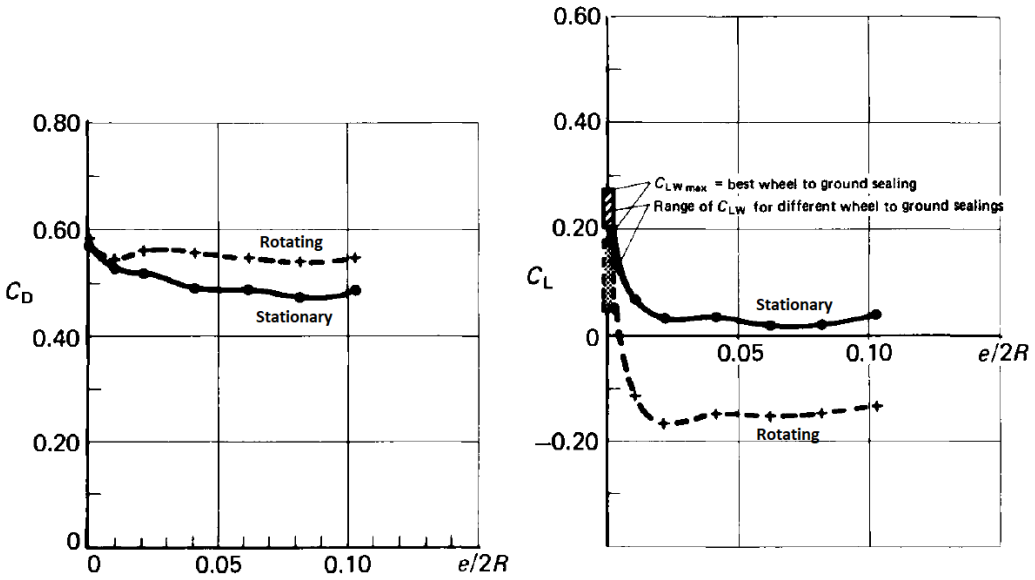

Figure 2.5: Drag and lift coefficients of a wheel in stationary and rotating conditions for different ground clearances. From [14].

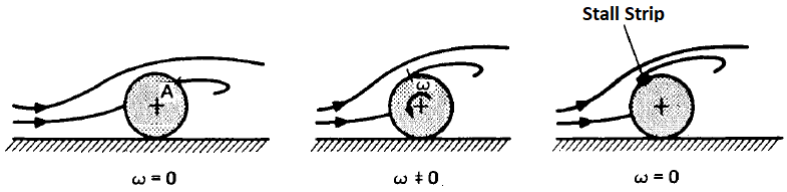

Figure 2.6: Reproducing air separation on a wheel by adding stall strip. From [14].

2.4 Wind Tunnel Airflow Characterization

Usually, anemometry is used to get fast-response velocity measurements in turbulent flows due to the low inertia. The probe can be a thin metal wire or film (Fig. 2.7), that has a high temperature coefficient of resistance.

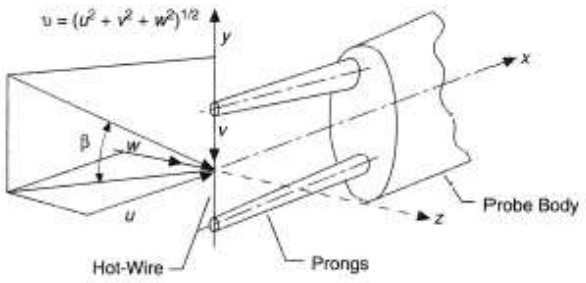

Figure 2.7: Hot wire anemometry sensor. From [15].

The resistance of the materials used for the sensors depends linearly on the temperature,

$$R_H = R_0[1 + \lambda(T_h - T_0)], \tag{2.2}$$

where R_H is the resistance at operating temperature T_h, R_0 the resistance at ice point temperature T_0 and λ the temperature coefficient of resistance. There are two types of anemometry: hot wire and constant temperature anemometry. During the anemometry process, the resistance is heated electrically to temperatures higher than the airflow. For the first type, when exposed to airflow, the hot wire loses heat, decreasing its temperature. By measuring it, it is possible to deduce the airflow speed. On the other hand, constant temperature anemometry has a similar principle, in order to maintain temperature and consequently the resistance, when exposed to increasing airflow speed, the electrical sensor current changes. The airflow speed can be obtained through the current variation measurement [14].

2.5 Aerodynamic Force Balance

An aerodynamic force balance measures the forces and moments acting on a body of interest during wind tunnel testing. To achieve high accuracy, the balance has to satisfy some requirements [14]: The balance should not interfere with the airflow (if a support is used, it is imperative to determine its influence); During tests, the model attachment should remain untouched; If the lift forces measured are much lower than the model weight, pre-loading should be compensated by tarring weights; If yaw tests are performed, the balance should rotate along with the model; The forces applied on the vehicle should be carried exclusively to the load sensors, so friction and hysteresis must be minimal.

Depending on the mounting location, balances can be external and internal being the former located outside the test section and the latter placed inside the test model.

The location of internal balances (Fig. 2.8.(a)) is a substantial advantage since they cause almost no interferences with the airflow. However, they increase the overall system complexity as they are manufactured to test a specific model. Indeed, the most common force balance is the six components external balance (Fig. 2.8.(b)), due to its versatility, it is possible to test distinct models without further modifications. The complexity of external balances resides in the model attachment and the number of measurements needed, which can vary between one and six for the most complex studies (three forces and three moments components).

Forces Measurements

Balances can have several designs and measurement channels depending on the test requirements and usually use strain sensors.

For aerodynamic purposes, the measurement of three forces (drag, side force and lift) and three moments (roll, pitch and yaw) are essential to characterize the race car performance (Fig. 2.9). Measuring the six components is not a trivial task and some care has to be taken: i) Loads have to be corrected due to model weight; ii) During wing tunnel tests, the model loads will increase approximately with the square of airflow speed. If the model is sustained by the wheel assembly, the ride heights will change not only with the model weight but also with the increasing vertical loads during testing. In this case, the force distribution in the two axles must be known to correct the model ride height. Otherwise, the angle of attack will change leading to variations of the aerodynamic coefficients [18].

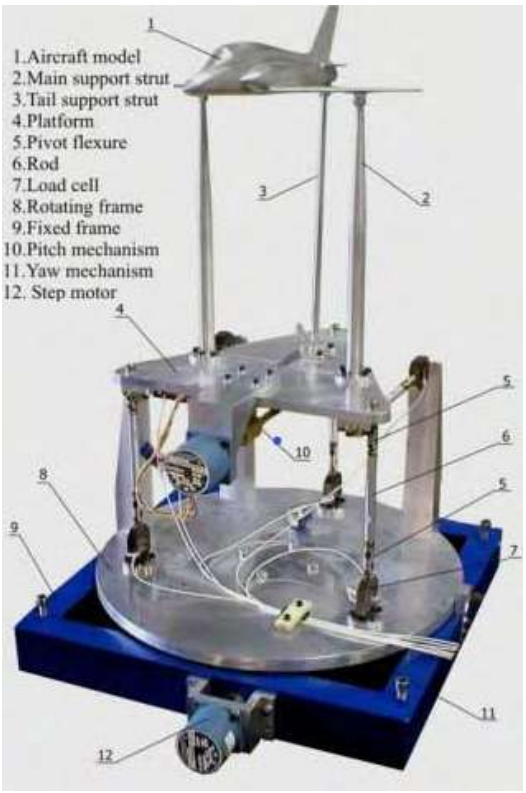

(a) External balance scheme. From [16].

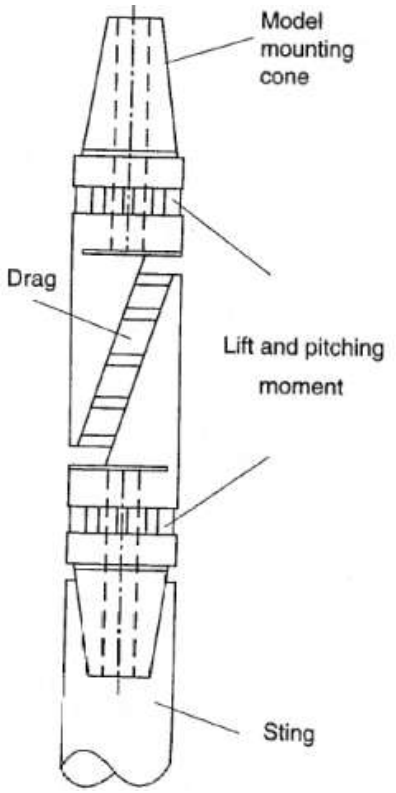

(b) Internal Balance scheme. From [17].

Figure 2.8: Aerodynamic wind tunnel balances.

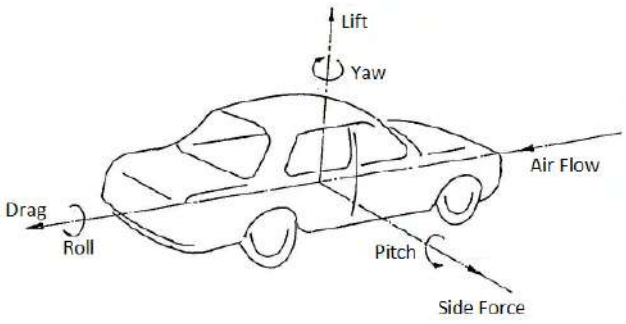

Figure 2.9: Aerodynamic forces. From [19].

Since cars have complex geometries, they generate vortices and flow separation zones. These phenomena are impossible to avoid, leading to the unsteadiness of the aerodynamic loads. Consequently, the test data sample must be large enough to capture any periodicity or to calculate an accurate mean value.

2.6 Balance Calibration

The previous sections present general remarks regarding wind tunnel testing in motorsport. This section relates to the aerodynamic balance, manufactured by Oliveira [20], which was used to acquire the aerodynamic loads during the wind tunnel testing.

To obtain accurate data from the force balance, a calibration process is necessary. The balance measures the strain values of each bar using strain gauges. This data is collected by two *NI 9237* acquisition systems provided by *National Instruments*™ [21]. The user interface created in *LabView*™ by Oliveira [20] gathers the different parameters necessary to present and record the loads in their intermediate or final form.

The first step of the calibration process is to correlate the strain with the force for each bar. To do so, the same calibration present in Oliveira [20] was used. The second step corresponds to the correlation between the 6 aerodynamic outputs (F_x - drag, F_y - side force, F_z - lift, M_x - roll, M_y - pitch, M_z - yaw) and the force carried in each bar. Finally, the correlation is added to the balance user interface to present the loads in their final form. During the balance calibration process, distinct types of loads were applied to the balance using a custom made apparatus (see Fig. 2.10).

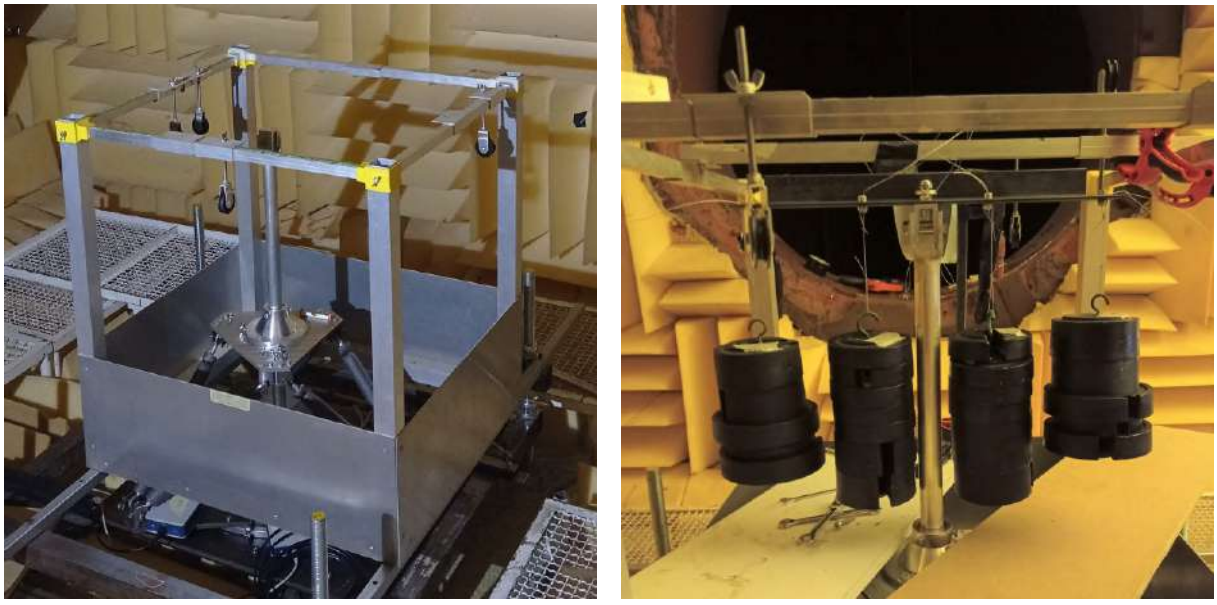

(a) Calibration apparatus.

(b) F_z load case, around 36 N in negative z direction. Load is applied symmetrical to eliminate any moments.

Figure 2.10: Force balance calibration.

Since the CFD setup was already completed, it was possible to estimate the expected forces and moments that should be achieved during the wind tunnel testing (Tab. 2.1). In that way, the load cases of the calibration were planned differently depending on the force/moment combinations expected during the experiments. Thus, the calibration matrix presents a higher data density near the expected operating loads.

Table 2.1: Calibration load case.

Reference case	$F_x\ [N]$	$F_y\ [N]$	$F_z\ [N]$	$M_x\ [Nm]$	$M_y\ [Nm]$	$M_z\ [Nm]$
FST 10e model @ $25\,\mathrm{m\,s^{-1}}$	-65	-2	-225	0.3	-3.5	0.05

Lastly, it was necessary to define a range of time to extract samples for averaging purposes. To define it, weights were loaded every 5 minutes to register the bars loads variations in time.

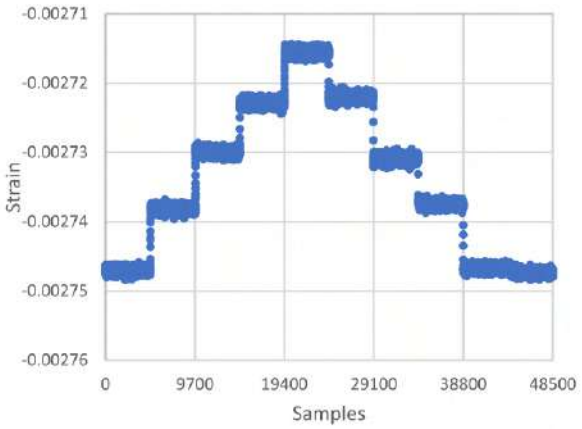

(a) Bar 1 strain during 45 minutes. A load of 20 N was loaded/unloaded each 5 minutes in negative x direction.

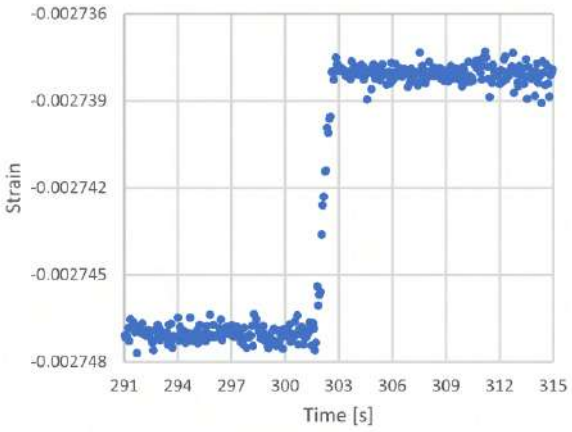

(b) Stabilization time during loading.

Figure 2.11: Force balance stabilization.

Figure 2.11 represents the strain in bar 1 during the calibration, where it is possible to observe a fast response and stabilization when constant loads are applied (around 2-3 seconds, which includes the loading process). A similar response time was also observed when evaluating the other bars.

2.6.1 Calibration Methodology

The load cases tested can be divided into three different cases: i) pure forces and pure moments, ii) combined forces and iii) combined forces and moments. Ideally, every type of pure or combined loads should be tested. However, since the calibration is a time consuming process, the main load cases were focused on F_x (negative), F_z (negative) and M_y, which were the expected predominant forces and moments during the experiments (refer to Sec. 3.2.1 for further information).

Weights of 1 N, 5 N, 10 N and 20 N were carefully weighted with a scale (ADAM PGW 4502i, accuracy of 10^{-5}kg), prior to use.

To ensure that the loads were applied in the desired direction axis, the calibration apparatus (cube shaped structure with pulleys constructed by Ferreira [22], see Fig. 2.10.(a)) was levelled and attached to the wind tunnel support with screws to reduce vibrations. Also, an L-shaped angle steel profile (see Fig. 2.10.(b)) was attached to the balance support to make possible the application of moments and high vertical loads (F_z negative).

After all preparations were complete, the calibration process began, following the calibration methodology described in Fig. 2.12: in the first 30 seconds, all the weight supports were loaded, then the weights were added every 30 seconds, however only 15 seconds were used to calculate the average strain, the rest was discarded due to the stabilization time of the force balance and mainly due to the loading process (the weights were slowly loaded to maintain vibration at the lowest, the loading process took a few seconds especially when combined forces/moments were being calibrated). Each load case sequence was repeated 3 times. In total, 267 load cases were tested. The post processing necessary to obtain the different calibration coefficient matrices can be found in Oliveira [20]. The calibration coefficient matrix C obtained as well as the calibration load cases are available in Appendix C.1.

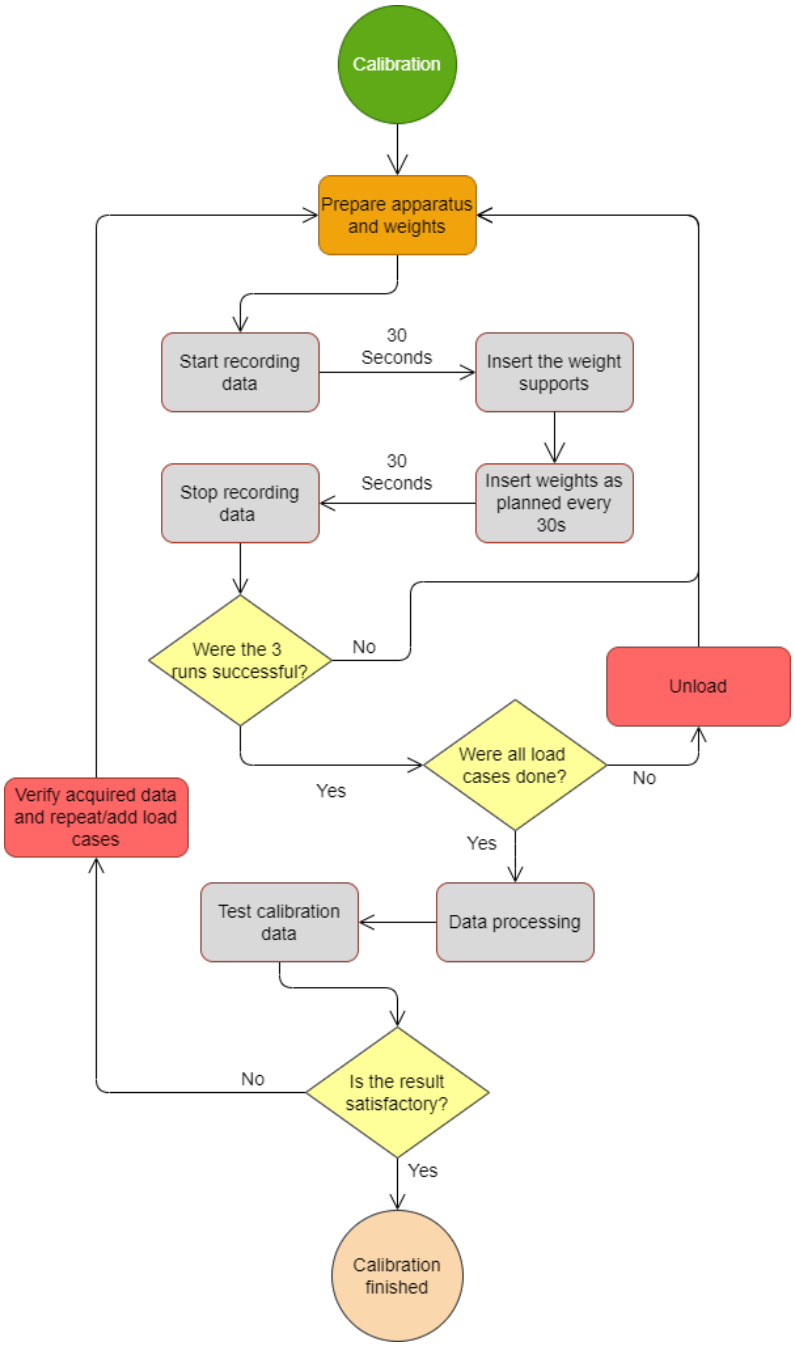

Figure 2.12: Force balance calibration methodology.

2.6.2 Calibration Check

Before testing the model, the calibration was tested by loading the balance with well known load cases. Once again, this process was focused on the main forces and moments (F_x negative, F_z negative, M_y). Initially, the balance was loaded (according with the calibration procedure) with the forces F_z and F_x combined, to understand if there was a relation between the two. It was clear that for high loads, these forces had a notorious dependency, which was not expected. To solve that, 36 new load cases were added to the calibration matrix around the expected load case obtained with the CFD setup (Tab. 2.1). Nevertheless, F_x still presented a maximum variation around 6.9 % when F_z was being loaded, as

marked in the red circles of Fig. 2.13.(a). While looking to the inverse loading process (Fig. 2.13.(b)), a maximum variation of only 1.7 % was captured in F_z when the maximum F_x load was applied.

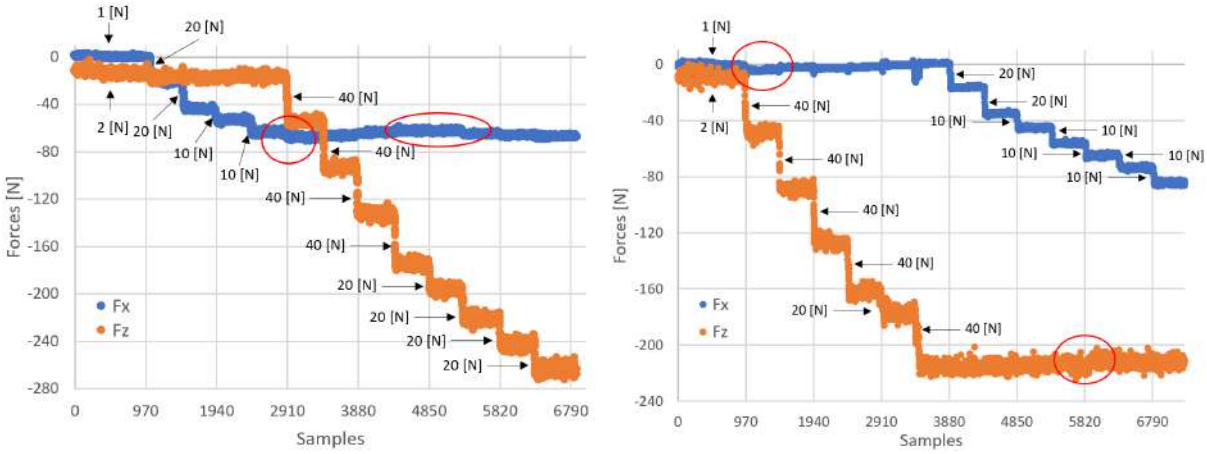

(a) F_{x-} load until -61 N followed by F_{z-} load.

(b) F_{z-} load until -221 N followed by F_{x-} load.

Figure 2.13: Force balance stabilization test cases F_x and F_z.

The aerodynamic balance did not behave entirely as a rigid body during the calibration process. When no loads were applied, a small looseness was noted in the attachments of the bars. This affected mainly the x and y direction (Fig. 2.14), which could be one of the causes for the variations presented in Fig. 2.13. However, regarding the z direction, no force variation was found during this test. Since the balance own weight produces a vertical downwards load, it might have eliminated any looseness affecting the vertical direction.

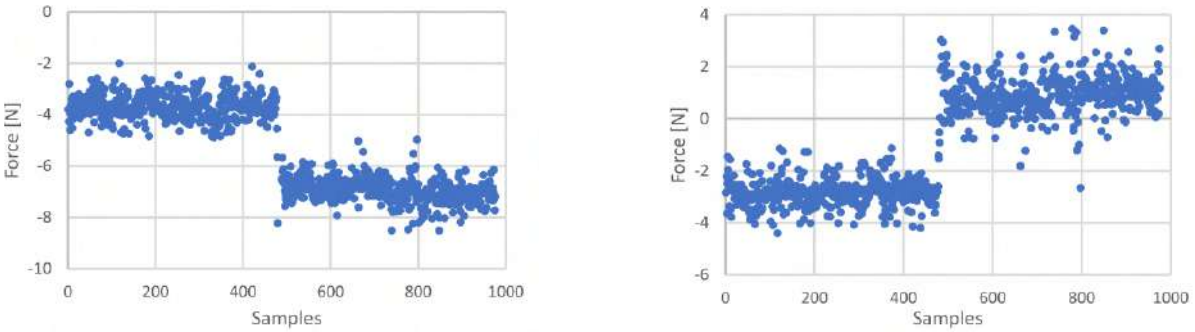

(a) F_x looseness.

(b) F_y looseness.

Figure 2.14: Force balance looseness.

2.7 Airflow Visualization

Despite being the oldest, smoke and tufts are the most commonly used techniques to provide diagnostic information relative to the airflow around a model of interest [23].

Smoke visualization technique (Fig. 2.15.(a)) is usually used away from the surfaces to spot vortices and separations zones. Tufts are used on the surface to detect cross-flow, reverse flow and also flow separation.

(a) Smoke and tuft. From [23]

(b) Flow-vis paint. From [24].

Figure 2.15: Flow visualisation techniques.

Tufts are the cheapest visualization technique, they are attached to the surface with tape or glue. When air passes through, the direction of the tufts reproduces the airflow near the surface. They must have a proper length and weight depending on their location on the surface so that they can move freely with the airflow [18].

Flow-Vis (Fig. 2.15.b) is another technique used in motorsport, which consists of a fluorescent powder mixed with oil and is normally used on track testing. Before going to the track, this mixture is poured on the car surfaces. Afterwards, the paint dries due to the evaporation of the oil, leaving a clear flow path on the surface. This technique can be used in wind tunnel testing. However, it is not recommended since the paint can damage the facilities and also due to the evaporation of possible toxic gases, especially when testing in a closed return wind tunnel with a closed test section [18].

2.8 Wind Tunnel Facility

The experiments were performed in the closed return aeroacoustic wind tunnel with an anechoic test chamber at Aerospace Engineering Laboratory in IST. A $200\,\mathrm{kW}$ motor rotates a seven blade fan that provides motion to the airflow up to $50\,\mathrm{m\,s^{-1}}$. The speed is controlled by a user input of the motor rotations per minute (RPM), which can reach 1500 RPM. However, for safety reasons, the rotational speed is limited to 1000 RPM, producing an airflow of approximately $43.5\,\mathrm{m\,s^{-1}}$ [25].

Figure 2.16 presents a computational model of the aeroacoustic wind tunnel with its general dimensions. The closed return was not included since it was used to perform computational simulations, Sec. 3.2 provides further information regarding the computational model. The wind tunnel has a $1.5\,\mathrm{m}$ diameter nozzle inlet and turning vanes at each corner helping the airflow to turn. Theoretically, the flow straightener, located just backwards from the nozzle, aligns the airflow and dissipates any turbulence. Thus, an uniform laminar airflow is supposed to enter the anechoic chamber. However, the wind tunnel characterization (the experimental tests will be discussed in Sec. 2.9.2) revealed an average turbulence intensity of 2% at the nozzle exit.

Initially, the facility did not have any apparatus to test a model of a car, as seen in Fig. 2.17.(a). The aerodynamic force balance, designed by Oliveira [20], was developed to be positioned at the lower part

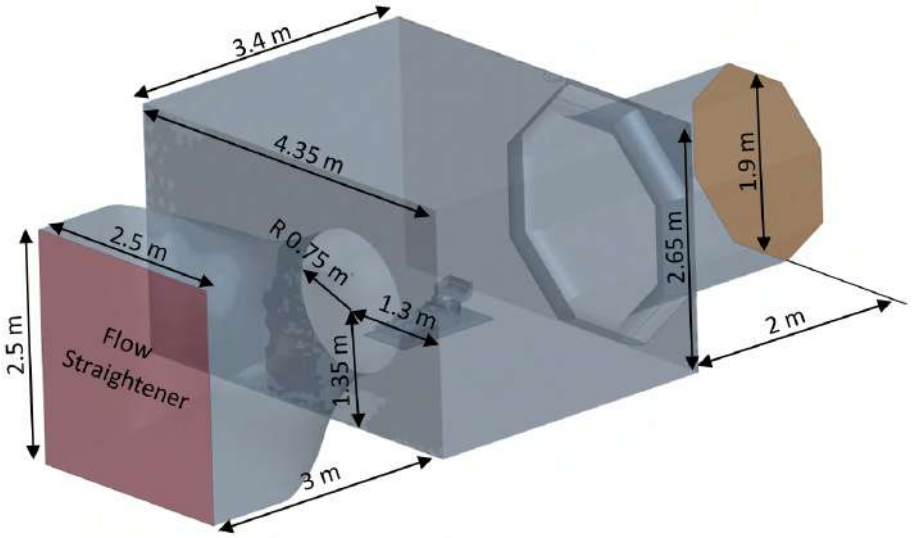

Figure 2.16: Aeroacoustic wind tunnel general measurements.

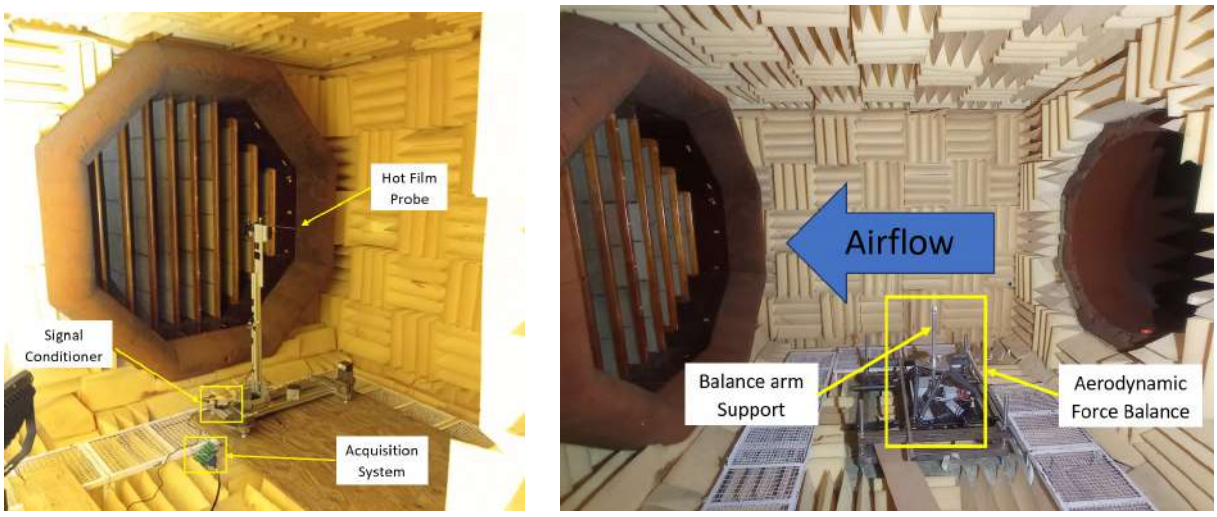

(a) Anemometry Test Setup.

(b) Aerodynamic Balance Setup.

Figure 2.17: Aeroacoustic wind tunnel test section at IST.

of the test section (Fig. 2.17.(b)). It is capable of measuring the six aerodynamic components (lift, drag, side force, roll, pitch and yaw - Fig 2.9). Installing a moving ground would require a huge effort due to the force balance characteristics. The only way to install a moving ground would imply to test the model upside down so that the model support arm would not cause a interference with the ground. Moreover, to decrease the blockage effects caused by the car wake and the balance components, the model should be tested as high as possible. The abnormal position of the car would increase the complexity of the overall apparatus, which was determined to be unrealistic.

The main objective of this work is to correlate wind tunnel data with CFD simulation, therefore the representation of reality turned to a secondary role as long as the same conditions were reproduced. As such, a stationary ground was considered to be the best option to be adopted and, consequently, stationary wheels too, Fig. 2.3.(e).

Facility Preparation

To guarantee the reliability of the results, it is important to ensure the structural integrity of the system and to maintain its vibrations to the minimum level possible. The wind tunnel facility was upgraded with a support frame which was constructed to provide fixed support for the aerodynamic force balance and the model ground, which is a $2\,\mathrm{m}$ long, $1\,\mathrm{m}$ wide with $3\,\mathrm{mm}$ thickness aluminium plate. The support was designed and built-in the concrete under the wind tunnel. It consists of four threaded rods (M27) that support a square steel tube platform. Due to the lack of concrete thickness under the test section, a block of reinforced concrete was elevated from it, which involved the frame support as seen in Fig. 2.18. Refer to Appendix B to access the mechanical study realized. Since the construction of this new support affected the quality of the anechoic camera, foam and mineral wool were added to further insulate the wind tunnel.

(a) Frame structure preparation.

(b) Frame structure installation.

Figure 2.18: Aeroacoustic wind tunnel facility upgrade.

The ground flap plate had a bed frame like support to ensure that no deformation occurred (Fig. 2.19.(a)). However, the bed frame was deformed during the welding process. Thus, medium density fibreboard and aluminium spacers were added between the ground and the bed frame to align the ground with the incoming airflow. As shown in Fig. 2.19.(b), the aerodynamic force balance was secured on the wind tunnel floor level. Therefore, it was necessary to cut a hole on the ground plate to attach the model with the balance arm vertical support.

Taking into account the distinct car conditions to be tested, it was decided to run the experiments with the wheels in the air instead of making holes for the tyres. In every single run, two cameras were recording the tyres displacement to ensure that no load was transferred from the car to the ground. In addition, a small deflection on the model arm support was observed during testing. Thus, another camera was pointed to the car nose which had a mark to measure the vertical displacement with help of a rule, as seen in Fig. 2.20. Combined with the distances of the front and rear axles to the attachment point of the model, it was possible to determine the pitch rotation of the car with the increasing speed.

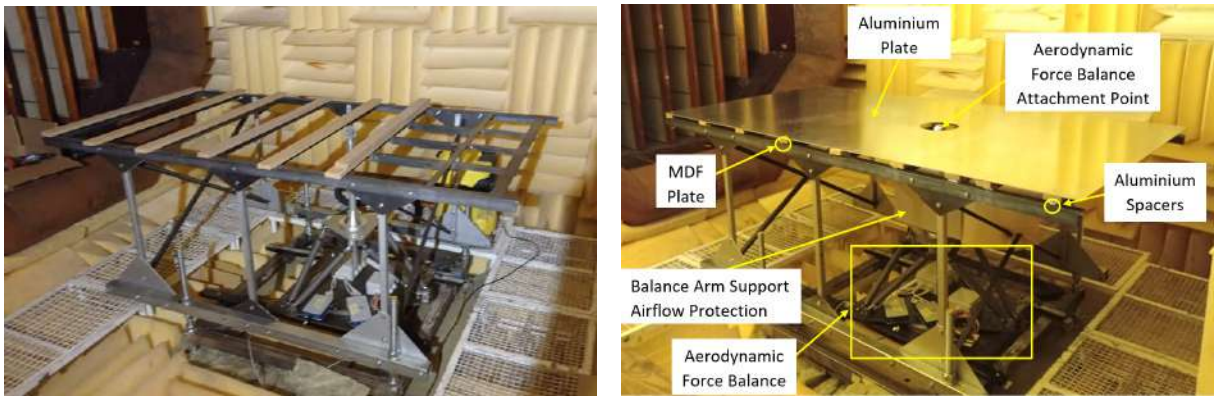

(a) Ground bed frame.

(b) Ground installed.

Figure 2.19: Aeroacoustic wind tunnel facility with ground and force balance mounted.

(a) Model nose vertical displacement.

(b) Front tyres ground clearance.

Figure 2.20: Ground clearance and car displacement check during experiments.

2.9 Airflow Definition

The wind tunnel facility was upgraded with an anechoic test chamber. Since its placement, different studies were performed. However, the airflow (inside the test section) was never characterized, which is fundamental to understand the airflow conditions (flow regime, boundary conditions, etc.) and to define the position and scale of the testing models. To overcome this problem, velocity measurements were made along several test sections to characterize the velocity profile of the jet and turbulence evolutions. The velocity measurements were taken with the *Model 1750* constant temperature hot film anemometer provided by *TSI Incorporated*®.

2.9.1 Components Calibration

First of all, a pressure sensor was calibrated inside a room with a controlled environment. Then, it was used to calibrate the hot wire anemometer, which was responsible for taking the velocity measurements for the wind tunnel characterization.

Pressure Sensor

The pressure sensor used was a differential pressure sensor (*Schlumberger® H5010* coupled with the *Schlumberger® D5484* signal conditioner) with a Prandtl probe, the static pressure take was connected to the probe and the total pressure take was connected to a U-tube manometer (Fig. 2.21). A direct current source powered the sensor (*TTI TSX3510*) and the output voltage was measured by a digital multimeter (*HP 34401A*). The signal conditioner and pressure sensor specifications are presented in Sec. D.2.

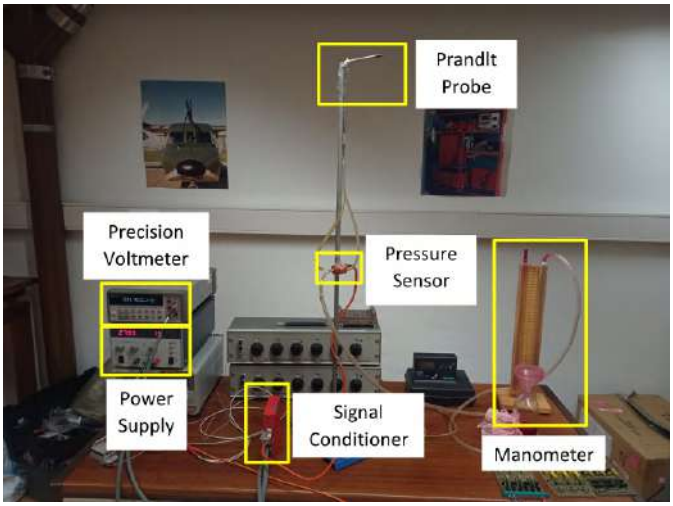

Figure 2.21: Pressure sensor calibration setup.

Assuming incompressible flow and negligible dissipation, the Bernoulli's principle [26]

$$p_t = p_s + \rho g z + \overbrace{\frac{1}{2}\rho V^2}^{\text{Dynamic Pressure}} = constant \tag{2.3}$$

can be applied to the manometer as: $(p_t)_{room} = (p_t)_{manometer}$. The calibration conditions and the fluids properties are presented in Tab. 2.2.

Table 2.2: Room conditions and fluids proprieties.

Property	value	units
Room pressure	100864	Pa
Acceleration of gravity	9.80054	$m\,s^{-2}$
Room temperature	20	℃
Manometer fluid density	784	$kg\,m^{-3}$
Air fluid density	1.219	$kg\,m^{-3}$

Figure 2.22.(a) presents the pressure sensor calibration, which revealed a linear relationship between pressure and output voltage. Being a differential pressure sensor, the pressure measured was directly the dynamic pressure $p_{dynamic} = \frac{1}{2}\rho_{air}V_{air}^2$. Finally, the relation between the mean airflow speed at the center of the test section inlet and the motor RPM was obtained, as shown in Fig. 2.22.(b).

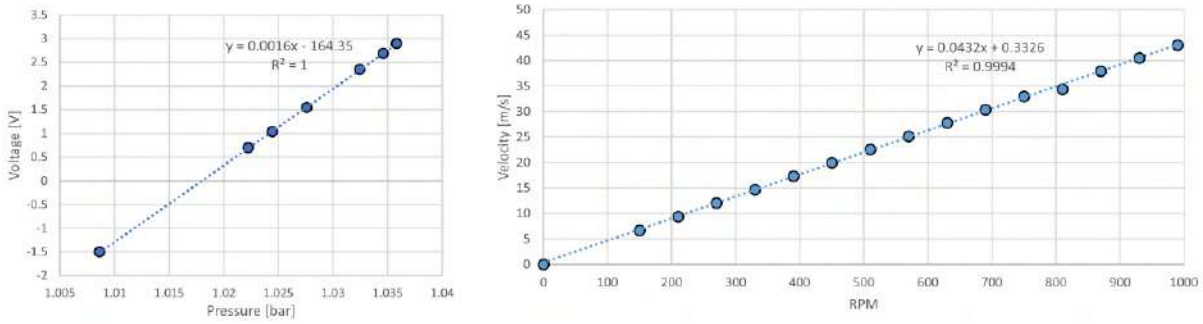

(a) Linear relation between the output voltage and the differential pressure.

(b) Wind tunnel airflow velocity related to the motor RPM.

Figure 2.22: Wind tunnel apparatus calibration.

Hot Wire Anemometer

To calibrate the Model 1750 Constant Temperature Anemometer, a flow with known velocity is needed. During the calibration process, the speed must vary from zero to the desired speed ($45\,\mathrm{m\,s^{-1}}$) with a minimum of 15 intermediate calibration points [27]. The calibration was performed inside the aeroacoustic wind tunnel where the differential pressure sensor was positioned near the anemometer probe, as seen in Fig. 2.23.(a). The anemometry data was acquired with a *NI PCIe - 6321* acquisition system with 16 bits provided by *National Instruments*™ [28]. The specifications of the Model 1750 Constant Temperature Anemometer is available in Sec. D.1.

An initial calibration curve was obtained with the anemometer probe support perpendicular to the incoming airflow. However, high vibrations were visible, which affected the results. Regarding the remaining experiments, the anemometer support was placed parallel to the incoming airflow, which reduced significantly its vibrations (only some minor vibrations related to the structure could not be eliminated). The calibration curve retrieved is presented in Fig. 2.23.(b).

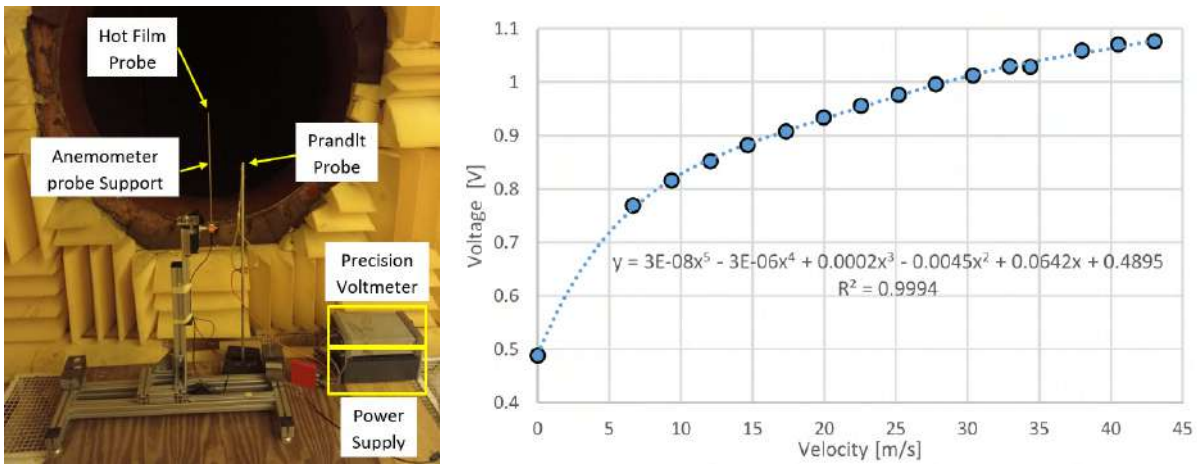

(a) Anemometer calibration apparatus.

(b) Anemometer calibration curve.

Figure 2.23: Anemometer calibration.

During the calibration process, the inability to extract heat from the wind tunnel made it impossible to control the temperature. As such, the calibration was performed as quickly as possible to minimize

the consequences of the increasing temperature. Analysing Fig. 2.24, the temperature increase is notorious when the fan motor surpasses 610 RPM. However, some problems regarding the anemometer support emerged. Considering the circumstances, the wind tunnel had to be shut down, which caused a decrease in temperature. Nonetheless, the same effects were noted for higher RPM.

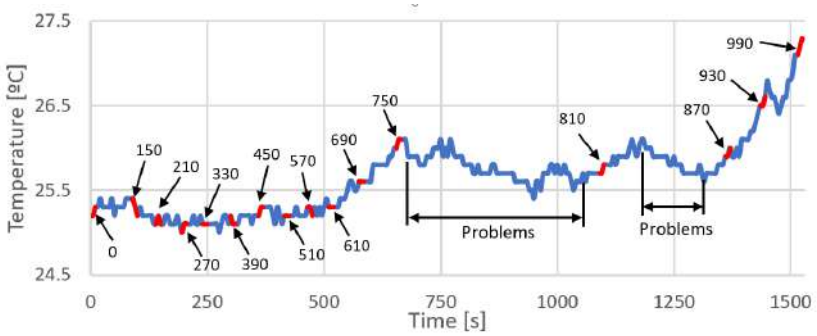

Figure 2.24: Anemometer calibration experiment temperature.

2.9.2 Wind Tunnel Characterization

Initially, the wind tunnel characterization data was taken at approximately $u_x = 43\,\mathrm{m\,s^{-1}}$ (990 RPM), around the maximum speed allowed for safety reasons[3]. Still, it was impossible to maintain a steady temperature during the wind tunnel running time as seen at Fig. 2.25. Furthermore, at this speed, the anemometer support presented significant vibrations, harming the collected data. Also, the 3D printed part that secured the anemometer probe failed. It expanded due to the high temperature, deeming it impossible to perform the tests at approximately $u_x = 43\,\mathrm{m\,s^{-1}}$ (990 RPM).

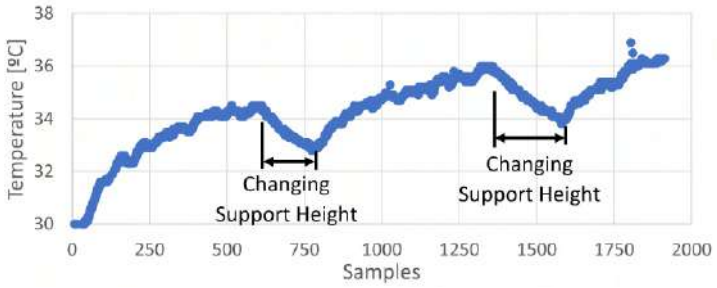

Figure 2.25: Temperature evolution while getting velocity data at $43\,\mathrm{m\,s^{-1}}$.

Consequently, the speed measurements were taken at $u_x = 25\,\mathrm{m\,s^{-1}}$ (571 RPM), maintaining a stable temperature around 27 ℃. The test apparatus presented some problems as well. The experiments were carried out on the top of a wood plank (before the balance support was built-in), supported by an aluminium structure at its edges. As a result, the wood plank was subjected to high vibrations whenever forces were applied to it.

The data was extracted for five sections at 315, 415, 515, 1030 and 2330 mm from the jet inlet. The first three sections were located between the nozzle and the supposed testing location of the model.

[3]At this point, the model scale was already fixed at 1/3 and, since the mean car velocity during competition rounds $15\,\mathrm{m\,s^{-1}}$, it was defined that the experiments should be done at $45\,\mathrm{m\,s^{-1}}$ to maintain Reynolds similarity. However, it was not possible for safety reasons. Thus, the maximum motor speed was the next target (990 RPM).

The fourth was located in the middle of that location and the last one was defined further behind. During the anemometry, 35 data points were extracted (for each section) in a vertical line. The first point was located at the center of the section. The rest were separated by 25 mm from each other.

Wind Tunnel Jet

Figure 2.26 shows a schematic of an open test section wind tunnel jet. The airflow speed is represented by u, where u_0 represents the speed of the uniform velocity profile, $u_m(x)$ is the velocity at the jet centreline and u_∞ the free stream airflow (zero in this case). The potential core is the zone where the velocity vector still remains equal to the uniform velocity profile. Shear layers are associated with the zones where the tangent velocity presents rapid changes. At the nozzle exit, the shear layers are formed due to the contact between the potential core and the free stream flow. Then, the further away from the nozzle, the bigger this layer gets due to the increasing perturbations in the airflow. At one point, as seen in Fig. 2.26, both shear layers merge, turning the flow fully turbulent.

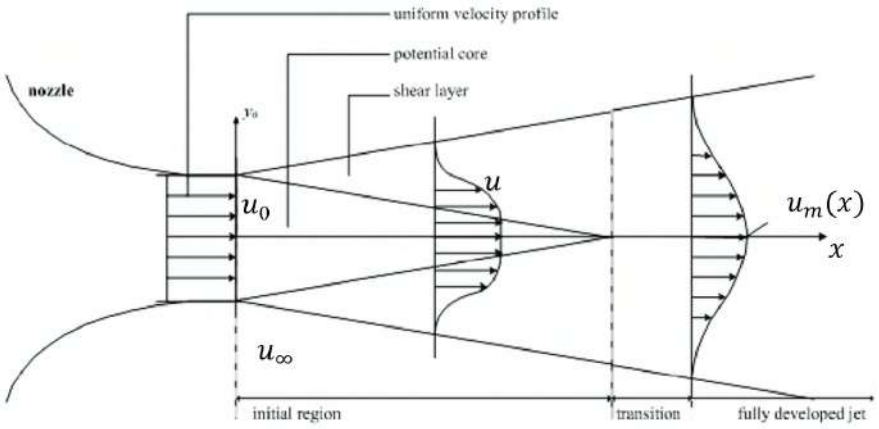

Figure 2.26: Open jet wind tunnel scheme. From [29].

Numerical simulations were also performed for an empty wind tunnel to recreate the experimental conditions. The numerical results presented in this section do not have any uncertainty associated. To do so, it would be necessary to perform a time costly mesh convergence analysis to estimate the numerical error (similar to the analysis presented in Sec. 3.2.5). Since the numerical mesh was enhanced for simulations with the car model, the sections where the data was collected presented a great refinement. Thus, the uncertainty was expected to be negligible.

The following subsections present a comparison between the experimental tests and the numerical simulations (refer to Sec. 3 for further details related to the numerical simulations).

Velocity Profiles

The figures showing the velocity profile at the different sections can be found in Appendix A. Figure 2.27.(a) illustrates the coordinate system adopted during the anemometry studies while Fig. 2.27.(b) illustrates the anemometer movement for each section, as well as some important measures. The wind tunnel test section inlet has a radius (r_{inlet}) of 750 mm, and the jet center is defined as $vertical\ distance\ 0$.

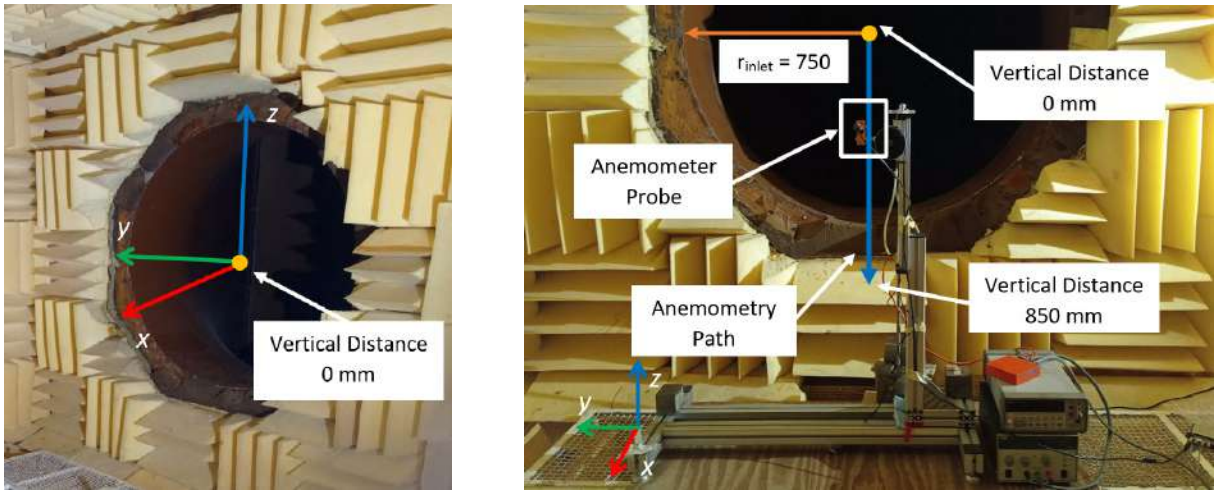

(a) Coordinate system.

(b) Anemometry scheme.

Figure 2.27: Wind tunnel characterization - anemometry study.

Regarding the first ($x = 315\,\text{mm}$) and third section ($x = 515\,\text{mm}$) (Fig. A.1 and Fig. A.3 respectively), the shear layers begin to be significant at $r_{inlet} > 700\,\text{mm}$ as the velocity gradient increases heavily. The measurements of the second section are not reliable because the experiment was affected by problems related to the anemometer signal conditioner and the acquisition system.

Focusing on the fourth section (Fig. A.4), the area affected by the shear layers increased and impacts the velocity profile around r_{inlet} = 650 mm. Finally, the last section (Fig. A.5) presents a smoother velocity drop characterized by the lower velocity gradient that is felt around r_{inlet} = 625 mm.

Figure 2.28 presents the normalized velocity evolution along the airflow jet. Four different radial coordinates were designated, $z = 0\,\text{mm}$ defines the airflow jet center, the other sections are distanced by 250 , 500 and 750 mm from it.

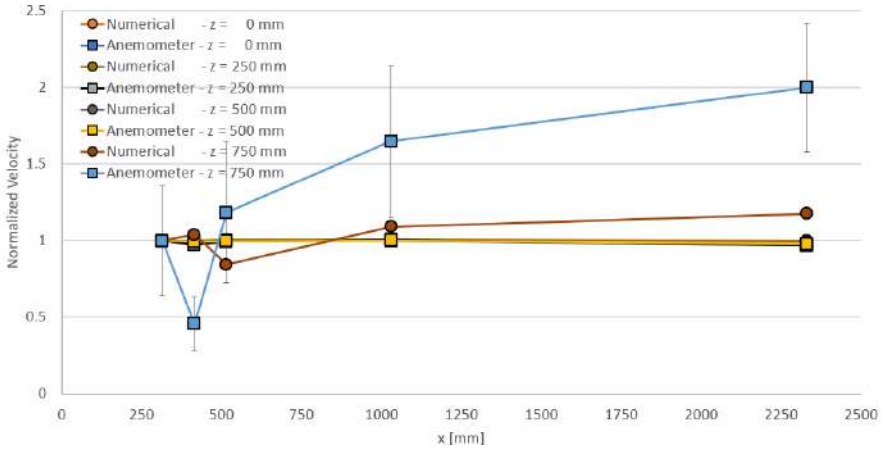

Figure 2.28: Wind tunnel longitudinal velocity evolution.

Regarding the first three sections ($z = 0$, 250 and 500 mm), the velocity presents a very small decrease along the x-axis, it is felt more the furthermost from the center. The CFD data presents a satisfactory correlation with the experimental data. At $z = 750\,\text{mm}$ (corresponds to the nozzle radius)

the velocity decreases near the inlet, followed by a notorious increase along the x-axis. The wind tunnel data presents a higher increase than the numerical one, which can be justified by the higher turbulence intensity felt around this section.

Turbulence Intensity

Turbulence is a three-dimensional phenomenon that is characterized by its irregular fluctuations. It affects the transport momentum, heat and mass and also intensifies the fluid friction losses. A wind tunnel is supposed to provide a controlled air motion to replicate the airflow around an object of study, however, it is impossible without causing fluid friction losses.

The most notorious characteristic of a turbulent flow is the irregularity of the velocity field, which corresponds to fluctuations with a wide range of frequencies, as illustrated in Fig. 2.29.(a). Despite the origin of turbulence being random perturbations in nature, turbulence energy spectrum has a typical shape, as seen in Fig. 2.29.(b) [30, 31].

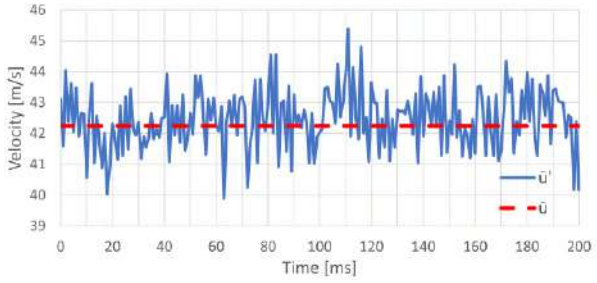

(a) Velocity fluctuations at 990 RPM.

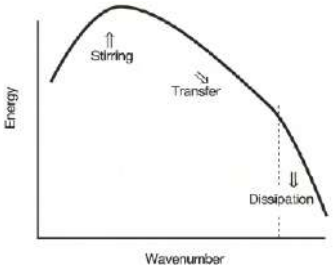

(b) Typical shape of the turbulence energy spectrum. From [31].

Figure 2.29: Turbulence characteristics.

Due to the random nature of the airflow, statistical methods are imperative as a substitute for deterministic methods [30]. The velocity field $u(t)$ is decomposed in two components: $\overline{u}(t)$ for the mean value and $\overline{u_i'}$ for the fluctuations. For both, a simple mean value method can be applied since the velocities in study are supposed to remain constant over time,

$$\overline{u}(t) \equiv \overline{u} = \lim_{t\to\infty} \frac{1}{t} \int_{t_0}^{t_0+t} u dt \equiv \frac{1}{N} \sum_{1}^{N} u, \tag{2.4a}$$

$$\overline{u'} = \lim_{t\to\infty} \frac{1}{t} \int_{t_0}^{t_0+t} (u-\overline{u}) dt \equiv \frac{1}{N} \sum_{1}^{N} (u-\overline{u}). \tag{2.4b}$$

Finally, the turbulence intensity can be represented by a scalar value:

$$TI = \frac{\overline{u'}}{\overline{u}}. \tag{2.5}$$

The apparatus available and the wind tunnel facilities did not allow to collect data from a whole section. Therefore, an axisymmetric jet condition was assumed. Also, the anemometer probe used was designed for unidirectional flows. Despite being a jet, the wind tunnel has an open test section, meaning

that it would be a rough approximation to assume unidirectional turbulence. As a consequence, the turbulence was assumed to be isotropic ($\overline{u'_x} = \overline{u'_y} = \overline{u'_z}$). Taking into consideration this assumption, the turbulence intensity can be calculated as:

$$TI = \frac{\sqrt{\frac{2}{3}k}}{\overline{u}}, \tag{2.6}$$

where $k = \frac{1}{2}(\overline{u'_x}^2 + \overline{u'_y}^2 + \overline{u'_z}^2)$ is the turbulent kinetic energy (TKE).

The turbulence intensity evolution along the streamwise x direction is presented in Fig. 2.30. It corresponds to the same radial coordinates ($z = 0$, 250 , 500 and 750 mm) as the velocity evolution in Fig. 2.28.

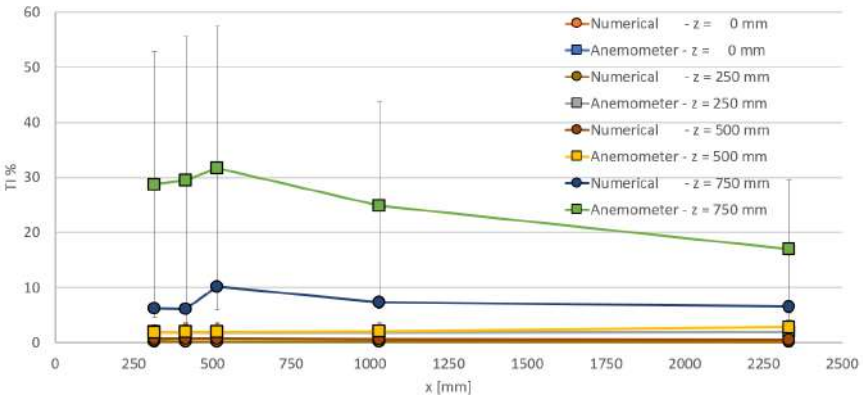

Figure 2.30: Wind tunnel longitudinal turbulence intensity evolution.

Since the focus of this work is to discuss the quality of the numerical simulations, the turbulence intensity behaviour will be compared qualitatively between the experiments and the CFD simulations. Typically, the numerical results are affected by the inlet boundary conditions. Thus, it is important to address the turbulence intensity because it is one of the quantities defined in that boundary (Sec. 3.2.3 provides the quantities defined in the distinct boundaries used).

At first sight, the numerical data presents the same trend as the data acquired by the experimental anemometry. Regarding the sections $z = 0$, 250 and 500 mm, the turbulence intensity increases gradually with the distance to the inlet as the shear layers grow. As expected, the middle section $z = 0$, is the least affected by the shear layers increases. The turbulence intensity mean value remains approximately constant at 2%. The experimental data suggests an increase from 1.87% to 2%. However, the uncertainty is greater than the difference registered. In contrast, the numerical simulations registered a value of 0.25% approximately, which is highly dependent on the inlet boundary condition. Even if the inflow turbulence intensity was measured experimentally (which was not possible), the mathematical models fail to recreate accurately the evolution of the inflow turbulence as the boundary conditions are defined far upstream from the test section, which allows a deep decay of the inflow quantities [32].

On the other hand, focusing on the section entirely inside the shear layers ($z = 750$ mm), it is reasonable to expect an increase in the turbulence intensity closer to the inlet, where the turbulent energy is concentrated in the large eddies. As the distance to the inlet increases the turbulence intensity decay as the turbulent kinetic energy dissipates.

Chapter 3

Mathematical Formulation of the Problem

In this chapter, the computational component of the work and its mathematical formulation are briefly addressed. Afterwards, the simulations setup, a mesh convergence study and an assessment of the numerical error are described.

3.1 Mathematical Formulation

Wind tunnels are characterized by their turbulent fluid flow, in which the fluid undergoes irregular fluctuations. Since these fluctuations occur at small scales and high frequencies, it is extremely costly to compute them in time and space. Using directly the governing equations of turbulent flows (Direct Numerical Simulation (DNS)) enables the resolution of all scales of the flow. However, the computational cell size dictates the minimum turbulent eddy size that can be obtained. Thus the number of cells required increases with the Reynolds number [33]. The airflow expected while testing the car is characterized by a Reynolds number greater than $Re > 10^6$, and it is dominated by very small structures due to the complex geometries. As a result, DNS is not feasible to simulate the wind tunnel conditions. However, the Reynolds Average Navier Stokes (RANS) equations are appropriated to the airflow characteristics expected. A steady state is achieved since they provide a time average for the flow quantities ϕ. Energy, pressure, velocity and density are decomposed into its average value $\overline{\phi}$ and its fluctuating component ϕ' [34],

$$\phi = \overline{\phi} + \phi'. \tag{3.1}$$

As stated in Sec. 2.1, for the working speeds is reasonable to assume imcompressible flow. Thus, RANS equations can be written as [30, 35, 36]:

$$\rho \frac{\partial \overline{u_i}}{\partial x_i} = 0 \quad \text{(Continuity)}, \tag{3.2a}$$

$$\underbrace{\rho\overline{u}_j\frac{\partial\overline{u}_i}{\partial x_j}}_{\text{Inertial Forces}} = \frac{\partial}{\partial x_j}\Bigg[\underbrace{-\overline{p}\delta_{ij}}_{\text{Pressure Forces}} + \underbrace{\mu\left(\frac{\partial u_i}{\partial x_j}+\frac{\partial u_j}{\partial x_i}\right) - \overbrace{\rho\overline{u_i'u_j'}}^{\text{Reynolds Stress}}}_{\text{Viscous Forces}}\Bigg] \quad \text{(Momentum).} \tag{3.2b}$$

Finally, a turbulence model acts as a closure model to compute the Reynolds stress since the velocity fluctuations can not be directly calculated.

3.1.1 Turbulence Model

The $k-\omega$ SST is a two equation model that predicts turbulence by solving transport equations for two variables: turbulent kinetic energy k and specific turbulent dissipation rate ω. It is one of the most commonly used models for wall bounded flows and presents great performance for complex boundary layer flows under adverse pressure gradients [37]. Thus, the $k-\omega\ SST$ turbulence model was used to perform the computational work in this master thesis.

3.1.2 Transition Model

In laminar flow, fluid particles move along each other smoothly in independent trajectories. Whenever perturbations happen, laminar flow can transit to turbulent. Typically, transition in boundary layers can occur by three primary modes [38]: i) Natural Transition, when weak instability waves appear and are amplified; ii) Bypass Transition, caused by external perturbations (incident waves, free stream turbulence and others); and iii) Separation (laminar bubbles) when laminar flow separation leads to transition.

Transition is a very complex phenomenon that has gathered a lot of attention over the years. Some models achieve excellent results for well-behaved attached airflows, either fully laminar or fully turbulent. However, none of them are capable of modelling transition with the same accuracy, not even when the easiest case as a flat plate is considered [30, 38].

Eddy viscosity turbulence models are mathematically derived to work with fully turbulent flows. Although some can actually predict transition, it happens at unrealistic Reynolds number (*Re*), which usually is lower than normal (around $Re \approx 10^4$) [39]. Whenever strong adverse pressure gradients are present, turbulence models fail to predict transition induced by separation. They anticipate transition upstream of the laminar separation point. Thus, laminar bubbles phenomena can not be reproduced [40].

To achieve realistic transition phenomena, transitions models can be used alongside turbulence models. *StarCCM+*® presents three distinct solutions to this problem [35]:

- Turbulence suppression model: Zero equation model which can be used with any turbulence model. The user defines the transition point by designating the zone where turbulence is suppressed;
- Gamma Re Theta transition model ($\gamma - Re_\theta$): Two equation model that solves two additional transport equations for intermittency[1] and momentum thickness Reynolds number. It can be coupled

[1] Measure of time in which flow is turbulent.

with $k-\omega\ SST$;

- Gamma transition model (γ): This model is a simplification of the $\gamma - Re_\theta$ transition model, and only solves the transport equation for the intermittency.

Figure 3.1 shows the transition Reynolds number for experimental tests and distinct mathematical models along a finite plate [41], in which the black line represents the $k-\omega\ SST$ turbulence model and the blue and red lines are obtained using the γ transition and the $\gamma - Re_\theta$ models (coupled with the $k-\omega\ SST$ turbulence model) respectively.

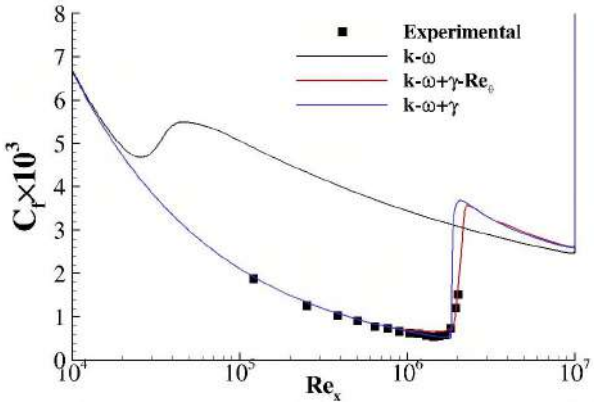

Figure 3.1: Skin friction coefficient along a finite plate. From [41].

When not using a transition model, the $k-\omega\ SST$ predicts transition around $Re \approx (3 \times 10^4)$, which is unrealistic for natural transition. On other hand, the $k-\omega\ SST$ coupled with any of the two transition models predict transition around the same value $Re \approx (2 \times 10^6)$ as the experimental tests. Thus, the transition models are capable to predict transition at realistic Reynolds numbers. However, since the wind tunnel conditions are distinct and more complex than a finite plate, the effects of the transition models on the car were studied.

Transition Model Study

As mentioned before, turbulent models usually predict transition at unreasonable small Reynolds numbers. The front wing is one of the few components of the car to be reached by laminar airflow. Thus, the distinct turbulence models were studied in this component.

Table 3.1 contains the parameters evaluated with (γ transition model) and without transition model. The iterative convergence could not be achieved with the $\gamma - Re_\theta$. Thus, this model was not considered in further analysis.

As expected, the γ transition model simulation was more time expensive (40% times) than not using a transition model. However, the difference between the forces coefficients is almost null. On top of that, the difference registered is within the estimated numerical error (refer to Sec. 3.2.5.).

Figures 3.2 and 3.3 present the surface skin friction coefficient $C_f = \frac{\tau_w}{\frac{1}{2}\rho V^2}$ and pressure coefficient $C_p = \frac{p - p_{ref}}{\frac{1}{2}\rho V^2}$, where τ_w represents the wall shear stress and p relates to pressure.

Table 3.1: Transition model analysis.

Transition Model	No transition	γ transition
Car C_L	3.27	3.31
Car C_D	1.55	1.56
Front wing C_L	0.98	1.01
Front wing C_D	0.14	0.14
Iteration elapse time [s]	47.36	65.07

The C_f and C_p coefficients were retrieved along the section y = 0.175 m of the front wing assembly. When no transition model is used, the skin friction coefficient (Fig. 3.2.(a)) presents a minimum immediately after the leading edge of the main plane, around $x \approx 5\,\text{mm}$. This minimum corresponds to the transition from laminar to turbulent airflow, which can be further corroborated by the growth of the turbulent kinetic energy (TKE) at this location, as shown in Fig. 3.4.(b). Despite being affected by a favourable pressure gradient, as marked in Fig. 3.2.(b), transition still occurs. Moreover, the same phenomenon can be seen in the front wing flap.

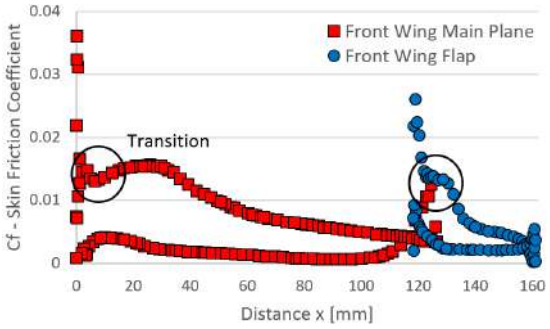

(a) Skin friction coefficient.

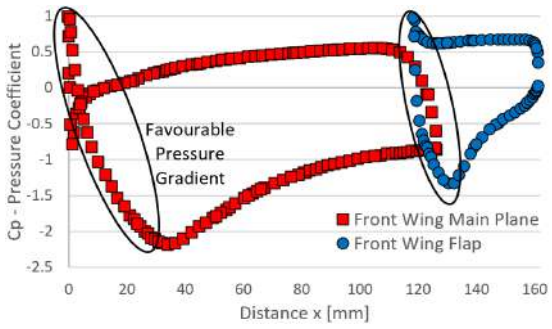

(b) Pressure coefficient.

Figure 3.2: No transition model.

Due to the transition odd location, the same section was evaluated with the γ transition model (Fig. 3.3).

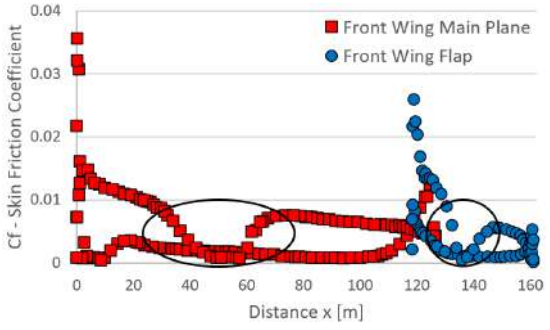

(a) Skin friction coefficient.

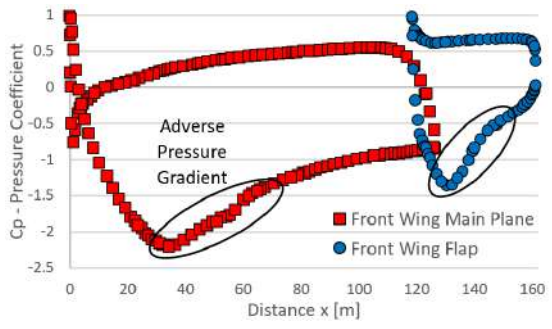

(b) Pressure coefficient.

Figure 3.3: Gamma transition model.

As a result, the transition jumped to around $x \approx 60\,\text{mm}$, as shown in Fig. 3.4.(a). At the same point, the skin friction coefficient decreased to zero, as illustrated in Fig. fig:Gamma transition model..(a). In this case, the transition was caused by laminar separation bubbles. This phenomenon appeared

exclusively with the gamma transition model as seen in Fig. 3.4.(a). As shown in Fig. 3.3.(b), the surface zone that presents laminar separation bubbles is under an adverse pressure gradient, which verifies the transition location. Moreover, a sudden slight jump in the pressure coefficient takes place at the same location, which corroborates the phenomenon described.

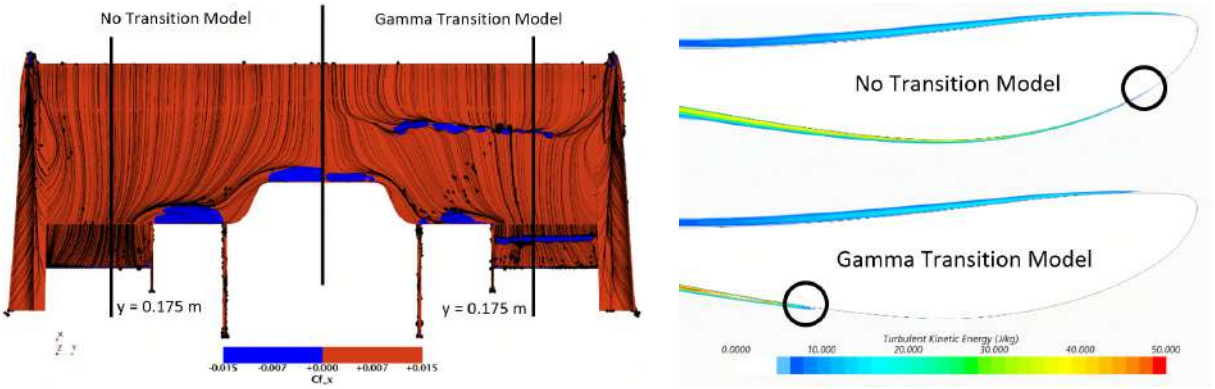

(a) Skin friction coefficient on the front wing suction side.

(b) TKE growth due to transition.

Figure 3.4: Comparison between the simulation results using the gamma transition model and no transition model.

In conclusion, the simulations without a transition model do not exhibit the correct physics of the flow. A transition model is required to predict the existence of laminar separation bubbles which is typical of low Reynolds number flows. Despite being more time costly, the γ transition model presents evident advantages. Thus, it was used in the numerical simulations.

3.2 Mesh Convergence

Since one of the objectives of this work is to correlate the wind tunnel results to the CFD models, the numerical domain was a recreation of the Aeroacustic Wind Tunnel, where the experimental work took place. To meet the above-mentioned objectives, it was necessary to model the entire wind tunnel, which required huge computational resources. However, there is no technical document of the wind tunnel, making it impossible to model accurately.

The numerical domain was divided into three different zones as presented in Fig. 3.5: nozzle, anechoic chamber test section and outlet zone.

3.2.1 Coordinate Systems and Aerodynamic Loads

Two distinct coordinate systems were used to define the model location and to study aerodynamic loads, as seen in Fig. 3.6.

The axis origin of the first one is located at the center of the front axle on the ground surface. This axis system follows the car, in other words, whenever the car moves position, the origin moves with it. This system was mostly used until the final model position inside the wind tunnel was settled. Until then, only the lift and drag forces were accounted for ($F' = (F_{x'}, F_{z'})$) and were presented in coefficient form,

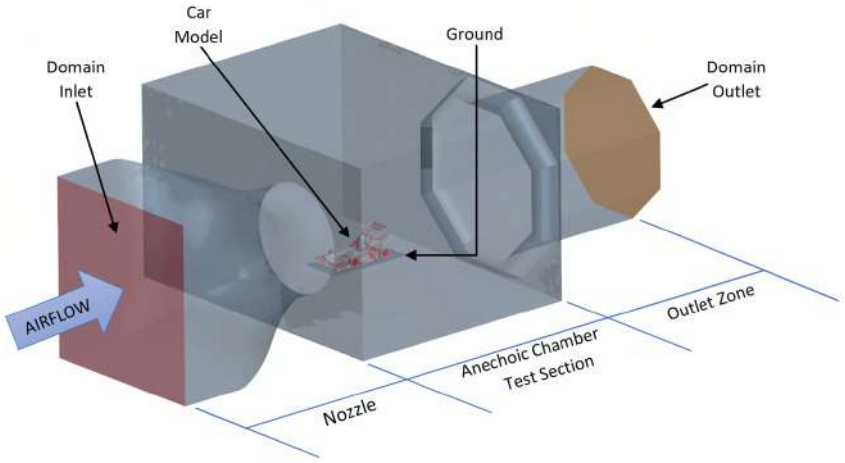

Figure 3.5: Numerical domain scheme.

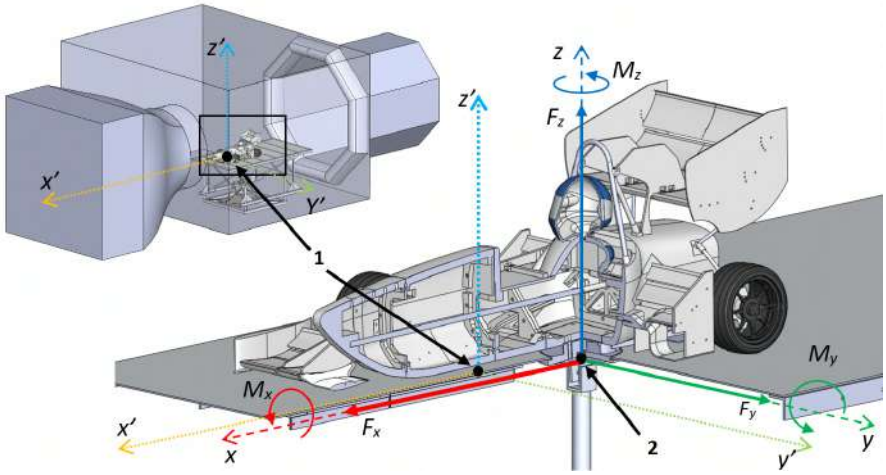

Figure 3.6: Coordinate systems.

respectively C_L and C_D.

The aerodynamic forces and moments were obtained with the coordinate system number 2. Its origin is the point of attachment to the balance support arm. This axis system was defined only when the final position of the model (within the wind tunnel boundaries) was defined. Thus, the forces $F = (F_x, F_y, F_z)$ and moments $M = (M_x, M_y, M_z)$ could be directly compared with the balance experimental loads. The two coordinate systems are related by a simple translation of the origin. Also, the forces in the lift (Eq. 1.1) and drag (Eq. 1.2) coefficients were calculated, respectively, by L = $-F_z$ and D = $-F_x$.

In this initial study, only straight line conditions configurations were tested (proceed to Sec. 5.2 for further information). Hence, the predominant aerodynamic loads expected were F_x, F_z and M_y due to the geometrical symmetry between the left and right sides. In contrast, the loads F_y, M_x and M_z were neglected since they did not present any relevant information.

To transform aerodynamic loads into its dimensionless coefficients, it is necessary to establish a fixed reference area S and reference chord length b. These parameters were defined, respectively, as the FST10e frontal area ($\approx 1\,\mathrm{m}^2$) and its length ($\approx 3\,\mathrm{m}$). In addition, the scale factor has to be accounted

in both parameters. To sum up, the reference area S and reference chord length b can be calculated by $S = \frac{1}{scale^2}$ and $b = \frac{3}{scale}$ respectively.

3.2.2 Models

The models defined in *StarCCM+*® software represent the substance being simulated. It incorporates not only the mathematical models but also the boundary conditions, material proprieties, and also discretization and solution techniques, as listed in Tab.3.2.

Table 3.2: *StarCCM+*® - numerical simulation models.

Mathematical	Boundary Conditions	Material Properties	Solutions Techniques	Discretization Techniques
Turbulent	Wall distance	Gas	Segregated flow	Three dimensional
Reynolds-Average Navier-Stokes	All y+ wall treatment	Constant density	Steady	Cell quality remediation
K-Omega turbulence		and viscosity	Gradients	
SST (Menter) K-Omega		(ρ = 1.225 kg m^{-3}		
Gamma transition		$\mu = 1.8 \times 10^{-5}$ Pa s)		

3.2.3 Boundary Conditions

Numerical methods require a domain with physical boundaries where the problem can be solved. Thus, it is necessary to define how the airflow behaves when it reaches or passes the physical boundaries. To do so, boundary conditions must be assigned for each surface. Table 3.3 presents the selected boundary conditions that reflect the physical domain of the wind tunnel as well as the initial conditions of the problem.

Table 3.3: Boundary conditions.

Boundary Conditions	Flow Variables	Boundaries
Velocity Inlet	Defines the inflow condition and flow proprieties, where the velocity $u_x = u_{inlet}$ value was set depending on the simulation finality. The *turbulence intensity* was defined as TI = 0.01 and *turbulence viscosity ratio* as μ_T/μ = 10.	Domain Inlet
Pressure Outlet	Defines the outflow condition, it imposes a static pressure to the boundary. Velocity is extrapolated from the domain. The pressure was defined to $p_{static\ outlet} = p_{ref} =$ 101 325.0 Pa. The *turbulence intensity* was defined as TI = 0.01 and *turbulence viscosity ratio* as μ_T/μ = 10	Domain Outlet
Wall (no slip condition)	Defines a solid surface where the fluid attached presents the same velocity as the surface.	Car model, Ground and Domain Walls
Initial conditions	The *intermittency* was defined as γ = 1, the *turbulence intensity* as TI = 0.01 and *turbulence viscosity ratio* as μ_T/μ = 10.	Region (volume domain)

Sensitivity study of the outlet location

The boundary condition at the outlet of the domain imposes a fixed pressure, which theoretically would only occur at large distances from the test section. Therefore, a sensitivity study was performed to verify the influence of the outlet location on the drag and lift coefficients of the car. The outlet pressure was fixed to $p_s = 0\,\text{Pa}$. Figure 3.7 presents the results of the sensitivity study.

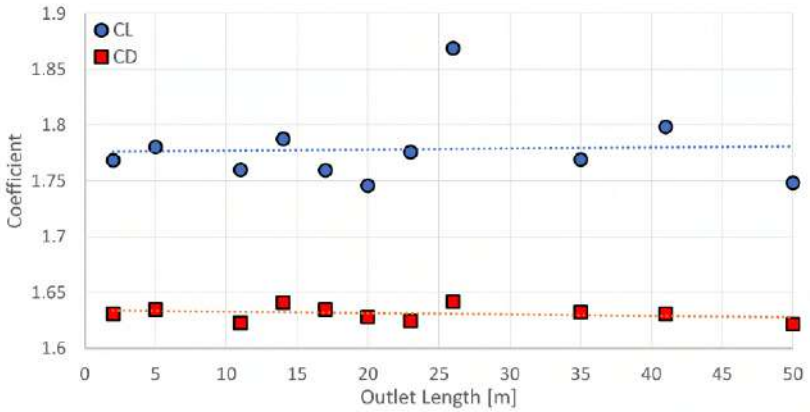

Figure 3.7: Drag and lift coefficients for different outlet lengths.

There is some scatter in the data (most likely a consequence of iterative convergence) although the results show a small influence of the outlet location on the C_L and C_D.

As a consequence, it seemed advantageous to use the $2\,\text{m}$ outlet zone to minimize the domain volume. To corroborate the outlet dimension decision, the momentum flux ($\int \rho u(u \cdot \mathbf{n}) dS$) was evaluated (Tab. 3.4) at the entry (x = $1000\,\text{mm}$) and exit (x = $-2750\,\text{mm}$) of the test section. One more time, the values show small differences especially when the *x* value is considered.

Table 3.4: Momentum flux at entry and exit of the test section.

	Entry section ($x = 1000\ mm$)			Exit section ($x = -2750\ mm$)		
Outlet dimension	50 m	2 m	$\Delta\%$	50 m	2 m	$\Delta[\%]$
$Magnitude$ [N m^{-2}]	2868.78	2871.46	0.09	1289.23	1340.77	4.00
$x - Flux$ [N m^{-2}]	2866.69	2869.54	0.10	1249.06	1288.70	3.17
$y - Flux$ [N m^{-2}]	1.10	1.02	6.80	14.80	21.98	48.54
$z - Flux$ [N m^{-2}]	0.99	0.90	9.76	25.37	30.09	18.61

The higher values obtained to the *y* and *z* delta values are expected. These differences are related to the steadiness condition of the simulation and also to the iterative convergence effects. Moreover, these effects are visible in Fig. 3.8 due to the change in the wake orientation for $2\,\text{m}$. It shows the difference in the total pressure coefficient at the center section ($y = 0\,\text{m}$).

Ground

Typically, the presence of a ground plate changes the flow field. It is especially prominent for cars with low ground clearance or those that rely on ground effect. Like the outlet study, a ground study was

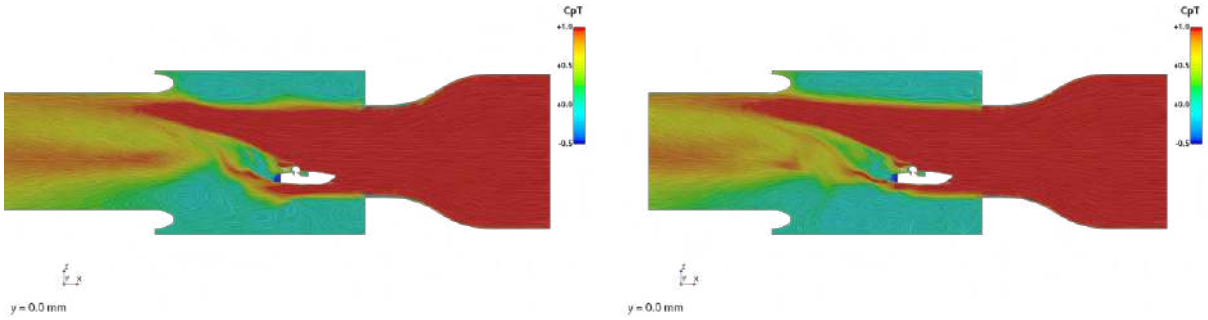

(a) Outlet 50 m. (b) Outlet 2 m.

Figure 3.8: Total pressure coefficient at the center section (y = 0 mm).

performed (in a preliminary phase) to understand how the ground dimensions affected the model forces. General dimensions were utilized in this study.

Despite the car model being around 1 m long and 0.5 m wide, the ground must be substantially larger to not cause dependency on lift and drag coefficient, as seen in Tab. 3.5. Taking into account this study, a 2 m long, 1 m wide and 3 mm thick aluminium plate was installed in the wind tunnel.

Table 3.5: Lift and drag coefficients for different ground dimensions.

Ground Dimension	2000x900x5	1200x600x5		1400x600x5		2350x1100x5	
C_L	3.314	3.053	(-7.86 %)	3.153	(-4.86 %)	3.327	(0.41 %)
C_D	1.556	1.496	(-3.83 %)	1.494	(-4.01 %)	1.558	(0.11 %)

The option of using a moving ground and a model with rotating wheels were early discarded due to facilities conditions. Nonetheless, a study was conducted to understand how the different motions and boundary conditions (BC) affect the lift and drag coefficients, as seen in Tab. 3.6. The major difference between these coefficients was noticed for the moving ground (MG) and rotating wheels (RW). Therefore, this result can not be neglected whenever a comparison with on road testing is made.

Table 3.6: Lift and drag coefficients for different ground and wheels boundary conditions.

BC	No Slip	Slip		MG		MG and RW	
C_L	3.314	3.231	(-2.49 %)	3.304	(-0.28 %)	3.019	(-8.91 %)
C_D	1.556	1.526	(-1.95 %)	1.533	(-1.46 %)	1.500	(-3.57 %)

3.2.4 Mesh

The car was modelled in *Solidworks*® and then imported to *StarCCM+*®. Despite being a simplified model version of the FST 10e, the car model still presented a complex geometry. Indeed, the car model importation to *StarCCM+*® did not provide a clean geometry. To ensure that no geometric errors affected the results, a *surface wrapper* feature was applied as seen in Fig. E.1. Even though this feature is time

consuming, it cleans the geometry getting it ready for meshing since it does not require further boolean operations.

Three volumetric controls (Fig. 3.9.b)) were used to refine specific zones of the model, particularly surfaces with strong adverse pressure gradients, for example, the front wing and lateral diffusers. This assured that small phenomena that might affect the airflow were captured during the simulations. In addition, five volumetric controls (Fig. 3.9.a) were also used to smooth the volume mesh growth. These controls encompass not only the car but also its wake.

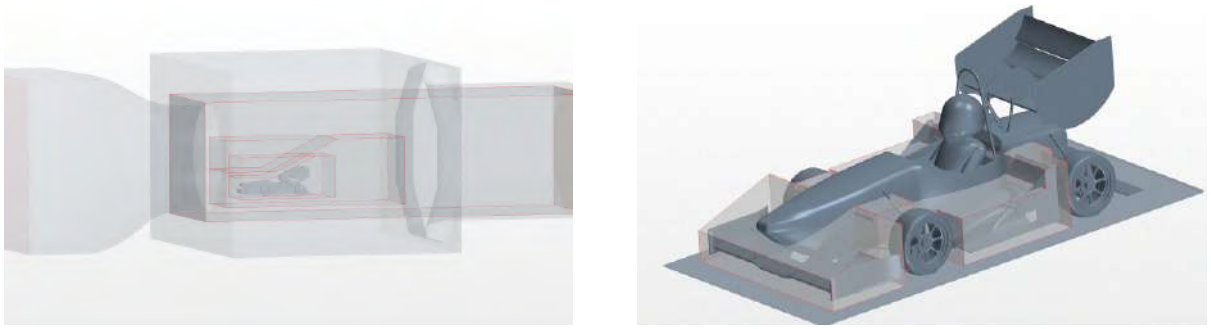

(a) Domain

(b) Front wing and lateral diffuser

Figure 3.9: Volumetric controls.

StarCCM+® offers three main distinct meshers: Tetrahedral, Trimmed and Polyhedral. The latter was chosen to discretize the domain, Fig. 3.10 presents an overall overview of the polyhedral mesh and Fig. E.2 shows the surface mesh of some car components. This mesher is time consuming, although it requires fewer iterations to converge the solutions. Thus, the solver simulation time is lowered. Moreover, polyhedral cells are constructed from a group of tetrahedral cells that present a successful adaptation to complex geometries, particularly where high refinement is required. However, this adaptive process is time expensive [42, 43]. A convergence analysis was performed to get the best compromise between mesh refinement and simulation solver time (refer to Sec. 3.2.5).

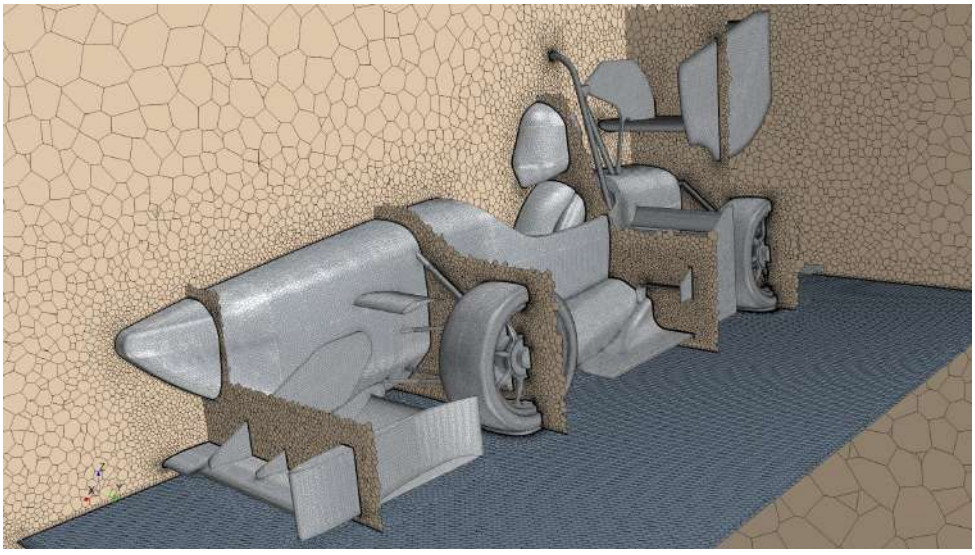

Figure 3.10: Polyhedral mesh.

Focusing on aerodynamic purposes, the inner region of a boundary layer must have a high resolution to catch and accurately predict transition and separation phenomena, on which lift and drag forces are highly dependent on it. The $k-\omega\ SST$ can be coupled with wall treatment models, which model each sublayer using different empirical approaches. $Wall\ y^+$ is a non-dimension distance that defines the extension of the sublayers as seen in Fig 3.11.(a),

$$y^+ = \frac{y\rho u_\tau}{\mu}, \tag{3.3}$$

where y is the normal distance to the wall, u_τ the friction velocity and can be calculated by $u_\tau = \sqrt{\frac{\tau_w}{\rho}}$, where τ_w is the wall shear stress. To ensure that the whole boundary layer airflow was captured, a prism layer mesh was generated on every surface of the ground and car, targeting a $wall\ y^+$ smaller than five as seen in Fig. 3.12[2]. This value guarantees that the first mesh node is located inside the viscous sublayer enabling the low y^+ wall treatment presented in Fig. 3.11.(b).

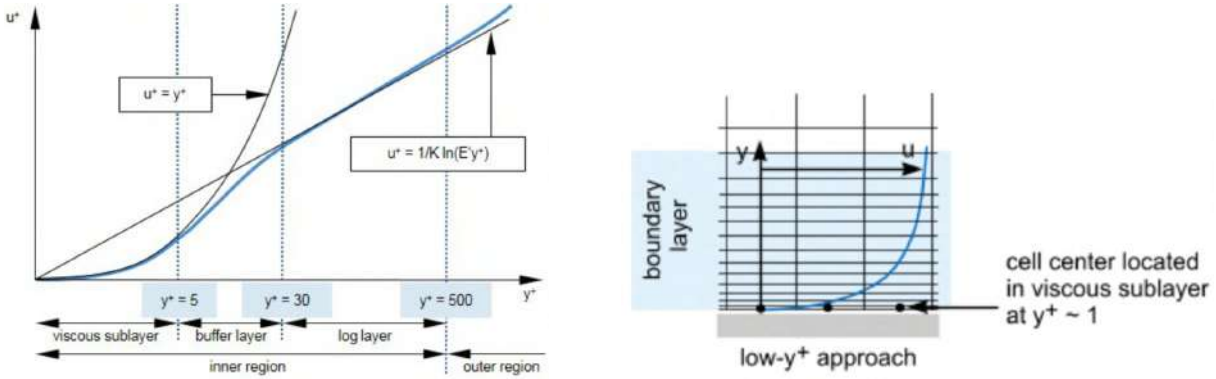

(a) Bounday layers sublayers.

(b) Low y+ treatment.

Figure 3.11: Boundary layer treatment.

The front wing is the first component to be reached by the incoming airflow, meaning that is almost the only component to be surrounded by laminar airflow. As expected, the rearwards components are subjected to greater turbulence leading to an increase in the boundary layer thickness. Accordingly to the component being discretized, the prism layer mesh parameters (such as the number of prism layers and total layer thickness) were changed to capture the entire boundary layer.

As a result, the total number of mesh elements increased substantially, thereby the computational capacity required increased as well. In order to minimize the number of elements used in the numerical simulations, the prism layers of the suspension and wheels assembly were disabled since these components are responsible for a very small part of the aerodynamic forces. Table 3.7 presents a comparison between using prism layers on the whole car (Prisms) and not using prism layers on the wheels assembly surface (No prisms).

Despite not being aerodynamic components, the wheels affect the overall airflow around the car. The prism layers enabled a better definition of the airflow around these complex components. Table 3.7

[2]The limits concerning the logarithmic layer are highly dependent on the Reynolds number. For very high Reynolds number both limits can be located much further from the wall. For instance, studies regarding turbulent boundary layer for very high Reynolds numbers performed by Vallikivi et al. [44], revealed that the logarithmic regions can be defined as high as $400 \leq y^+ \leq 0.15Re_\tau$, where $Re_\tau \gg 20\ 000$.

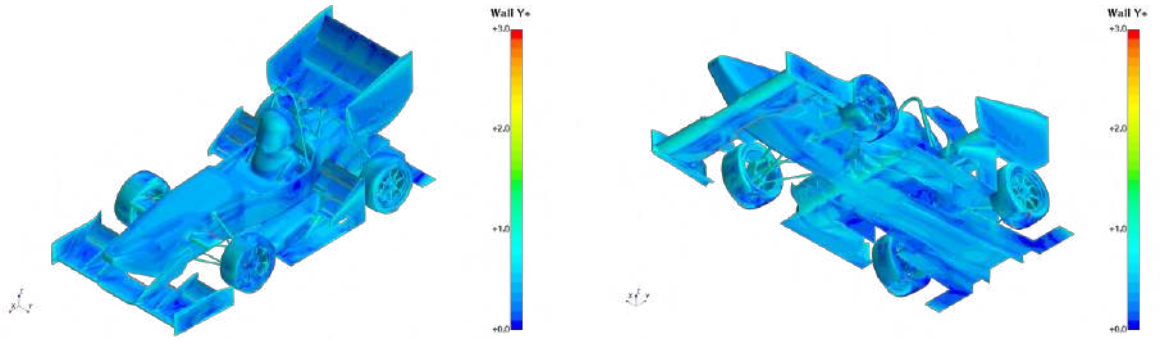

(a) Top view (b) Bottom view

Figure 3.12: Mesh $Wall\ y^+$ of mesh 3.

Table 3.7: Lift and drag coefficients comparison between a having prism layers at all car surfaces and disable prisms layers at the wheels assembly (No prisms simulation).

	Overall		Front wing		Lateral diffusers		Rear wing	
Simulation	C_L	C_D	C_L	C_D	C_L	C_D	C_L	C_D
Prisms	2.588	1.455	0.600	0.083	0.867	0.559	0.975	0.103
No prisms	2.996	1.473	0.819	0.113	0.916	0.569	1.023	0.117
Difference	15.8 %	1.2 %	36.6 %	36.1 %	5.6 %	1.8 %	4.9 %	13.3 %

shows a significant difference, in particular, in the front wing coefficients.

3.2.5 Numerical Error

The numerical error $e(\phi)$ of a variable can be expressed as the difference between the approximated solution ϕ_i and the exact solution ϕ_{exact} [45],

$$e(\phi) = \phi_i - \phi_{exact}. \tag{3.4}$$

When solving non-linear differential equations with a numerical method, the errors can derive from [45–47]:

- Round-off errors - Occur due to the representation of real numbers by a finite number of significant digits in computers. To calculate the round-off error, it would be necessary to know the exact solution of the discrete problem, which is not possible;
- Iterative errors - Caused by several features of the solution procedure: linearisation methods, segregated models, differed corrections to obtain second order (or higher) equations in discretization and the iterative methods used to solve the solver linear equations;
- Discretization errors - The transformation of differential equations, embraced by the mathematical models into algebraic equations leads to these errors. To solve the models computationally, grid cells populate a domain where algebraic equations are solved. This causes a finite spatial resolution and, if unsteady conditions are considered, a limited time resolution is included.

The numerical calculations were performed with a *StarCCM+*® version that provides double precision[3], in which each floating data point occupies 8 bits and has 15 precision digits. The lower round-off error increases the accuracy of the solutions leading to robust convergences of problems.

Numerical simulations solve the algebraic equations to provide approximate solutions to the governing equations of the problem. One of the main concerns is to guarantee that these solutions are approaching the exact solution. Since the exact solution is an unknown quantity, the solution convergence can be evaluated by its consistency and stability [47]. The residuals of the governing equations are the main quantities to guarantee the solution convergence. Nevertheless, it is also essential to study the behaviour of the quantities of interest. Thus, the convergence of the residuals of the governing equations (momentum in each direction, specific dissipation rate, TKE, continuity and intermittency), the six aerodynamic loads and the center of loads (which gives an approximate location of the center of pressure of the car) were analysed. All non-normalized residuals dropped below 10^{-3}, except the continuity residual that only achieved the 10^{-2} order. However, the other quantities of interest were also considered converged.

When complex geometries and surfaces with heavy curvature are used, discretization errors can be dominant. Nevertheless, they can be theoretically decreased by increasing the mesh degrees of freedom, whereas the two other types of errors increase [45, 48].

An exact solution ϕ_{exact} is needed to determine the discretization error $e(\phi_i)$. However, this is only possible if round-off and iterative errors are negligible compared with the discretization error. Since double precision reduces the round-off error and the solution convergence was achieved, the discretization errors were considered to be the main factor in the numerical error.

Several error estimators are available in the literature. Yet, only the the least-squares error estimation method was applied. This method requires a mesh convergence study with at least three geometrically similar grids. The discretization error presents the following behaviour [49]:

$$e(\phi_i) = \phi_i - \phi_{exact} = \alpha h_i^p, \tag{3.5}$$

where α is the error constant, p the convergence order and h_i is the typical cell size (know as refinement ratio as well), defined by $h_i = \sqrt[3]{\frac{N_1}{N_i}}$, where N_i stands for number of elements of each mesh and N_1 for the number of elements of the finest mesh.

The aerodynamic forces are extremely important for this work since they will be compared against the wind tunnel forces. Thus, the lift, drag and pitch moment coefficients were the main variables analysed during the mesh convergence analysis for the five distinct geometrically similar meshes created. Their results are summarized in Tab. 3.8, where the total solver time (TST) is included for reference.

Coupled with the least-squares error estimation method, the Richardson extrapolation method was used to estimate the exact value of lift (C_L), drag (C_D) and pitching moment (C_M), -2.414, 1.329 and -0.098 respectively as illustrates Fig. 3.13.

Despite the finest mesh (mesh number 5) presenting the lowest error and uncertainty, it was decided to continue the studies with mesh number 3, which has r_i = 1.29 and an estimated error for the lift (C_L)

[3]Precision refers to the number of precision digits that are stored for a floating point data.

Table 3.8: Convergence and discretization errors results.

	Convergence analysis						Estimated error - $e(\phi)$		
Mesh	N_i $[\times 10^6]$	h_i	TST $[h]$	C_L	C_D	C_M	C_L	C_D	C_M
1 (Coarsest)	5.343	1.73	8.5	-2.183	1.441	-0.290	0.206	0.106	0.191
2	9.443	1.45	14.8	-2.354	1.370	-0.149	0.165	0.073	0.131
3	13.68	1.29	17.5	-2.182	1.408	-0.202	0.141	0.057	0.102
4	24.18	1.06	27.9	-2.258	1.354	-0.163	0.114	0.039	0.070
5 (Finest)	29.04	1.00	37.2	-2.361	1.373	-0.163	0.106	0.034	0.062

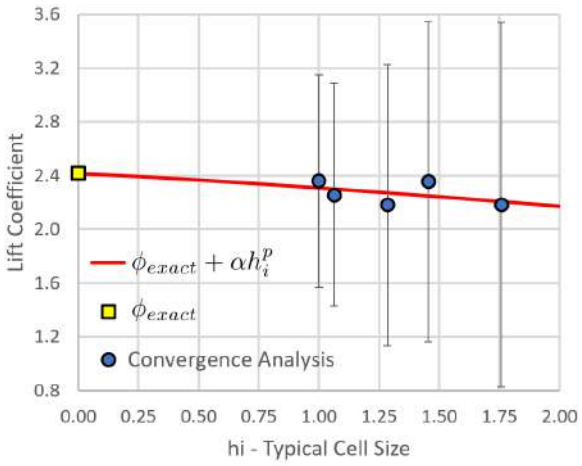

(a) Lift coefficient.

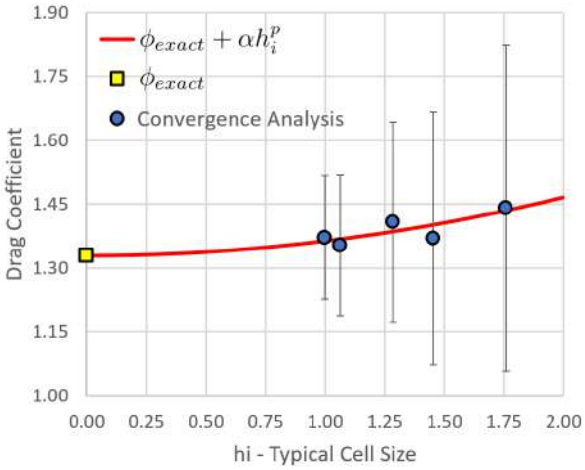

(b) Drag coefficient.

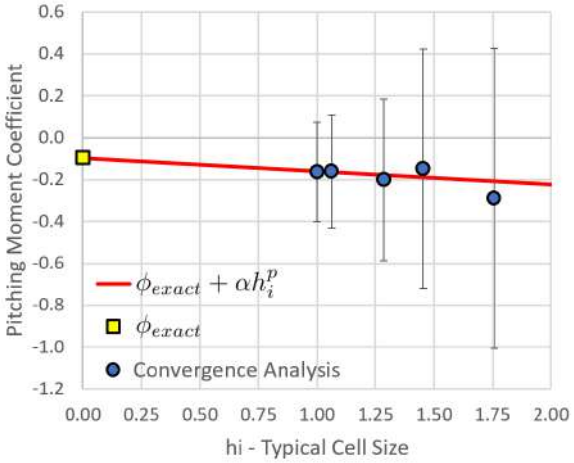

(c) Pitch moment coefficient.

Figure 3.13: Numerical error uncertainties.

and drag (C_D) coefficients of 5.8 %, 4.3 % respectively. Since the pitching moment depends on both lift and drag forces, its error presents the same order of the lift and drag coefficients. Mesh 3 represents a good compromise between numerical accuracy and simulation time. It still presents good grid resolution around the car, catching important phenomena that are lost in meshes 1 and 2.

Chapter 4

Formula Student Model

This chapter discusses the process and design decisions of the wind tunnel model including the manufacturing process of the physical model. Also, a brief study concerning the aerodynamic balance is presented to ensure its structural integrity during the wind tunnel experiments.

4.1 Wind Tunnel Car Model

The model geometry preparation began with the FST latest prototype, the FST10e (Fig. 4.1). Its geometry was simplified before defining the testing position and model scale. External systems that could not be reproduced or did not have a large impact on the aerodynamics of the car were eliminated, such as the cooling system and electrical wires. Other components suffered small changes, for instance, the cockpit was closed, the sharp edges of the wheel assembly were smoothed and the thickness of the flaps trailing edges was increased to $0.5\,\mathrm{mm}$ to ease manufacturing.

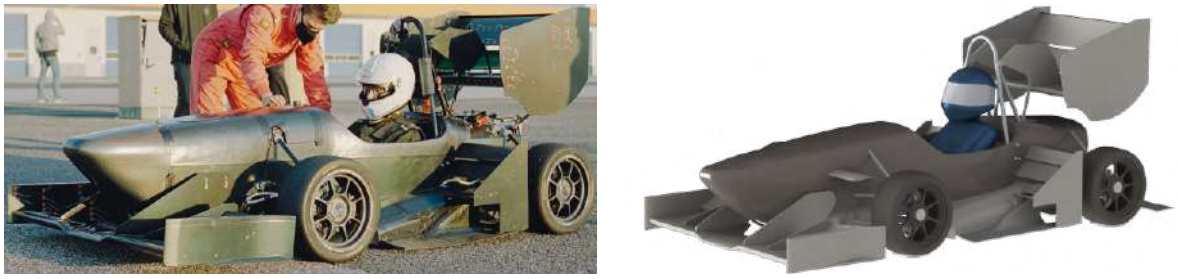

(a) Full size vehicle.

(b) Wind tunnel model.

Figure 4.1: FST10e design.

4.1.1 Flow Similarity

The model position within the wind tunnel test section and the model scale had to be studied together because these variables are not independent of each other. The airflow characteristics also have a significant effect on these decisions. Thus, several constraints must be accounted for:

Reynolds Similarity

In a low speed wind tunnel, the airflow is moving around a model in study which disturbs the flow field, generating aerodynamic forces. The intensity of these forces depends on the model shape and airflow characteristics such as speed, density and viscosity. To recreate the conditions of road testing, aerodynamicists rely on similarity parameters for the different quantities. When two different flows present the same values for the similarity parameters, forces are being modelled correctly [8].

Reynolds number is a dimensionless number that correlates the ratio between inertial forces and viscous forces

$$Re = \frac{\rho V l}{\mu}, \tag{4.1}$$

where l relates to the reference length. The Reynolds number also indicates if the flow is laminar or if it suffers transition to the turbulent regime.

To guarantee Reynolds similarity, assuming equal air density and viscosity, the airspeed must scale with the inverse of the characteristic length,

$$Re_{car} = Re_{model} \Rightarrow \frac{\cancel{\rho_{air}} V_c l_c}{\cancel{\mu_{air}}} = \frac{\cancel{\rho_{air}} V_m l_m}{\cancel{\mu_{air}}} \Rightarrow \frac{V_m}{V_c} = \frac{l_c}{l_m}. \tag{4.2}$$

Wind Tunnel Facility

The wind tunnel has a $3\,\mathrm{m}$ long test section with a round inlet of $1.5\,\mathrm{m}$ diameter. This section is an anechoic camera covered by triangular shaped foams, which decreases noise reflection. Beyond that, there are some aluminium structures inside the test section, that make it possible to walk inside the camera. These features worked as constraints to define a position for the model.

Finally, the model should be located inside the uniform flow region, as characterized in Sec. 2.9.

4.1.2 Position and Scale Definition

To minimize the forces and moments suffered by the balance, the balance arm support should be as small as possible. Since there was already a $0.455\,\mathrm{m}$ balance arm support tube mounted with a system that regulates the pitch of the model, it was decided to use it. Instead of redesigning this support, the time was spent designing and manufacturing a support frame that supports the whole balance, as mentioned in Sec. 2.8.

Considering the available area inside the test section, the model was located as close as possible to the inlet to make sure it would be located inside the potential core of the airflow jet. Thus, the model was fixed at $-0.55\,\mathrm{m}$ in z axis and $0.8\,\mathrm{m}$ in x axis from the center of the wind tunnel inlet.

The next step was to define its scale. Numerical simulations[1] of the airflow were performed to evaluate how the airflow energy behaves inside the wind tunnel. Analysing the total pressure coefficient, the available lateral distance where there is almost no losses (red colour) is around $0.4\,\mathrm{m}$ for each side

[1] These simulations were performed without a model.

as seen in Fig 4.2.(a). Since a flat plate was needed under the car to reproduce the ground, it should be larger than the model. Thus, the lateral distance available for the model shrinks even more. In addition, the wind tunnel characterization (anemometry) could not be performed prior to this definition. Consequently, a higher margin was considered, the model scale should not be higher than 1/3 of the real one.

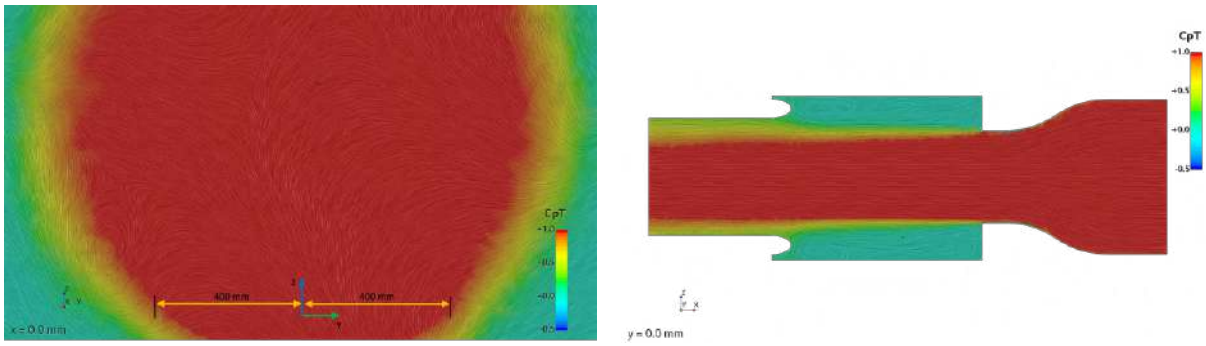

(a) x = 0 mm. (b) y = 0 mm.

Figure 4.2: Total pressure coefficient inside the empty test chamber.

Knowing that the FST10e average speed when competing is around $15\,\mathrm{m\,s^{-1}}$, and the maximum speed of the wind tunnel is around $45\,\mathrm{m\,s^{-1}}$, a 1/3 scale model was built to assure Reynolds similarity (Eq. 4.2).

Afterwards, a CFD simulation was performed with the model in place to verify its position within the jet potential core. The red colour in Fig. 4.3 represents zones with no losses, where the car should be located. This position was considered reasonable despite the most rearward section of the model being slightly affected by the jet shear layers.

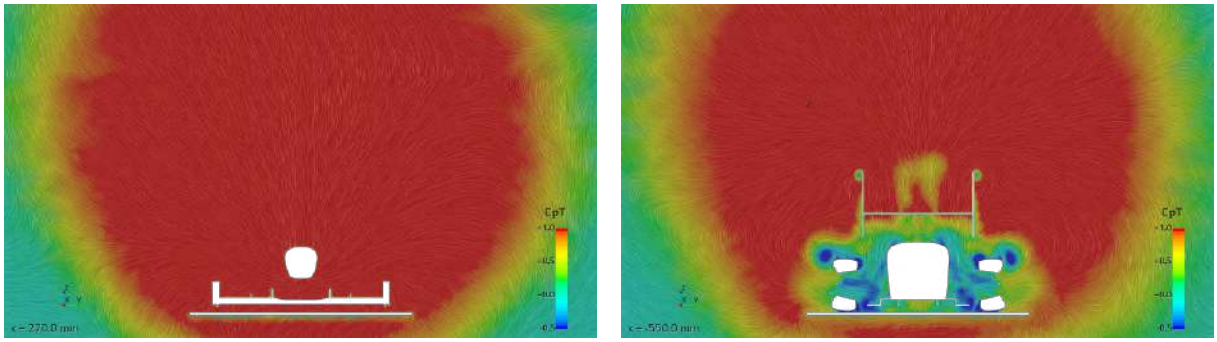

(a) Nose and front wing (x = 270 mm). (b) Monocoque rear end and rear ring (x = −550 mm).

Figure 4.3: Total pressure coefficient with model installed on the balance.

Airflow Velocity

As referred to in Sec. 2.8, the maximum velocity of the wind tunnel motor is 1500 RPM. However, for safety reasons, the motor was limited to 1000 RPM, which is around $43.5\,\mathrm{m\,s^{-1}}$. Much later, during the hot wire anemometry test, it was noted that the wind tunnel does not maintain the air temperature when operating at high speeds. This enhanced the need to decrease, even more, the airflow speed of the

experimental tests. Hence, it was set to $25\,\mathrm{m\,s^{-1}}$. At the same time, the scale of the model was already defined. Thus, the Reynolds similarity initially defined was not respected. However, the main concern of this study is to match the wind tunnel Reynolds number with that of the CFD simulations.

New Position

Some problems emerged during the balance support construction which implied the most forward position for the aerodynamic balance to be shifted $0.4\,\mathrm{m}$ backwards and the model to be $0.05\,\mathrm{m}$ higher than expected. This new position, presented in Fig. 4.4, was expected to still be inside the jet core, so no further numerical tests were made.

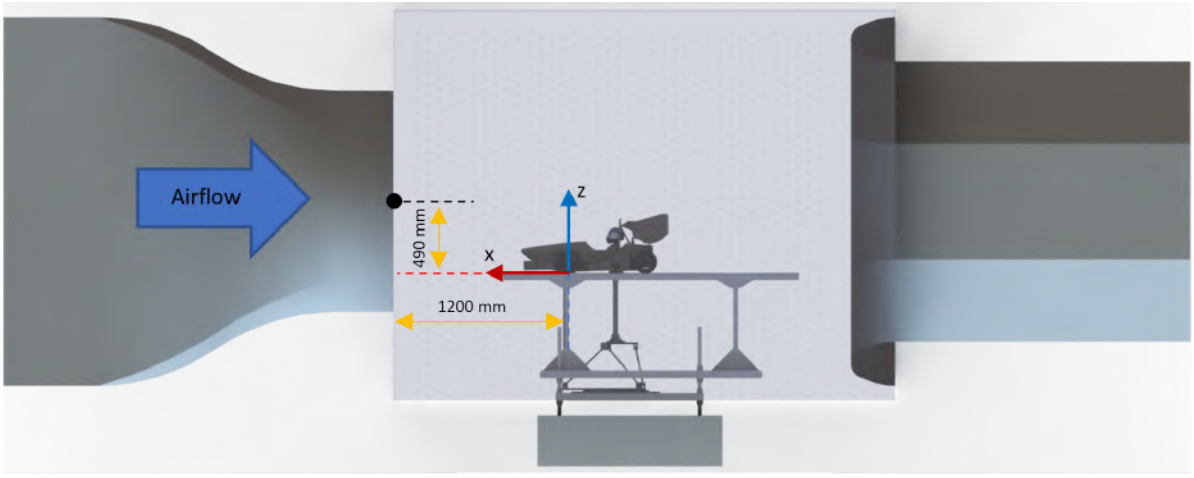

Figure 4.4: Model position inside the test section.

4.2 Manufacture

As stated in Sec. 4.1.2, the wind tunnel model is a 1/3 scale model of the FST10e. Despite being considerably smaller and simpler than the prototype itself, it is still approximately $1\,\mathrm{m}$ long, $0.75\,\mathrm{m}$ wide and $0.6\,\mathrm{m}$ tall. The integration of the different assemblies raised its complexity, which was taken into consideration during the design phase.

4.2.1 Manufacturing Principles

The following points were the main constraints during the model design and manufacturing process.

Withstand High Loads

Both, the wind tunnel model and the aerodynamic balance, have not only to withstand their own weight but also the aerodynamic loads produced. Section 4.3 contains further information concerning the balance structural integrity.

Physical Models Evaluation

Pressure readings are key to evaluate the airflow evolution and to enabling the validation of the numerical models. In this context, pressure taps were added to the front wing suction side main plane, the monocoque nose (Fig. 4.5.(b)), the rear wing main plane suction side (Fig. 4.6.(b)) and inside the lateral diffuser. In the latter, it was noticed (through CFD simulations) that the mesh refinement in that area had a large impact on the lateral diffuser performance. Thus, it was important to verify the boundary layer behaviour.

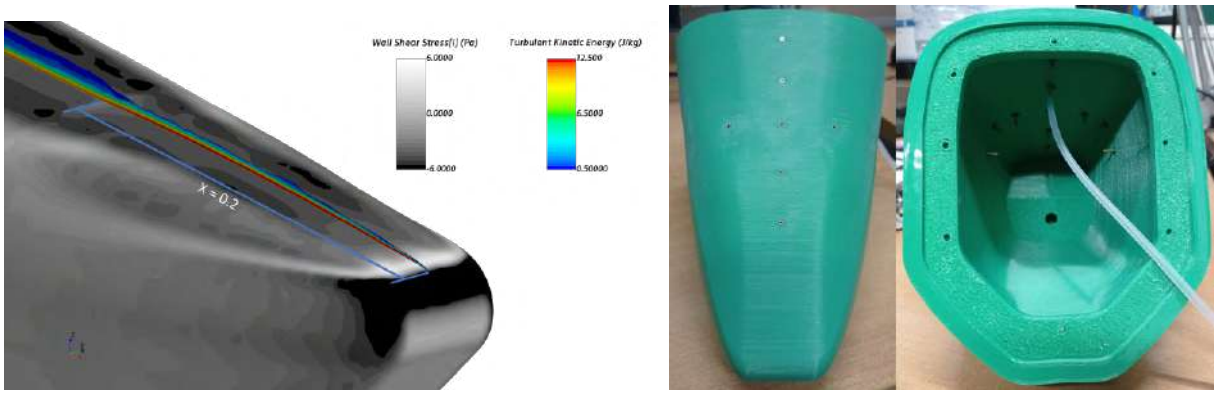

(a) Monitoring points in the numerical simulations

(b) Pressure taps for the wind tunnel model instrumentation.

Figure 4.5: Physical models evaluation.

Hollow Interior

Some measures were taken to neither obstruct or modify the airflow. The main planes of the front and rear wings and the lateral diffuser are hollow to accommodate the pressure taps and the silicon tubes (Fig. 4.5.(b) and 4.6). Also, the monocoque has a hollow design (Fig. 4.6.(a)) as well to accommodate the pressure sensor itself.

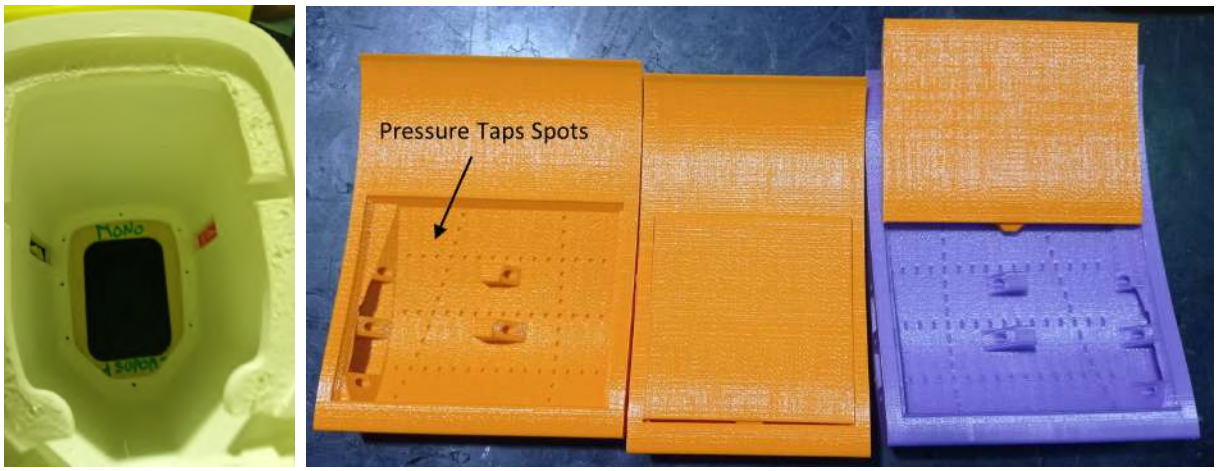

(a) Monocoque.

(b) Rear wing main plane.

Figure 4.6: Hollow components.

Modular Design

A modular design was adopted to ease the model manufacture. The model is divided into several assemblies which consist of dozens of parts joined together. Although it raised the model complexity, it made it possible to test distinct car configurations without manufacturing a whole new section. Some examples of the car modules can be seen in Fig. 4.7.

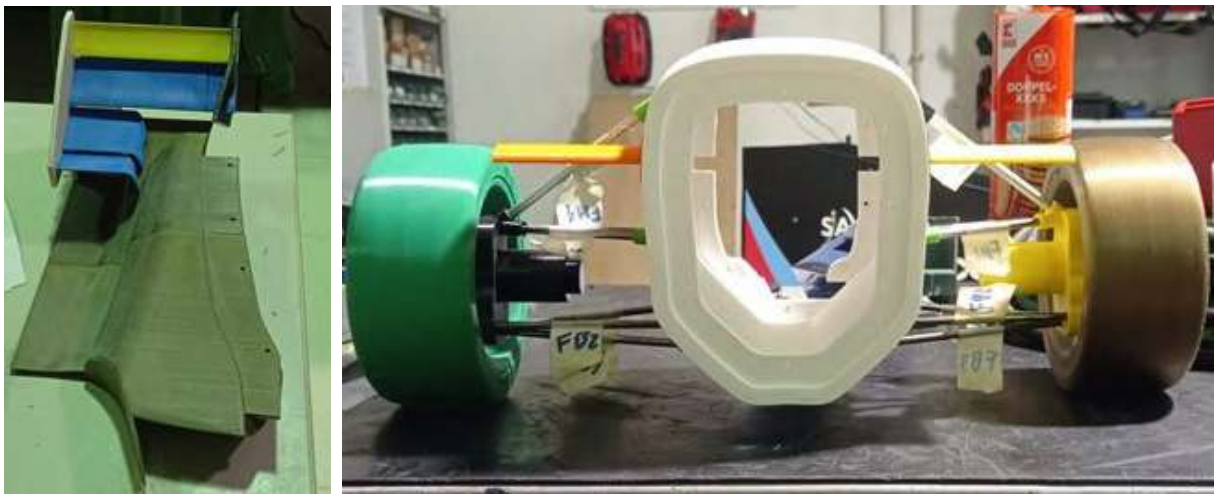

(a) Lateral diffuser and side cascade.

(b) Front axle section.

Figure 4.7: Model modular assemblies.

Balance Mounting

To minimize the transmission of loads, the attachment points between the monocoque and the balance are located as close as possible to the center of pressure of the model. At this point, the resultant of the aerodynamic forces can be solved (lift, drag and lateral force) and the moments are zero (roll, pitch and yaw) [50]. In reality, the center of pressure is not a point. On the road, a car is continuously changing configuration, inducing shifts in the center of pressure. However, for a steady flow of a wind tunnel, the pressure center does not change significantly its position.

The model center of pressure location was estimated through CFD simulations. The *StarCCM+*® *center of loads* feature intends to locate the point where only the fluid flow pure forces are acting. However, for 3D geometries, it is not always possible. This feature locates the line of action of the aerodynamic resultant force, so it needs a reference (plane or an input surface) that crosses that line, denominating the intersection point as *center of loads*. Since the balance arm supports the model by the lower surface of the monocoque, three reference planes around that lower area plus the input surface option were defined to calculate several centers of loads. Figure 4.8.(a) illustrates the line of action of the aerodynamic resultant force, where z = 0 refers to the ground plane, z = 16.3 mm corresponds to the monocoque plane[2] and, finally, the plane z = 25mm corresponds to the middle of the monocoque lower

[2]The monocoque plane is cordial to the lowest part of the monocoque. Note that the monocoque presents a 3° rake angle at the rear.

wall. The latter intersects the monocoque wall at the forces line of action, therefore, it was used as the center point for the balance arm attachment.

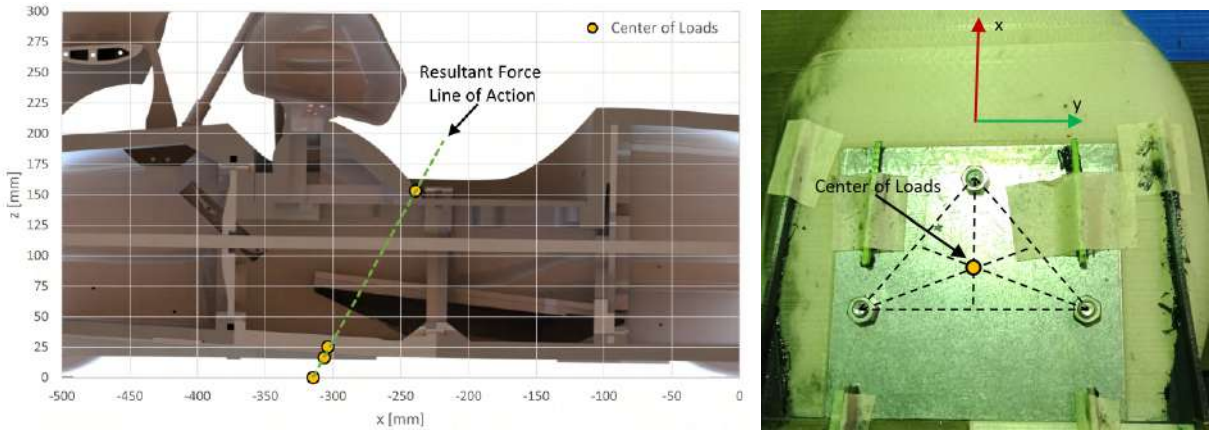

(a) Center of loads positions.

(b) Model attachment points.

Figure 4.8: Center of loads.

Taking into account the position of the *center of loads* at z = 25 mm, a triangular shape attachment was designed to increase stability during experiments, as shown in Fig. 4.8.(b).

As expected, the balance attachment method above described not only brought some problems but has also raised the design complexity of the system. Moreover, a large hole on the ground plate (Fig. 4.9.(b)) was necessary to attach the model to the aerodynamic balance. The attachment between the balance and the monocoque is made at the bottom of the monocoque cockpit. First, three threaded rods are used to secure the monocoque interior to the base plate, which is bolted to the balance arm support, as seen in Fig. 4.9.(a). Second, three aluminium spacers (component 4) hold both components to minimize the interferences with the incoming airflow. Third, two steel plates (components 6 and 7) were added to both sides of the monocoque bottom wall to spread the loads by a larger area. Four, since the aluminium spacer tubes (component 4) might cause airflow separation, an attachment cover (component 2) was designed with three NACA 0030 airfoils that lodge the aluminium tubes. Also, the rearwards airfoils were designed at the same angle as the diffuser strakes (Fig. 4.8.(b)) to minimize the geometry changes. The bottom part of the component is round to enable a change of the model yaw angle (lateral wind conditions can be recreated).

A 5 mm gap located between the balance support arm (component 8) and the ground (component 3) prevents any load transfer between these components. However, it has to be sealed to ensure that no air passes through, which would change the airflow. To solve it, several pieces of transparent tape were strategically glued to the ground (component 3) and the attachment cover (component 2). On one side, the tape is glued just to the component located upstream and it lays down on top of the other component.

Reinforcements

The highest loads are generated in the front wing and rear wing components. Since these parts are located on the opposite sides of the model, the monocoque is subjected to large bending loads. Since

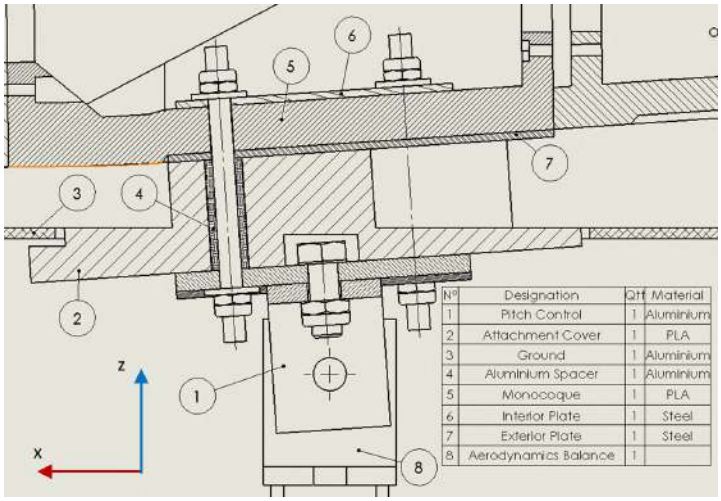

(a) Attachment scheme.

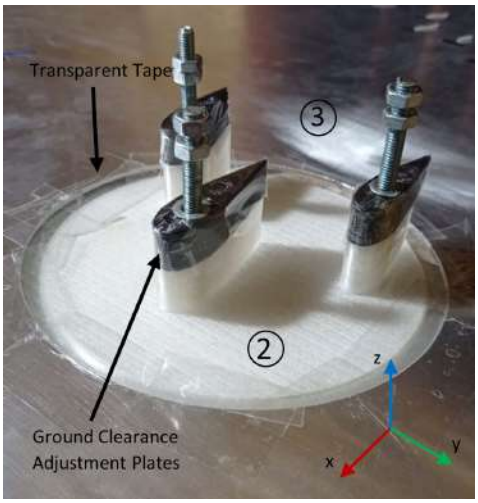

(b) Model attachment points.

Figure 4.9: Attachment of model to balance.

the model is sustained by the lower part of the cockpit, the distance from the attachment point to the aerodynamic components is significant, so four plywood parts were used to reinforce the monocoque.

Accessibility

The model has more than 100 different parts, so the various assemblies must be accessible to replace any component if necessary. The cockpit and rear end of the monocoque can be used to access the model interior. For instance, the attachment points are accessible from the cockpit, which eases the mounting process of the model.

Adjustability

To correlate the wind tunnel experiments with the numerical results, it is necessary to define several configurations for the model. As a result, some model components were designed to reproduce the aerodynamic configurations of the real prototype. As such, the front wing height and the rear wing flaps angle of attack (Fig. 4.10.(a)) can be changed to reproduce the formula student acceleration event car setup. Moreover, the model ground clearance can be changed as well by introducing $1.6\,\mathrm{mm}$ thick PLA plates between the attachment cover NACA profiles and the exterior plate of the monocoque, hereafter referred to as ground clearance adjustment plates (Fig. 4.10.(b)). Each ground clearance adjustment plate has a washer around the threaded rod to prevent the PLA from crushing.

The suspension configuration is also easy to modify. Despite not being directly adjustable, the components that connect the suspension rods to the monocoque were designed to be small and fast to print.

Finally, the general car configuration can also be modified. The balance has a bearing that enables the yaw rotation of the model. Furthermore, the balance arm support has a pitch control part that adjusts the pitch angle. However, to change it a new adjustment cover is required since the angle between the ground and the model must change accordingly. In fact, the ground clearance adjustment plates can be

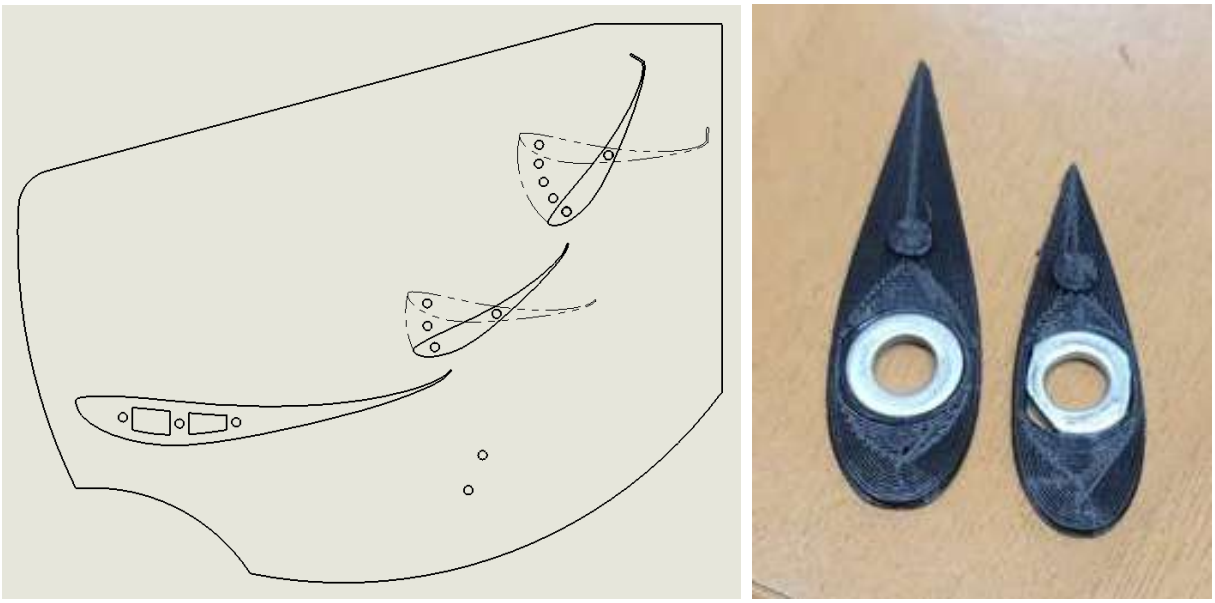

(a) Rear wing. (b) Ground clearance adjustment plates.

Figure 4.10: Model adjustability.

used to perform small pitch and roll changes. Nevertheless, their use is not recommended to achieve precise predetermined configurations.

FST10e Model

The 1/3 scale model weighs 9.35 kg and it is composed of 149 parts, excluding bolts, nuts, etc. Figure 4.11 presents an overview of the general components used to assemble the FST10e model.

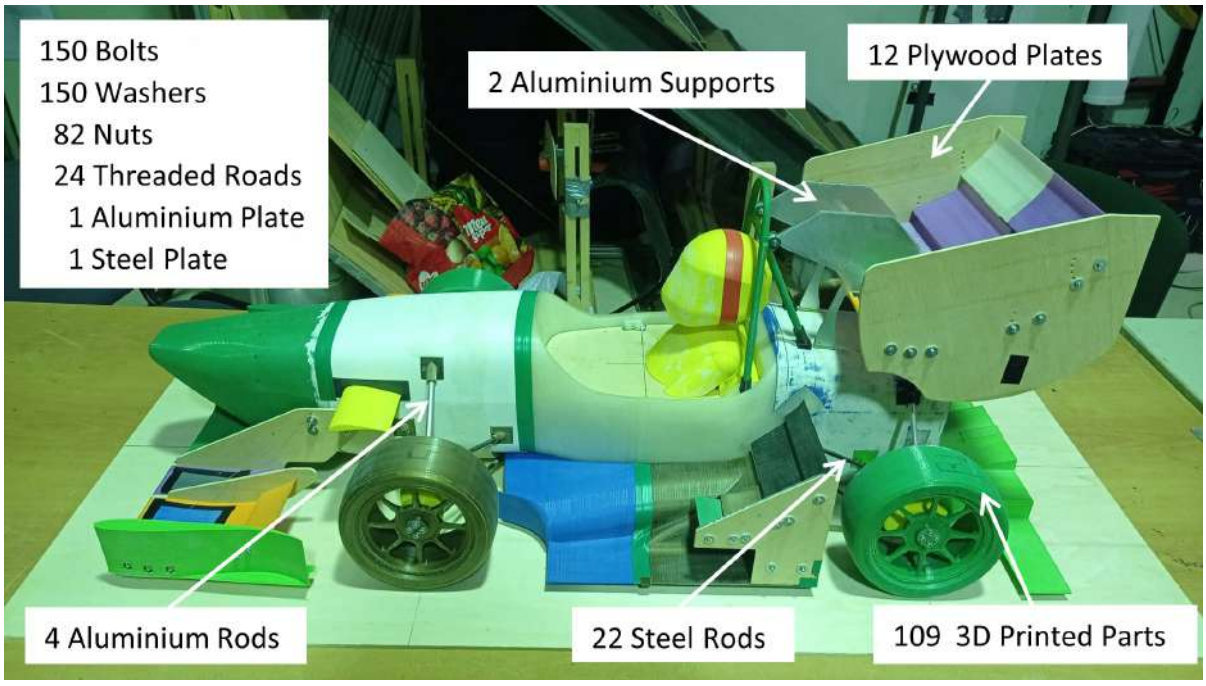

Figure 4.11: Parts used to assemble the model.

The two major manufacturing processes predominantly used were 3D printing and Computerized Numerical Control (CNC) machining. The latter was used to manufacture flat plywood components and the rear wing aluminium supports. On the other hand, the remaining components were 3D printed in Polylactic Acid (PLA). The aerodynamic parts were manufactured through 3D printing, since it enables the creation of complex geometries with a smooth surface, within a reasonable amount of time. To sum up, it took around 60 days to print the whole model.

As stated in Sec. 4.2.1, several components were supposed to have pressure taps, although the pressure acquisition system was not ready to use during the experimental tests. This acquisition system was within the scope of another master thesis. Still, several components were marked with possible pressure taps locations, which were also manufactured but not installed. During the experimental tests, the existing pressure taps were covered with tape to seal the model surfaces.

4.2.2 Printing Process

3D printing is an additive layer manufacturing process, by which the molten material is placed by a numerical controlled extruder.

To keep consistency between the finishing conditions and setting parameters throughout the printing process, the car model was printed using only *Ultimaker*™ machines [51]. One *Ultimaker* 2+™ and one *Ultimaker* 3™ were used to print the majority of the aerodynamic components. Two *Ultimaker* 2+ Extended™ were used to print large components (due to their larger vertical dimension), such as the monocoque parts, main hoop and diffusers.

The open source *Ultimaker Cura*™ (v.4.8.0) software was used to slice the geometry of the components into fine layers and to create a g-code file for the specified printer. An example of the user interface is described in Appendix G.2.

For each printing, a set of settings must be tuned. Some initial printing tests were performed to define the print parameters. For instance, the print parameters of the component presented in Fig. 4.12.(a) were defined to achieve a smooth surface without being time expensive. In other cases, these initial tests deemed necessary to increase the thickness of the trailing edges of the airfoils.

Due to the larger number of components to be printed and their various dimensions, two distinct printing profiles were defined: one for the aerodynamic components and one for the larger parts. Focusing on the second, the printing speeds were increased around 25% and the layer height was increased from 0.15 to $0.2\,\mathrm{mm}$. Moreover, the walls that act as a support for the higher load components (for example, the front wing attachment, the rear wing attachment and the bottom wall of the cockpit) were reinforced with high infill density (around 60%). Refer to Appendix G.2 for the full settings.

To mitigate any assembly problems, fitting tests (see Fig. 4.12) were performed at an early stage. A surface offset of $0.1\,\mathrm{mm}$ was applied to every surface where two printed parts are in contact. Also, special attention was given to the suspension assembly. A $0.4\,\mathrm{mm}$ surface offset was applied to achieve thigh joints between the steel rods and the printed connections, to ensure the assembly rigidity.

More than 500 hours of printing time and $8\,\mathrm{kg}$ of PLA material were necessary to complete the man-

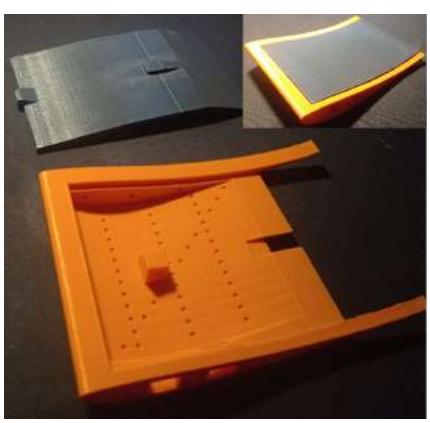

(a) Hollow flap first iteration.

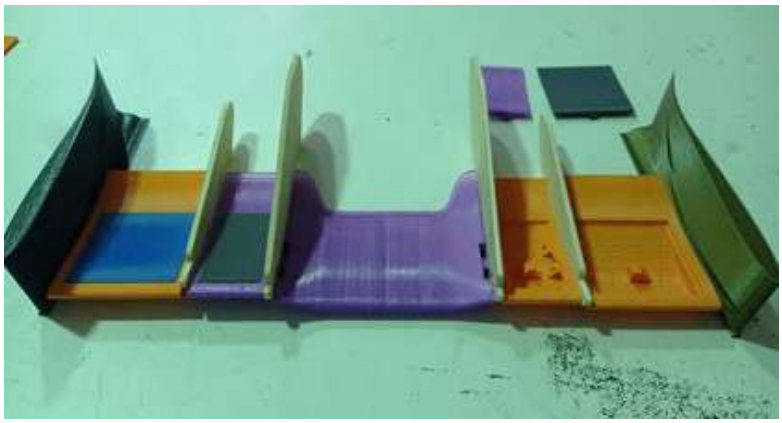

(b) Front wing fitting test.

Figure 4.12: 3D printing tests.

ufacture of the 3D print components. The monocoque of the model was particularly challenging to print. Due to its complexity and size, it was divided into five pieces, which combined took around 250 printing hours.

As the printing time increases, also raises the probability of a printer error. *Ultimaker*™ machines do not present a feature to resume printing from the layer it stopped. Therefore, every time an error came up, the print had to be restarted. To solve that, the g-code was modified to start where the error happened. However, it is important to note that, the layers where the printing resumed were considerably weaker. Figure 4.13.(a) show several attempts to print one of the monocoque parts. To improve the stiffness and to seal the surface of the affected components, a silicon adhesive was spread on the surface, as visible in Fig. 4.13.(b).

Finally, the printed components were sanded to smooth, even more, the surfaces exposed to the airflow.

(a) Monocoque part 2 printing attempts.

(b) Monocoque part 5 surface treated with silicon adhesive.

Figure 4.13: Monocoque printing errors.

4.2.3 CNC Machining

CNC machining is a subtractive manufacturing process, in which machine tools are controlled numerically to remove material from a stock piece.

To machine components, its design files (CAD) run through a computer aided manufacturing (CAM) software, which generates a programming code to control the CNC machine. *Solidworks*® was the software used to model the car and also to generate the CAM file. Finally, *InoCONTROL*® software was used to read the CAM files and to perform the setup of the CNC machine. Its features are briefly described in Appendix G.1.

The model has several flat components that are impossible to print using the 3D printers available due to the printing volume dimension. The solution was to machine them using a CNC at *iStart* laboratory at IST. Initially, all components were machined in a plywood stock but, the rear wing supports were fragile due to their low thickness. Thus, they were machined in aluminium a second time (Fig. G.1.(b)).

(a) Plywood flat components. (b) Aluminium rear wing supports.

Figure 4.14: CNC machining.

4.3 Balance Structural Integrity

To ensure that the force balance could cope with the aerodynamic forces, an analytical model and a computational model developed by Oliveira [20] were used. Following his procedure, the balance structural rigidity was verified for the aerodynamic loads expected. The numerical model was used to calculate the forces acting on the sensing bars and lastly, the analytic model reverted the process and estimated the initial forces applied in the support.

The balance numerical model analysis was performed in *Solidworks*® with the same model provided by Oliveira [20]. The forces acting on the six bars were obtained by analysing the Von Misses stresses from the static analysis using sensors (*Solidworks*® feature) in each bar.

The analytical model is a six equations and six variables rigid model simplification that works both

ways, not only to calculate the forces acting in each bar but also can perform the inverse process to verify the models.

The balance uses extensometers to detect the axial deformation of the bar. Then, their signals are converted into strain. Afterwards, knowing the characteristics and proprieties of the bars is possible to compute the critical forces that the bars are suffering. The physical characteristics of the bars, as well as the analysis criteria, are presented in Tab. 4.1. The maximum yield force was calculated from the yield stress (Aluminium 6063-T6) while the P_{cr} refers to the buckling loads. Due to the different sections of the sensing bars, the buckling loads present two values. They were calculated assuming both ends pinned condition. Leaning towards a more conservative approach, the lower buckling value of $P_{cr} = 1239\,\text{N}$ was assumed and used in the calculations [20].

Table 4.1: Dimensions of the testing bars and two analysis criteria values. [20].

	D_t [m]	d_t [m]	Area [m^2]	I [m^4]	*Yield Force* [N]	P_{cr} [N]
Sensing Bar	0.009	0.007	2,51E-05	2,04E-10	6057	1237
	0.01	0.007	4,01E-05	3,73E-10	-	2260

Load Cases

To guarantee Reynolds similarity, the model and balance assembly must sustain at least speeds of $u_x = 45\,\text{m}\,\text{s}^{-1}$. Since the forces and moments sustained by the balance could become quite significant, two load cases were considered to ensure the structural integrity of the load sensing bars, as presented in Tab. 4.2. These load cases were obtained through numerical simulations. The first load case considered a straight line condition with a higher average speed of $u_x = 51\,\text{m}\,\text{s}^{-1}$ (representing $17\,\text{m}\,\text{s}^{-1}$ for the real car). The second was created to present a critical condition by adding a $21\,\text{m}\,\text{s}^{-1}$ lateral wind, three times (scale factor) higher than the maximum registered wind velocity during testing at Circuito do Estoril. To reproduce this condition, the car yaw angle was set to $22.38°$ and the airflow jet to $u_x = 55.154\,\text{m}\,\text{s}^{-1}$. The expected aerodynamic loads are presented in Tab. 4.2.

Table 4.2: Load cases - balance structural integrity.

Load case	$F_x\ [N]$	$F_y\ [N]$	$F_z\ [N]$	$M_x\ [Nm]$	$M_y\ [Nm]$	$M_z\ [Nm]$
Straight	-270	-7	-550 - 100	2	-10	1
Straight with lateral wind	-415	115	-325 - 100	35	-25	-20

Initial predictions set the model weight around $7/8\,\text{kg}$ which could not be neglected to perform the structural integrity study. Since the 3D model was not completed yet, a force of $F_z = -100\,\text{N}$ was considered to represent the weight of the wind tunnel model and other possible components (pressure taps, pressure sensors, structural ribs if needed).

Load Cases Results

Both analytical and numerical models were used to calculate the forces in each bar. Table 4.3 presents the forces related to the straight line condition while Tab. 4.4 shows the forces related to the lateral wind condition. Figure F.1 presents the positioning of the bars within the balance assembly.

Table 4.3: Balance bars forces - straight line Condition.

	Analytical Model			Numerical Model		
	$Force\ [N]$	$Yield\ Force\ [\%]$	$P_{cr}[\%]$	$Force\ [N]$	$Yield\ Force\ [\%]$	$P_{cr}[\%]$
Bar 1	96.58	1.60	(7.81)	96.21	1.59	(7.78)
Bar 2	93.65	1.54	(7.57)	93.85	1.55	(7.59)
Bar 3	23.05	0.38	(1.87)	23.24	0.38	(1.88)
Bar 4	-609.98	10.07	49.31	-609.47	10.06	49.21
Bar 5	-609.00	10.05	26.95	-608.71	10.05	26.93
Bar 6	37.47	0.62	(3.03)	37.02	0.61	(2.99)

Table 4.4: Balance bars forces - straight line condition with lateral wind.

	Analytical Model			Numerical Model		
	$Force\ [N]$	$Yield\ Force\ [\%]$	$P_{cr}[\%]$	$Force\ [N]$	$Yield\ Force\ [\%]$	$P_{cr}[\%]$
Bar 1	10.78	0.18	(0.87)	13.37	0.22	(1.08)
Bar 2	542.28	8.95	(43.84)	539.35	8.90	(43.60)
Bar 3	487.73	8.05	(39.43)	483.81	7.99	(39.11)
Bar 4	-805.48	13.30	65.12	-804.25	13.28	65.02
Bar 5	-709.96	11.72	57.39	-708.99	11.71	57.32
Bar 6	-158.41	2.61	12.81	-155.35	2.56	12.56

As expected, the critical values are found in the straight line with lateral wind condition. The maximum yield force reaches only 13.30% ($Bar\ 4$) of the maximum yield force of 6057 N (Tab. 4.1) while the compressive forces reach 65.02% ($Bar\ 4$) of the lower buckling force. Analysing the yield stress of the whole balance, the maximum stress reaches 98.95 MPa and, once again, is related to the same airflow condition. This value represents only 41.05% of the Aluminium 6063-T6 yield stress (σ_y = 241 MPa). Note that, the values inside the parenthesis are related to traction forces. Thus, these forces do not contribute to the buckling of the bars. In addition, Appendix F presents the points where the minimum and maximum stress were detected through the finite element analysis.

In conclusion, the experimental studies considered were feasible and did not present any chance of causing damage to the aerodynamic balance or its bars.

Chapter 5

Wind Tunnel Test Campaigns

In this chapter, the wind tunnel testing procedure is described and the different model configurations are addressed. Finally, a qualitative validation of the numerical setup was performed through flow visualization methods and aerodynamic loads of several model configurations.

5.1 Model Configurations

The tests performed were the first meaningful wind tunnel validation experiments of the aerodynamics of an FST prototype. Thus, the testing focused just on a straight line condition. Instead of changing completely the car position relative to the incoming airflow, the model was tested at three different ground clearance configurations ($RH1$, $RH2$ and $RH3$) described in Tab. 5.1. The front and rear ride heights are the ground clearance of the monocoque plane at each axle.

Table 5.1: Experimental ride heights (RH).

Configuration		$RH1-LiDAR$	$RH1-NB$	$RH1$	$RH2$	$RH3$	$RH3-DRS$
Ride Height [mm]	Front	10.5	10.5	10.5	15.4	20.0	20.0
	Rear	21.5	21.5	21.5	28.7	35.6	35.6
Variation between tests		LiDAR	No Bullhorns				DRS

The first configuration was tested with ($RH1$) and without bullhorns ($RH1-NB$), which are real wings located near the car nozzle, as seen in Fig. 5.1. The $RH1$ configuration was also tested with a light detection and ranging (LiDAR) ($RH1-LiDAR$ configuration). The Formula Student competition fosters new technological developments. At this point, the competition is leading toward a driven hybrid format between autonomous and human-driven cars. FST team is already designing its second autonomous prototype (the first one to be designed from scratch). The biggest aerodynamic challenge is to integrate the new driverless systems with minimum aerodynamic losses. For instance, the LiDAR, essential for 3D mapping, has to be attached to the car in an unobstructed place to obtain the most reliable data to map the tracks. In the FST11e, the LiDAR will be located at the main hoop, right in front of its rear wing, as shown by Fig. 5.1.

Finally, the third configuration was experimented with two distinct rear wing setups, which were developed for different Formula Student dynamic events, a high downforce setup for the endurance event ($RH3$) and a low drag configuration (recreating a Drag Reduction System (DRS)) for the acceleration event (low drag configuration $RH3 - DRS$), which is illustrated in Fig. 5.1.

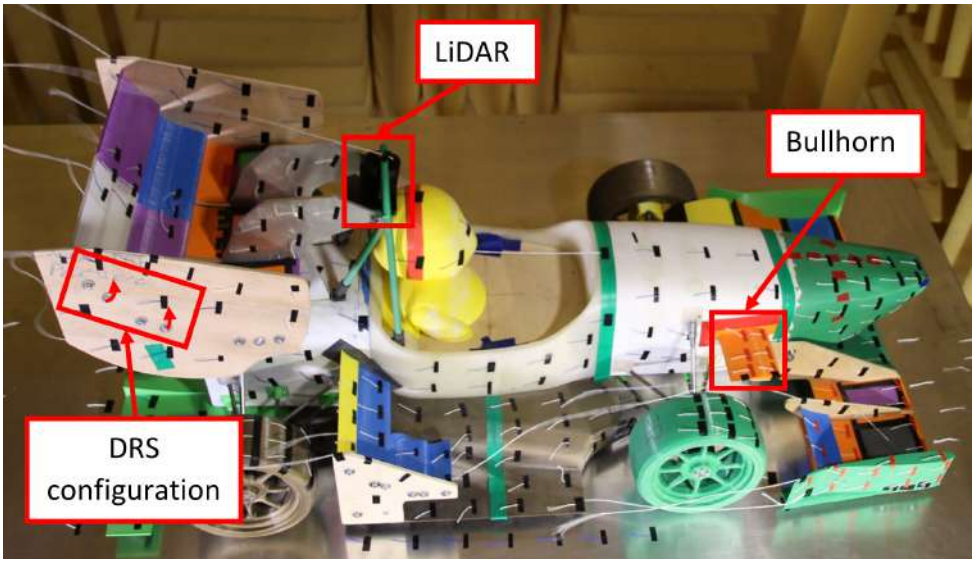

Figure 5.1: Configuration variation setups.

The $RH1$ configuration was obtained by attaching the model to the balance arm support without any ground clearance adjustment plates. Configurations $RH2$ and $RH3$ were accomplished by adding, respectively, 4 and 8 ground clearance adjustment plates to each attachment point. The $RH1$ configuration presents a pitch angle of $1.23°$. However, as the center of gravity of the model is in front of the attachment points, every time the ground clearance adjustment plates were added to change configuration, the model pitch angle increased by $0.26°$.

5.2 Experimental Procedure

The experimental tests require a vast number of systems (e.g. wind tunnel motor, force balance acquisition system, temperature sensor) to work in synchrony without any link between them. To ensure that the experiments were performed in similar conditions and to minimize the experimental errors, a detailed procedure was developed, as described in Fig. 5.2

It was planned to open a hole underneath each tyre of the model although it was decided not to do so to prevent any damage to the ground aluminium plate. Doing so, would prevent the transfer of loads between the wheels and the ground. As a consequence, the assemblies of the wheels were constantly monitored to ensure that they would not touch the ground at any moment.

First, it was ensured that the model was well secured and none of its tyres touched the ground. The "fictitious" vertical symmetry plane of the wind tunnel, which should pass through the middle car, was marked by a *Light Amplification by Stimulated Emission of Radiation* (*LASER*) to facilitate the model alignment with the airflow. Afterwards, the model was subjected to the $25\,\mathrm{m\,s^{-1}}$ airflow test run, which

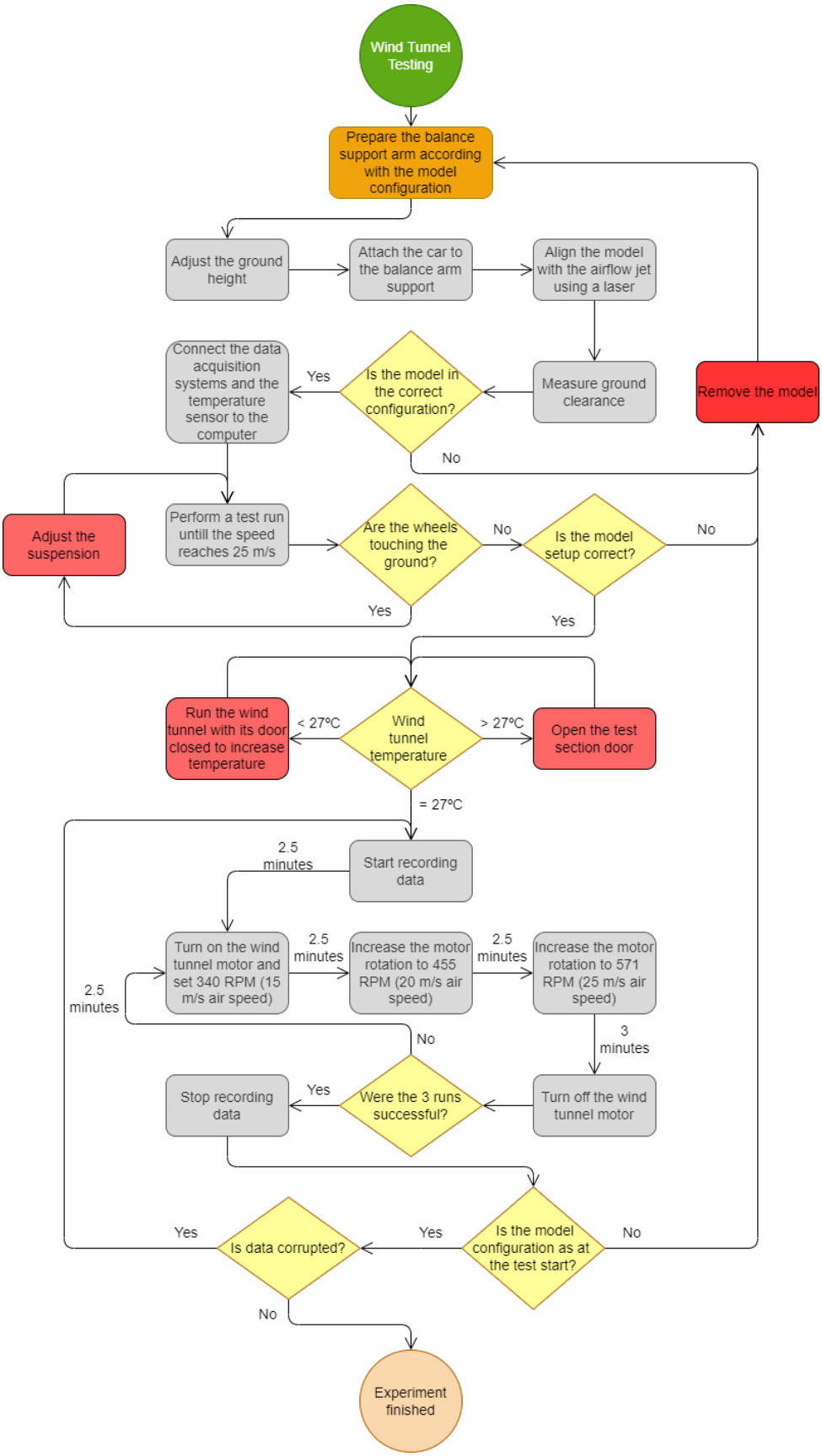

Figure 5.2: Wind tunnel testing procedure.

corresponds to the maximum speed, to ensure that the model conditions remained unchanged and also to preload the aerodynamic balance. As a result, the extensometers slack was removed and the balance looseness (observed during its calibration which was addressed in Sec. 2.6.2) was decreased as well. The test run was also useful to check the ground clearance at any speed, ensuring that no errors would affect the experimental runs. Moreover, several cameras recorded the wheels movement during the runs (Sec. 2.8).

During the tests, the wind tunnel temperature was monitored and kept at 27 ℃, which was the same temperature of the wind tunnel characterization experiments (Sec. 2.9.2). For safety reasons, the wind tunnel motor speed was increased in three steps: 340 RPM ($15\,\mathrm{m\,s^{-1}}$), 455 RPM ($20\,\mathrm{m\,s^{-1}}$) and lastly 571 RPM ($25\,\mathrm{m\,s^{-1}}$). This procedure also enabled to study how the Reynolds number affects the aerodynamic loads.

During the experiments, the balance loads, wind tunnel temperature and ground clearance were continuously monitored and recorded. The experiment was repeated whenever the model suffered any damaged or the recorded data was corrupted.

Finally, after the experiments, the model was detached from the aerodynamic balance to decrease hysteresis effects (refer to Sec. 5.4 for further information).

5.3 Flow Visualization

The aerodynamic loads collected by the aerodynamic balance enable the correlation of the wind tunnel data with CFD results. However, since the forces and moments are measured only at a single point, it is impossible to determine the behaviour of each component. Flow visualization can somewhat fill that gap. Wool tufts were bounded to the model to visualize the airflow on its surface, as seen in Fig. 5.3.

The wind tunnel airflow and the aerodynamic balance are very sensitive to motion. To obtain high quality visual data, two *GoPro*® (*Hero3* and *Hero7*) and one *Rollei*^{TM} *Actioncam 625* cameras were installed to record different perspectives, and a digital camera (*Canon*® *EOS 100D*) was used to obtain close up images of the areas of interest.

This study was done only with the $RH1$ and $RH3 - DRS$ configuration, at $25\,\mathrm{m\,s^{-1}}$. This recording session was performed separately from the experiments described in Sec. 5.4 to not disrupt the aerodynamic loads data.

The following subsections present a comparison between the experimental flow dynamics (EFD) visualization and the surface streamlines simulated numerically. The x axis skin friction on the model surface is presented in two distinct colors: red ($C_{f_x} > 0$) represents the attached airflow and blue ($C_{f_x} < 0$) the separated airflow zones.

Finally, it is important to note that phenomena that are smaller than the wool length, like small recirculation zones, might not be captured. Tufts can filter those high frequency perturbations. Moreover, turbulence is a severe unsteady phenomenon, experimental images represent just a moment in time. Thus, some conclusions drawn from the recordings were impossible to represent in figures. In contrast,

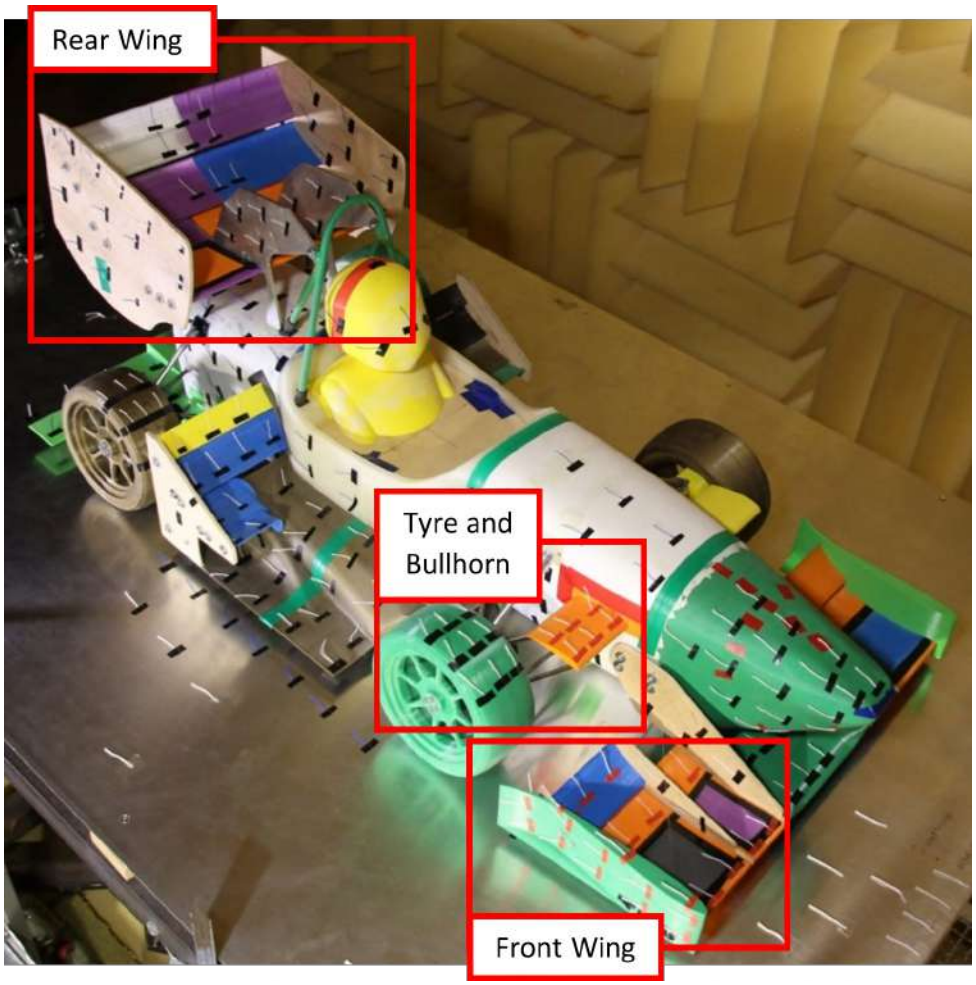

(a) Frontal view.

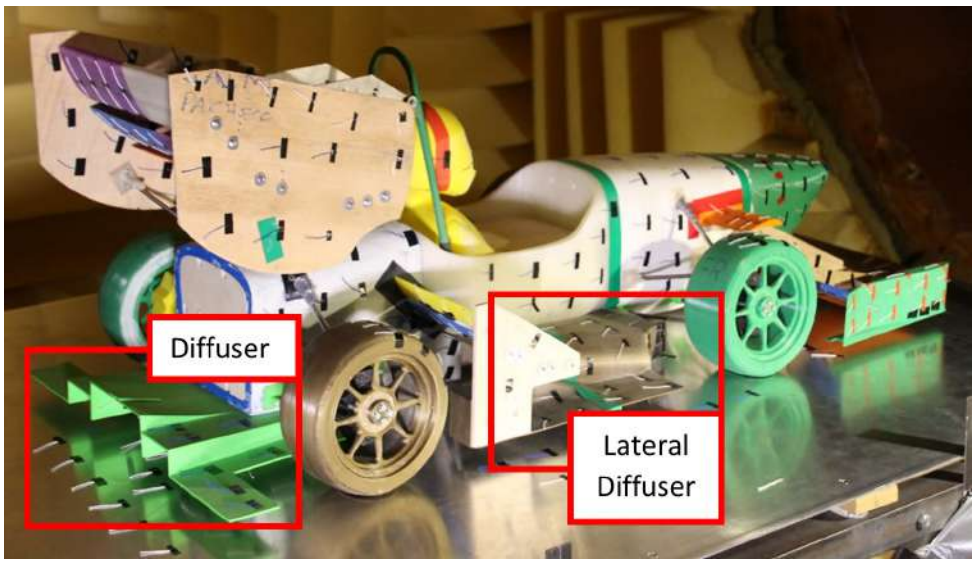

(b) Rear view.

Figure 5.3: Wool tufts for flow visualization.

the numerical simulation presents a time average result. In addition, the airflow presents not only longitudinal but also 3D and mix transverse separations, which are very difficult to trace with tufts. The following images highlight the assemblies used to draw the most relevant conclusions from the experi-

mental recordings, such as the model rear wing, tyre and bullhorn and front wing observed in Fig. 5.3.(a) and the diffuser and lateral diffuser depicted in Fig. 5.3.(b).

5.3.1 Front Wing

The front wing presented some major discrepancies between the experimental (Fig. 5.4.(a)) and numerical (Fig. 5.4.(b)) results.

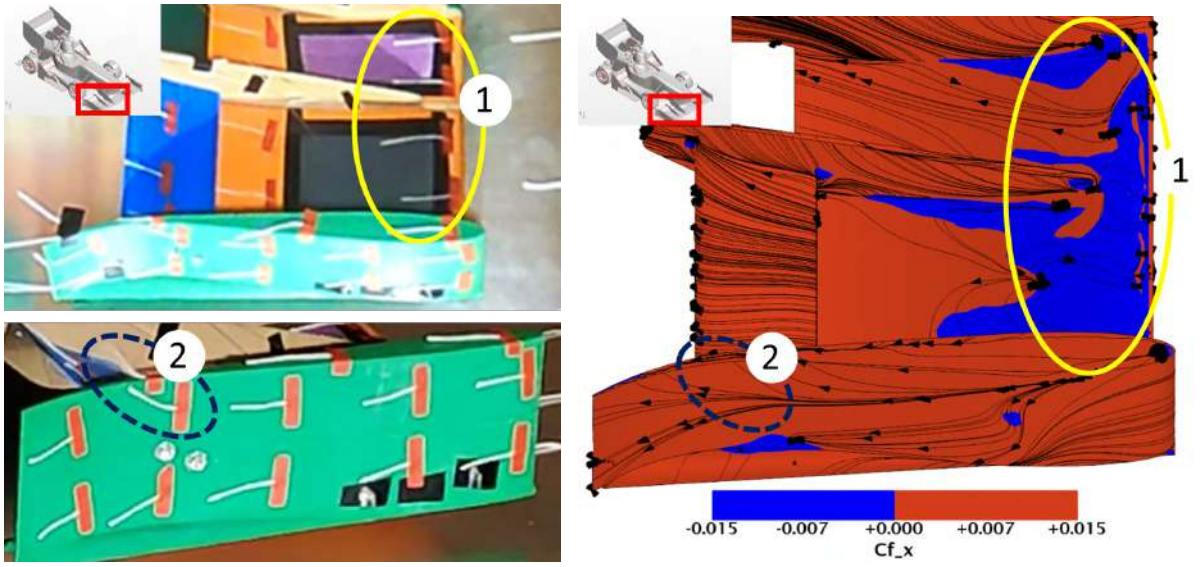

(a) EFD. (b) CFD.

Figure 5.4: Front wing pressure side flow visualization ($RH1$).

During the experiments, the tufts only captured some vorticity near the trailing edge of the endplate (marked as zone 2 in Fig. 5.4.(a)). In contradiction, the numerical simulations captured a large separation zone near the leading edge of the main plane (zone 1 in Fig. 5.4.(b)).

As such, distinct incoming airflows may be responsible for the difference noted. The tufts that were located on the ground surface, in front of the front wing, showed some movement, which means that the ground boundary layer became turbulent even before it reached the front wing. Thus, it can prevent any separation from happening. Also, the numerical domain was not a complete recreation of the experimental apparatus. Under the ground plate, there were several apparatus such us, structures to support the ground in place, the aerodynamic balance and its covers to prevent the airflow to cause undesirable loads, particularly drag. The presence of these components would affect the incoming airflow, changing it. Thus, it is reasonable to assume that the difference marked as number one was caused by both points presented.

The same geometry was simulated without using a transition model to investigate how it affects the incoming airflow. In this way, the flow is already turbulent before reaching the front wing. Figure 5.5 shows that not using a transition model leads to no separation on the front wing pressure surface. Despite being advantageous to predict transition, the γ transition model does not recreate the physics observed inside the wind tunnel.

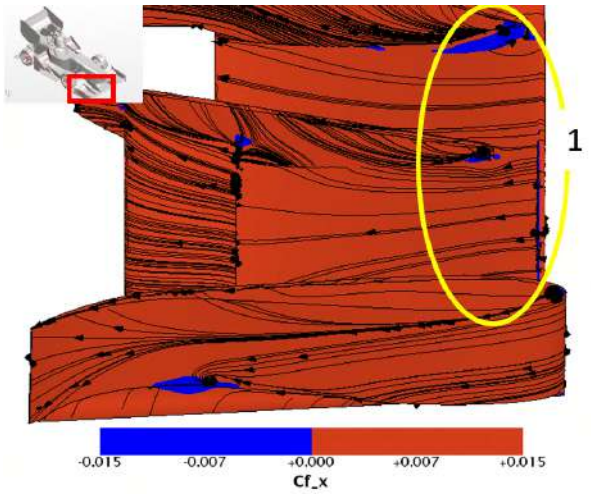

Figure 5.5: CFD front wing pressure side without transition model ($RH1$).

Regarding the endplate, generally, the surface streamlines reproduce very well the wool tufts behaviour in both simulations. Indeed, an up-wash stream was noticed (zone 2) corresponding to the up-wash created by the front wing flap.

5.3.2 Tyre and Bullhorn

During the experiment, two high turbulence zones were detected at the front of the model, one on the bullhorn (zone 1 in Fig. 5.6.(a)) and another on the tyre (zone 2 in Fig. 5.6.(a)). However, the numerical simulations predicted flow separation in both zones, as can be seen in Fig. 5.6.(b).

Focusing on the tyres surface, the behaviour of the two first rows of tufts was captured by the streamlines presented by the numerical simulation.

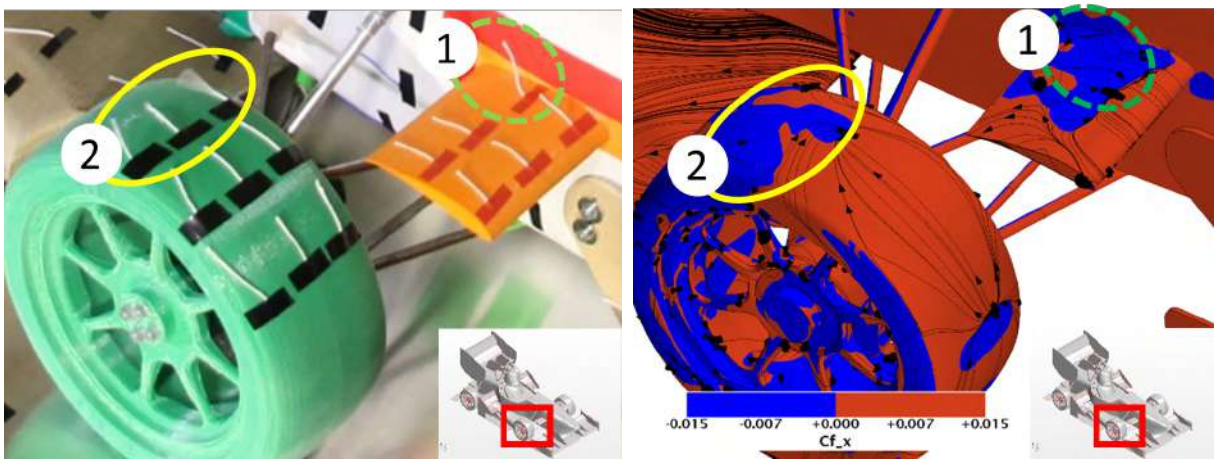

(a) EFD. (b) CFD.

Figure 5.6: Front tyre and bullhorn flow visualization ($RH1$).

The transition model failed once again to capture the wind tunnel physics. Despite presenting a smaller flow separation on the bullhorn (zone 1), removing the transition model was beneficial to recreate the tufts behaviour on the tyres surface, as zone 2 did not present any flow separation, as illustrated by

Fig. 5.7.

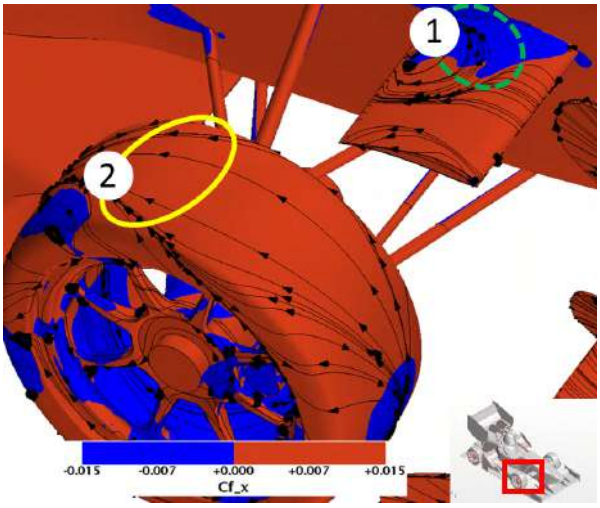

Figure 5.7: CFD front tyre and bullhorn - without transition model ($RH1$).

5.3.3 Lateral Diffuser

According to the numerical simulations, the lateral diffusers are accountable for, at least, 25% of the overall downforce. Thus, it is important to validate their performance. Despite not being able to visualize the underside of the model, some conclusions can be drawn by analysing the tufts on the upper surface, as Fig. 5.8 shows. It is important to note that the lateral diffusers are located behind the front tyres. As such, they are affected by the tyre wake turbulence, which has an unsteady behaviour. The numerical simulations are a time average result, which does not correspond to the real time behaviour of the airflow. Moreover, the tufts filter the high frequency perturbations due to their length. Thus, small separations zones can be completely unnoticed.

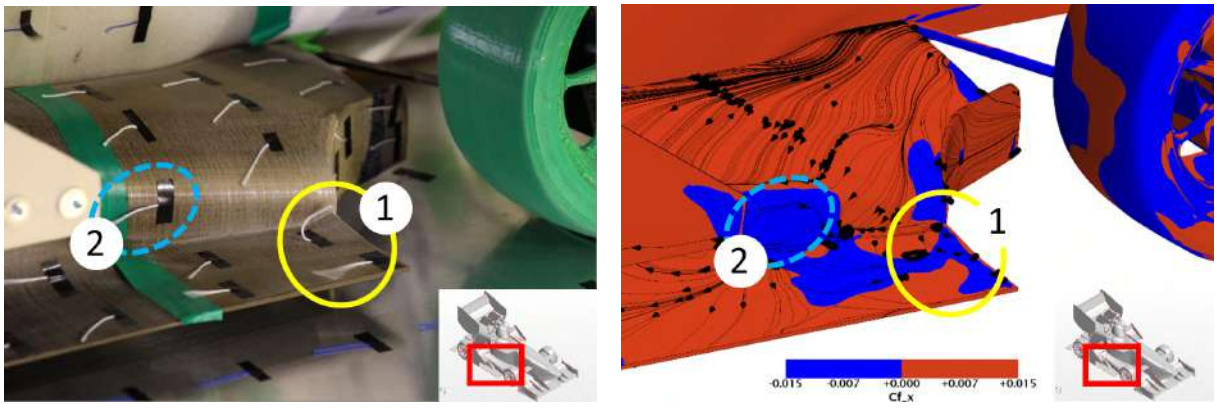

(a) EFD. (b) CFD.

Figure 5.8: Lateral diffuser flow visualization ($RH1$).

In the wind tunnel, a high turbulence zone and airflow recirculation were observed on the lateral diffuser behind the tyre (zone 1 in Fig. 5.8.(a)). The same recirculation (zone 1) was captured by the numerical simulations although the separation area (zone 2 in Fig. 5.8.(b)) was not visible in the wind

tunnel tests. Generally, the numerical surface streamlines reproduced the tufts behaviour.

5.3.4 Rear Wing

Similar to the front wing, the rear wing also presented significant differences between numerical and experimental tests, as illustrated in Fig. 5.9.

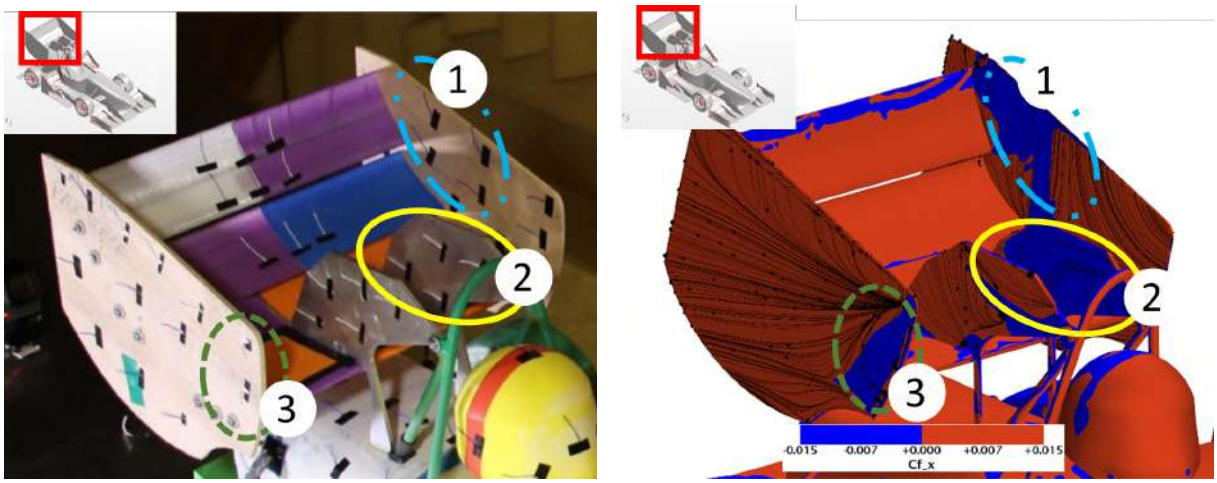

(a) EFD. (b) CFD.

Figure 5.9: Rear wing flow visualization ($RH1$).

The numerical simulations (Fig. 5.9.(b)) captured three large separation zones: endplate interior (zone 1), rear wing supports interior (zone 2) and endplate exterior (zone 3). However, only zone 3 was reproduced in the experiments. The tufts related to zone 3 show a separation zone near the endplate leading edge (zone 3 in Fig. 5.9.(a)).

The rear wing is located at the rear of the car. Thus, the airflow that reaches it has high turbulence intensity. Also, the wing geometry generates an airflow behaviour with complex combinations of longitudinal and transverse flow separation. For instance, zones 1 and 2 are extremely difficult to analyse using just tufts.

The airflow around the endplates can be complex as well as it is affected by strong vortices. In contrast, the numerical streamlines reproduced the tufts behaviour on the overall surface, as observed on the outer endplate surface.

DRS study

Regarding the $RH3 - DRS$ configuration, the rear wing flaps are set at a slight negative angle of attack to minimize drag. However, the new angle of attack caused separation on the pressure side of flaps 2 and 3, as illustrated in Fig. 5.10.(b).

Figure 5.11 shows the pressure coefficient in the rear wing middle section. It shows that the stagnation points on flaps 2 and 3 are located in the suction side. Moreover, the low pressure (suction) peak is located on the pressure surface just after the leading edge. Thus, the flow separation is caused by the excessive negative angle of attack.

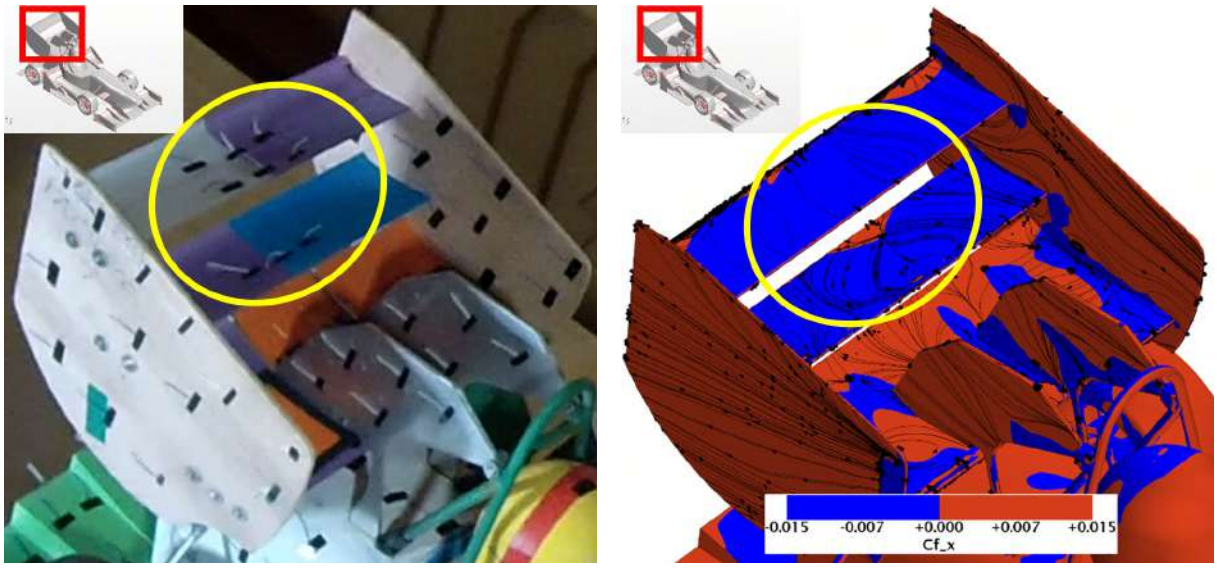

(a) EFD. (b) CFD.

Figure 5.10: Rear wing flow visualization ($RH3 - DRS$).

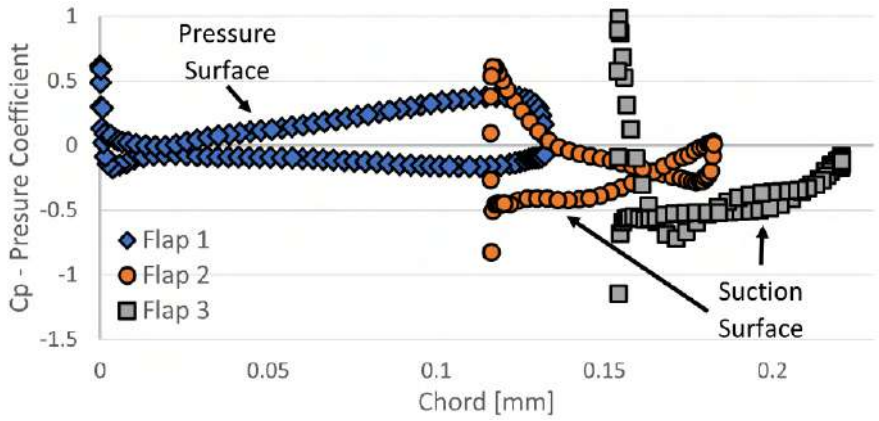

Figure 5.11: Rear wing pressure coefficient in the middle section.

The tufts located on the flaps pressure side highlighted a high turbulence zone, marked in Fig. 5.10.(a). The CFD streamlines closely match the flap 2 tufts, yet again, it is hard to identify what is exactly happening on the flaps pressure surfaces using just the tufts visualization method.

Due to the new rear wing configuration, the pressure difference between the inner and outer parts of the endplate is lower than in the last study (Sec. 5.3.4). Thus, the endplate top vortex has less circulation. The difference in the tufts behaviour highlights that change as well and once again the simulation streamlines match that behaviour.

LiDAR Study

The addition of the LiDAR at the main hoop above the pilot head caused an increase of turbulence intensity, which affected the surfaces located behind it, as proved by the tufts behaviour in zones 1 and 2 (Fig. 5.9.(a)). CFD simulations also captured several changes in those areas, predicting longitudinal separations and transverse flow.

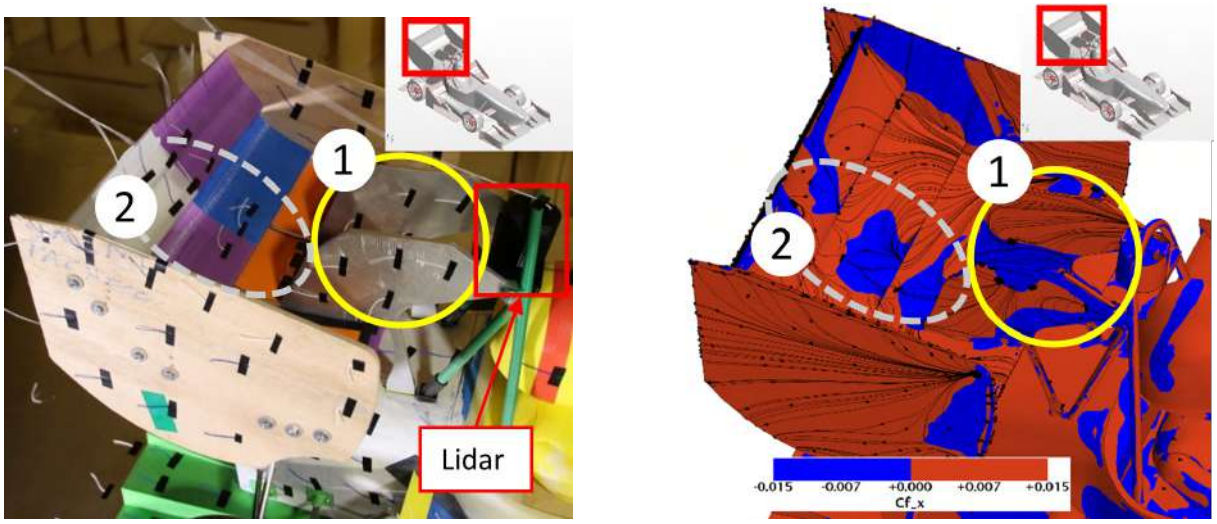

(a) EFD. (b) CFD.

Figure 5.12: Rear wing flow visualization ($RH1 - LiDAR$).

5.3.5 Diffuser

The diffuser was the only component of the model underbody that could be visualized. Numerical simulations captured two major separations, marked as zone 1 and zone 2 in Fig. 5.13.(b).

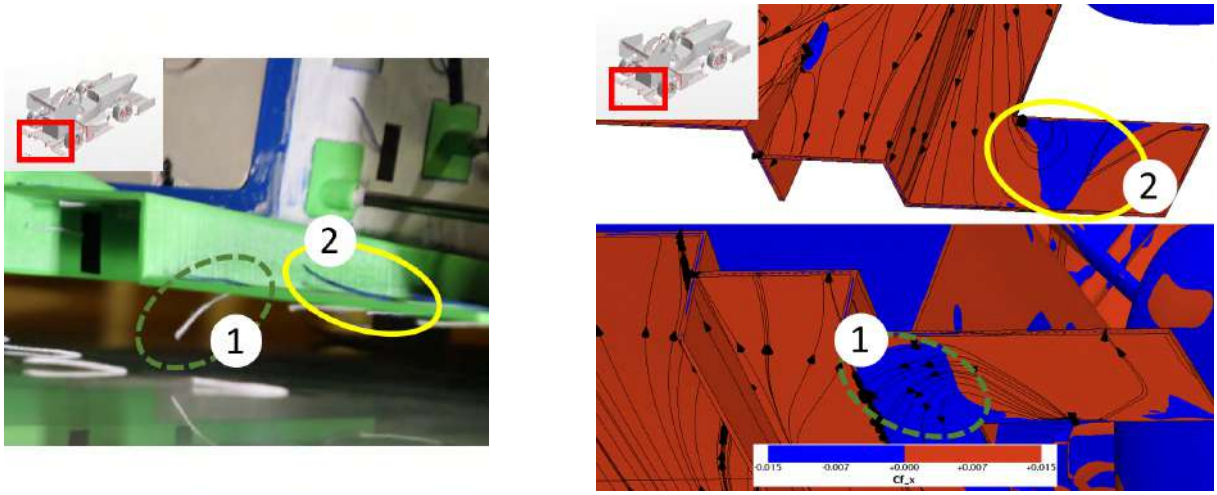

(a) EFD. (b) CFD.

Figure 5.13: Diffuser flow visualization ($RH1$).

During the test, a camera was attached to the ground to visualize the tufts inside the diffuser. This camera was located far away from the model so it did not interfere with the airflow. The tufts remained attached to the diffuser interior surfaces although it was possible to detect two high turbulence regions on the diffuser flat plates located behind the tyre. These plates aim to prevent the tyre wake to enter the diffuser due to its low pressure. Thus, these surfaces are susceptible to be in severe turbulence. The tufts highlighted in Fig. 5.13.(a) were located inside the separation zones predicted by the numerical simulations. However, it is impossible to conclude exactly what is happening to the airflow due to the tufts 3D motion.

5.4 Experimental Tests

When the model was attached to the balance, a high positive pitching moment was noticed. Since the center of gravity was located in front of the attachment point, it caused a pitch rotation and, consequently, interference between the model front suspension assembly and the ground. Moreover, the pitch rotation was also amplified by the balance looseness detected before. To shift the center of gravity backwards, two $1\,\mathrm{kg}$ steel blocks were placed inside the most rearward part of the monocoque.

Since experimental runs and their preparation were quite time consuming, it was impossible to make all the tests in a row. Furthermore, for safety reasons, two people had always to be present whenever the wind tunnel motor was in operation. To gain time, the model was prepared and attached to the aerodynamic balance, on the day before the experiment took place.

The balance calibration was made with the loads obtained from the numerical simulation, as mentioned in Sec. 2.6. It was noticed that the zero-offset forces changed considerably whenever the car remained attached overnight, due to hysteresis effects. As a result, the strains obtained during the tests began to shift outside the calibration zone, even though a safety range had been considered. Therefore, the forces had to be obtained by extrapolating the calibration results, which invalidated some experimental tests already performed.

As a matter of fact, the configurations tested consecutively, like $RH1$ and $RH1-NB$ and $RH3$ and $RH3-DRS$, can still be evaluated together, since the zero-offset forces were not affected by hysteresis. Thus, only the $RH1$, $RH2$ and $RH3$ configurations tests were repeated (designated as $RH1^*$, $RH2^*$ and $RH3^*$). Figure 5.14 presents the variation of aerodynamic loads between the initial and repeated experiments.

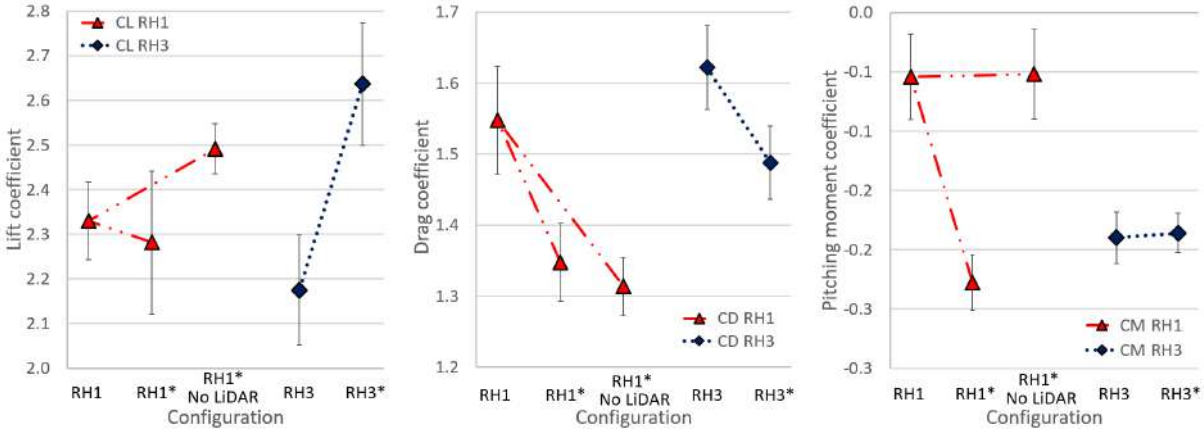

(a) Lift coefficient. (b) Drag coefficient. (c) Pitching moment coefficient.

Figure 5.14: Aerodynamic loads of the repeated experiments.

Despite the efforts, the maximum forces obtained during the repetition of the three main configurations were still outside the calibration zone, causing high uncertainties. Still, the results are qualitatively comparable and their trends remain the same, which does not invalidate the conclusions obtained by this work. Moreover, the goal of the present work is not to perform a quantitative comparison between EFD and CFD. Nonetheless, the experimental uncertainties were estimated through the standard devi-

ation of the data acquired. Several factors can affect the uncertainties of the results (balance systems, wind tunnel speed fluctuations, etc). However, its evaluation would require some sensitivity studies and non-available apparatus.

The data present in this section was collected at $25\,\mathrm{m\,s^{-1}}$ except for the *Speed Evolution Study* (Sec. 5.4.3), which evaluates the coefficients behaviour with the speed increase.

Center of Pressure - Car Handling

Improving the car handling is key to unlock its maximum performance. The relative positioning between the center of pressure (CoP) and the center of gravity (CoG), which are, respectively, the point where the aerodynamic forces and the whole mass are considered to be concentrated, dictates how the loads are distributed between the tyres. (This definition leads also to the aero balance concept, which is somehow an equivalent concept that defines the amount of the total downforce acting at the front axle.) Having the CoP in front of the CoG will load the front tyres, causing the car to oversteer. In contrast, having the CoP behind the CoG increases the grip of the rear tyres, leading the car to understeer.

As referred in Sec. 3.2.1, the lateral-directional loads F_y, M_x and M_z were neglected. Using only the longitudinal loads F_x, F_z and M_y, it is possible to determine the line of action of the resultant force,

$$\sum M_{CoP} = 0 \Rightarrow \underbrace{M_y - F_x\Delta z - F_z\Delta x = 0}_{\text{Resultant force line of action}} \Leftrightarrow \Delta x = \frac{M_y - F_x\Delta z}{F_z}. \tag{5.1}$$

Since the goal is to locate the CoP relative to the model CoG, the same height was assumed for both. Figure 5.15 represents a possible relationship between the model CoG and CoP. The x distance between the CoG and CoP is marked as b in this figure. When $b > 0$, the CoP is located behind the CoG, as pictured. However, if $b < 0$, the CoP is located in front of the CoG.

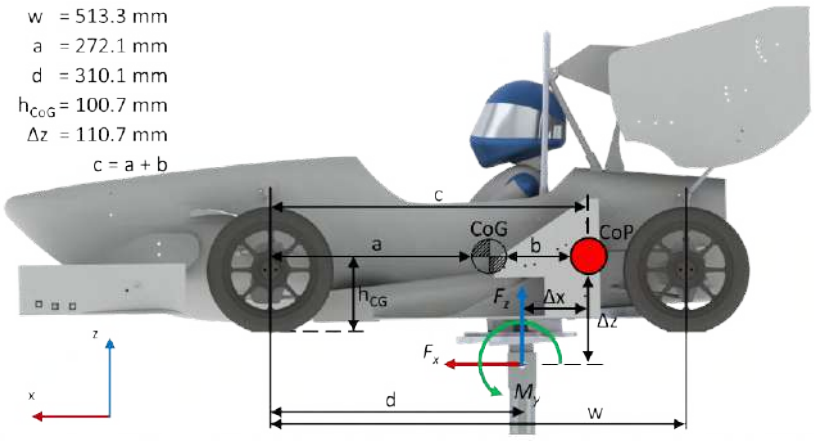

Figure 5.15: Representation of a possible relation between the center of gravity (CoG) and center of pressure (CoP) when b > 0.

Previous tests done by the FST team with an RH1 equivalent car configuration concluded that the FST10e prototype center of mass is located at 53% of the car wheelbase (marked as w in Fig. 5.15). In other words, 47% of the car weight is distributed in the front tyres, at a height of $302\,\mathrm{mm}$, which changes

to $h_{CoG} = 100.67\,\text{mm}$ when the scale factor (1/3) is applied. As the ride height changes, the CoG height changes as well. However, it was considered to be fixed for the calculations since it does not affect the outcome.

Once again, the observations regarding the CoP will be done qualitatively due to the high uncertainty related to its calculation. Thus, the focus will remain in the CoP shifts. However, it is important to remark that the wind tunnel tests suggested that the FST10e presented an aero balance between 10% and 20%, which locates de CoP behind the CoG.

5.4.1 Bullhorn Study

The first configuration was tested with ($RH1$) and without bullhorns ($RH1-NB$). Despite generating lift, the bullhorns are supposed to improve the airflow around the car by reducing the upwash generated by the front wing and redirecting the airflow to the side and rear wings, shifting the CoP rearwards. At the same time, they create a vortex to control the tyre wake and to push away the air with low momentum located at the side of the car. Furthermore, it also counters the vortex generated by the rear wing endplate by rotating in the opposite direction. Since the bullhorns performance is directly dependent on the effectiveness of vortices, its position can be hard to establish from numerical simulations. Figure 5.16 illustrates the relation between the numerical and experimental results for the bullhorn study.

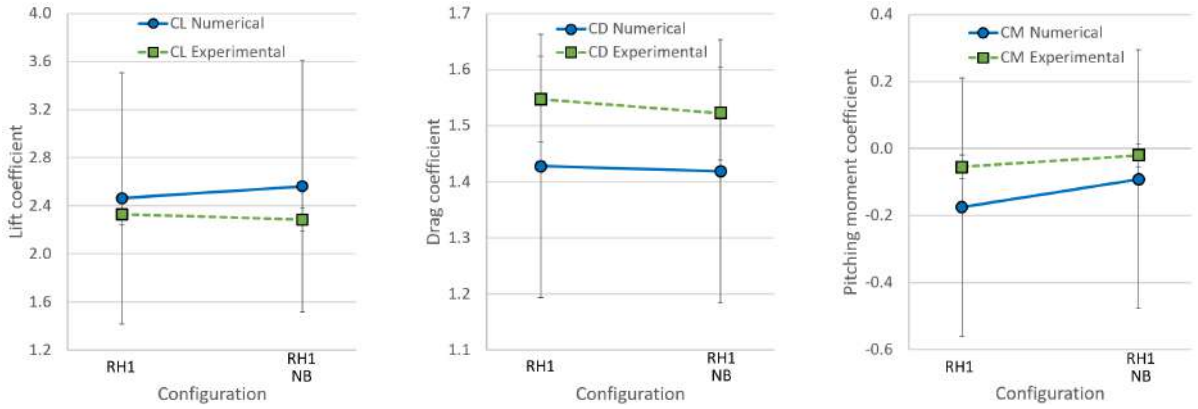

(a) Lift coefficient. (b) Drag coefficient. (c) Pitching moment coefficient.

Figure 5.16: Bullhorn study aerodynamic loads.

The drag and pitching moment coefficients (Fig. 5.16.(b) and (c)) present the same trend in the experimental tests as well as in the numerical ones, also the numerical simulations presents almost the same sensitivity as the experimental tests.

The lift and drag coefficients (Fig.5.16.(a) and (b)) present a small variation. However, the later shows a slight increase with the $RH1-NB$ configuration in the numerical simulation, which did not represent the behaviour of the wind tunnel tests.

Without bullhorns, the CoP presented higher sensitivity in the numerical simulations, where it shifted forward approximately 7.4% in contrast with the 2.8% in the experimental tests. Indeed, the bullhorns cause a rearwards shift of the CoP.

As a matter of fact, the experimental tests did not provided enough data to prove that the bullhorns

are essential to improve the aerodynamics of the car. Despite increasing the lift, it also shifts the CoP rearwards. This might not be worthy as it deteriorates the car handling if the car has already the CoP located behind the CoG, which is the FST10e case.

5.4.2 DRS Study

The third configuration ($RH3$) presented a higher pitch angle than the other two. Thus, the rear wing is exposed to cleaner airflow, producing higher aerodynamic loads. The $RH3 - DRS$ is an acceleration configuration that aims to reduce the drag force. Figure 5.17 correlates both ends of the rear wing flaps adjustments.

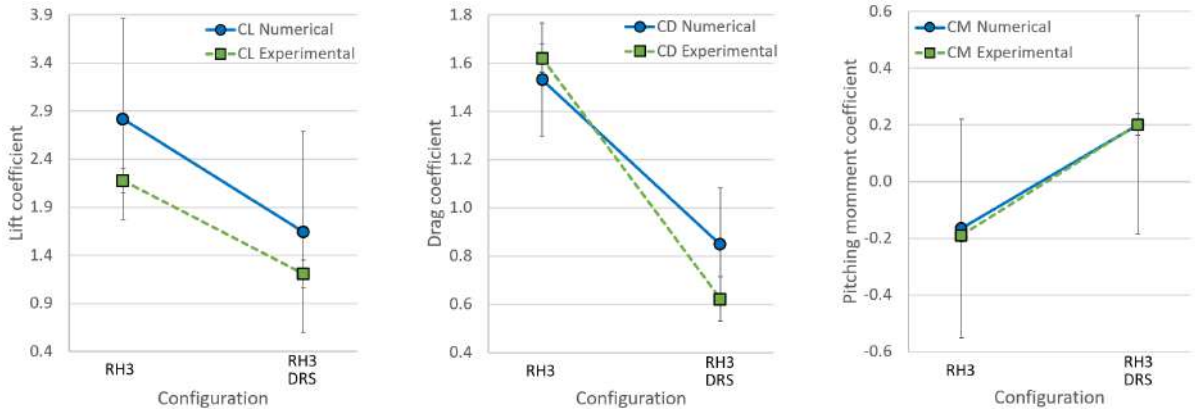

(a) Lift coefficient. (b) Drag coefficient. (c) Pitching moment coefficient.

Figure 5.17: DRS study aerodynamic loads.

The three aerodynamic loads and moments studied present the same trend in both the numerical simulations and the experimental tests. Both lift and drag coefficient (Fig. 5.17.(a) and (b)) decrease in the $RH3 - DRS$ configuration.

Notoriously, the numerical simulation do not capture the drag coefficient (Fig. 5.17.(b)) high sensitivity registered during the experimental tests.

The lift coefficient (Fig. 5.17.(a)) presents the same behaviour for both configurations. Despite the higher sensitivity discrepancy noted on the drag coefficient, the lift coefficient difference remains approximately constant between the $RH3$ and $RH3 - DRS$ configurations.

Finally, the pitching moment coefficient (Fig. 5.17.(c)) highlights a considerable shift of the CoP between the $RH3$ and $RH3 - DRS$ configurations. During the experimental tests, the CoP of the $RH3$ configuration was located behind the attachment point ($C_M < 0$) and it shifted forwards with the $RH3 - DRS$ configuration ($C_M > 0$). In this case, the numerical simulation captured the behaviour of the experiments. This remark is corroborated by the pitch rotation experienced by the model in the wind tunnel, as illustrated in Fig. 5.18. However, CFD simulations did not reproduce any rotation since they work with rigid geometries. The model motion may be the source for some discrepancies registered in the results.

The aero balance highlights, even more, the CoP shift, it presents a variation of +54.4%, which locates the CoP in front of the CoG. In contrast, the numerical values show a minor sensitivity regarding

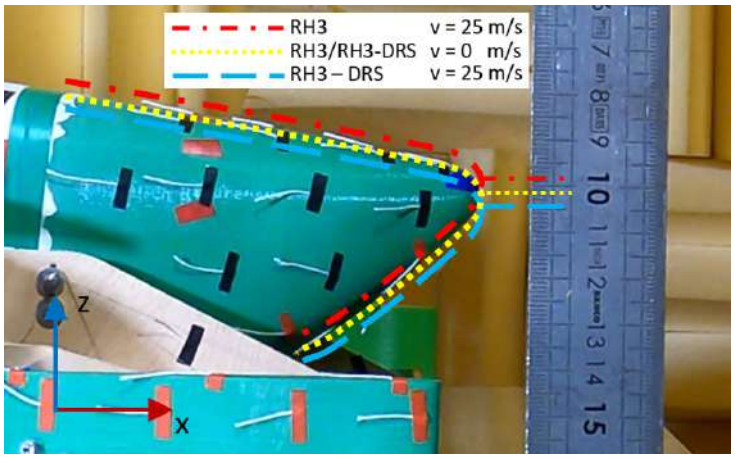

Figure 5.18: RH3-DRS configuration pitch rotation.

the aero balance, which registered only a +35% shift.

5.4.3 Speed Evolution Study

Theoretically, dimensionless coefficients, such as lift (Eq.1.1), drag (Eq.1.2) and pitching moment (Eq.1.3), are supposed to remain approximately constant independently of the experimental test speed, assuming constant air density (ρ) and the same reference area (S). However, they present small changes due to Reynolds effects. Moreover, if the flow regime remains the same, the lift coefficient usually increases with the Reynolds number [52].

Figure 5.19 presents the sensitivity of those three coefficients to the airflow speed obtained during the experimental and numerical tests. Numerically, all three coefficients present the same trend between the distinct speeds, and consequently, between different Reynolds number. Moreover, these variations are quite small which was theoretically expected. The experimental lift coefficient (Fig. 5.19.(a)) increases between the 15 and $20\,\mathrm{m\,s^{-1}}$ and decreases until $25\,\mathrm{m\,s^{-1}}$, which does not correspond to the trend obtained in the numerical simulations. Furthermore, the variation registered between the second and the third speed is higher than the total variation obtained in the numerical simulation. This may be explained by the appearance of separation zones when speed is increased. As mentioned before, the model is simulated as a rigid body. However, during the wind tunnel tests the model presented motion, which leads to changes in the airflow.

The drag coefficient behaviour (Fig. 5.19.(b)) is a consequence of the lift coefficient since the induced drag correlates with the lift force. In turn, the trend of the numeric pitching moment coefficient (Fig. 5.19.(c)) between distinct velocities is the opposite of the experimental one. The same goes for the aero balance, both changed around 7%. However, the experimental test presents a CoP shift to the rear contrary to the numerical simulations.

To understand the reason behind the trend change in the experimental results, wool tufts were recorded at the three different speeds. This permitted the visualization of any major change in the airflow. However, the only variation happened near the leading edge of the rear wing endplate outside surface. Despite being unusual, the separation zone appeared only at $25\,\mathrm{m\,s^{-1}}$ (zone 3 in Fig.5.9). As

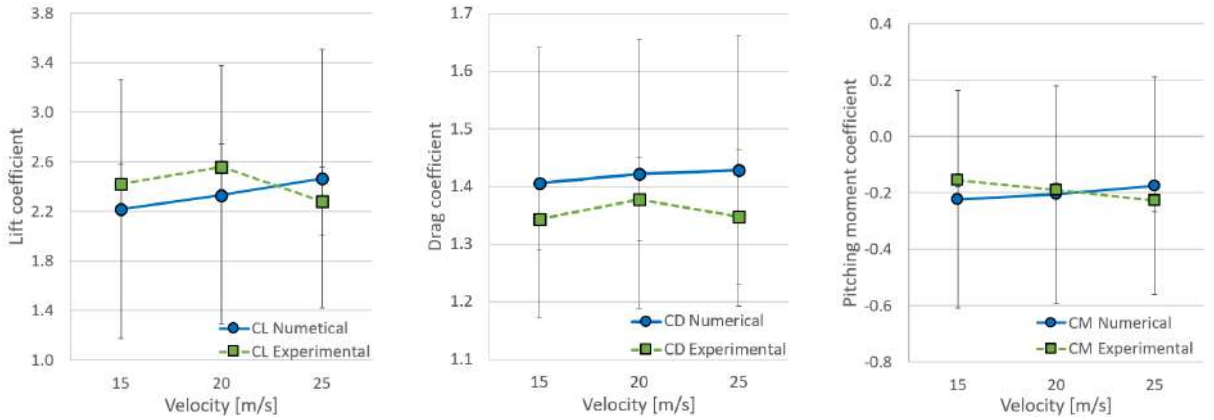

(a) Lift coefficient. (b) Drag coefficient. (c) Pitching moment coefficient.

Figure 5.19: Speed evolution study aerodynamic loads.

the Reynolds number increases with speed, the boundary layer is less likely to separate. Thus, the car rotation during the experiments is the most probable cause for its appearance. However, it did not prompt a severe change to justify the variation in the coefficients.

5.4.4 Ride Height Study

This study evaluates the sensitivity of the model aerodynamic loads to ground clearance changes. Figure 5.20 reveals how the lift, drag and pitching moment coefficients behave with the ground clearance.

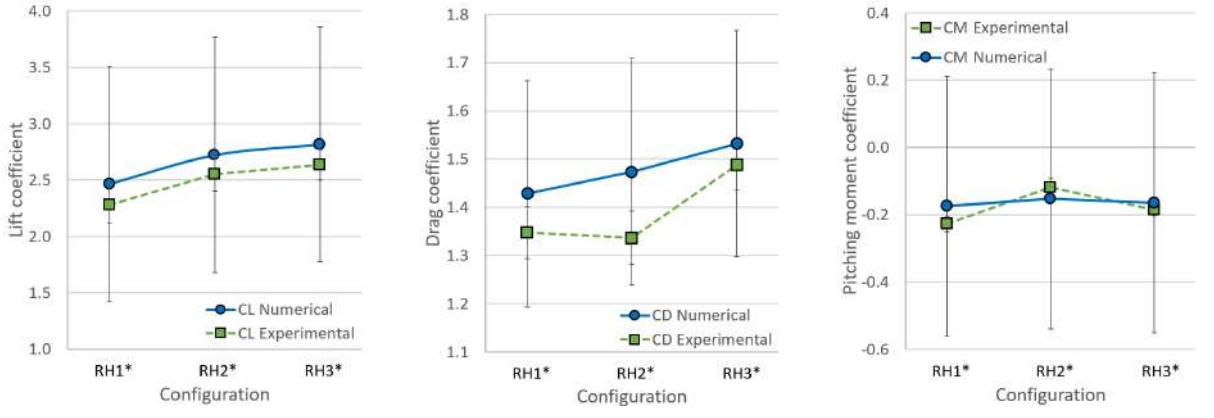

(a) Lift coefficient. (b) Drag coefficient. (c) Pitching moment coefficient.

Figure 5.20: Ride heights study aerodynamic loads.

Experimental tests concluded that the lift coefficient (Fig. 5.20.(a)) increases with the ground clearance. The lift coefficient curve related to the numerical simulations presented a constant offset for the three configurations. Also, the lift coefficient (Fig. 5.20.(a)) presents higher sensitivity to lower ride heights. In fact, in both numerical and experimental tests, it experienced a variation around 11% and 3.25%, between $RH1^*$ and $RH2^*$ configurations, and $RH2^*$ and $RH3^*$, respectively.

As expected, the drag coefficient (Fig. 5.20.(b)) from the experimental and numerical tests followed the increasing behaviour of the lift coefficient. As the model produces more downforce, it also creates more induced drag. During the experimental tests, the $RH2^*$ configuration presented a slight decrease

in drag coefficient while the pitching moment coefficient increased. In turn, the numerical simulation does not register this slight drag decrease. This was not true for the $RH1^*$ and $RH3^*$ configurations, for which the numerical results captured the same behaviour of the experimental drag coefficient.

Finally, the variations on the pitching moment coefficient (Fig. 5.20.(c)) were not captured by the numerical simulations. Generally, the experimental tests present an increase of this coefficient with the increase in ride height.

Taking a further look at the experimental results, the decrease in drag combined with an increase in downforce was not expected. The $RH2^*$ results may be affected due to the car positioning, as a result of a non-zero yaw angle. In this case, the drag force is decomposed into F_x and F_y, affecting the drag and pitching moment coefficients.

5.4.5 LiDAR Study

The introduction of the LiDAR in the free stream, in front of the rear wing, was expected to affect negatively the aerodynamics of the model. During numerical simulations, high momentum losses occurred around the rear wing. Regarding the experimental tests, an increase of the pitching moment coefficient (Fig. 5.21.(c)) from its reference test was observed, resulting in a CoP shift forward of 4.2%. This may be explained by a loss of downforce in the rear of the model. In contrast, the numerical simulations do not capture any significant shift in the center of pressure.

Interestingly, looking at the lift coefficient (Fig. 5.21.(a)), the numerical simulations present higher sensitivity than the experimental tests. Even so, the drag coefficient (Fig. 5.21.(b)) decreases approximately the same in both experiments, maintaining the offset.

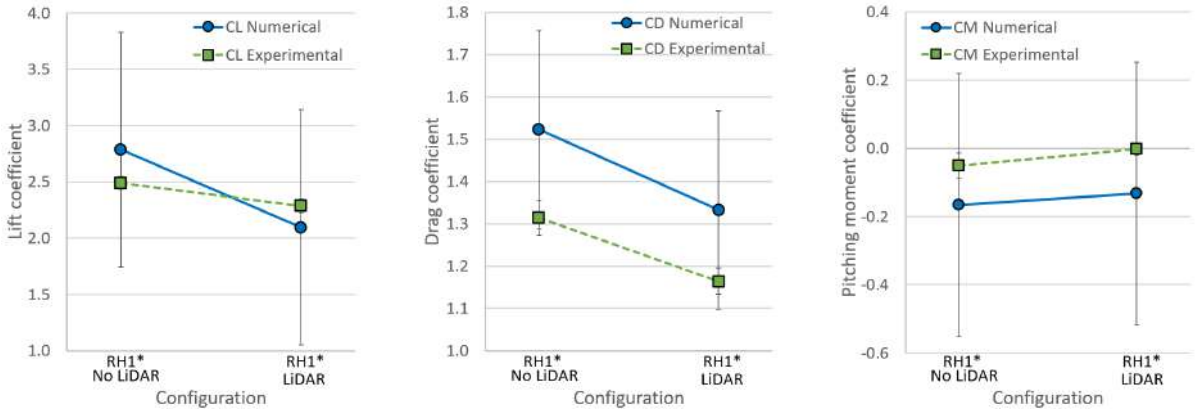

(a) Lift coefficient. (b) Drag coefficient. (c) Pitching moment coefficient.

Figure 5.21: LiDAR study aerodynamic loads.

Chapter 6

Conclusions

6.1 Achievements

The main goal of this work was to manufacture and aerodynamically test a complete Formula Student vehicle in a wind tunnel to validate the computational fluid dynamics setup and simulations. To achieve it, several improvements were made to the Aeroacoustic wind tunnel in Aerospace Laboratory at IST that enabled a representative test of the FST10e model.

The hot film anemometry enabled the characterization of the wind tunnel airflow. Generally, experimental tests revealed a higher turbulence intensity in the entire test section than the numerical simulations. Inside the jet core, the turbulence intensity was approximately 2%. Overall, the numerical simulations presented the same trends as the wind tunnel airflow. However, the major difference was registered on the shear layers, where the free stream affects the jet speed.

The numerical setup was developed to reproduce the model configurations tested in the wind tunnel. Modelling the entire wind tunnel nozzle as well as its test section revealed essential to define the initial requirements and constraints for the model itself and its positioning within the test section. The mesh convergence study presented a relatively low numerical error, 5.8% for the lift coefficient (C_L) and 4.3% for the drag coefficient (C_D). Yet, it revealed also the high uncertainties affecting the numerical setup. Moreover, the experimental uncertainties presented are considerably lower than the numerical ones.

One of the major marks of this thesis was the manufacture of a complete formula student model. Despite some geometry simplifications, the 1/3 scale FST10e model was faithful to the real prototype. Moreover, almost all simplifications were applied to the numerical setup to be as realistic as possible.

The high uncertainties did not enable a quantitative evaluation of the aerodynamic loads. However, a qualitative evaluation revealed that, generally, the numerical simulations captured the experimental trends. For instance, in the DRS study, the numerical simulation captured the C_L and C_M experimental sensitivities, while the numerical C_D sensitivity presented just a slight difference.

The wool tufts attached to the model surfaces enabled the visualization of airflow separation and turbulence zones. However, the numerical simulations presented some discrepancies with the tufts behaviour. The car presented 3D, mix transverse and longitudinal flow separations, which were difficult

to evaluate using just tufts. Finally, the front wing tufts behaviour revealed that the flow that reached the car was already turbulent. Thus, the transition model used did not reproduce the wind tunnel flow visualization. Not using one proved to be beneficial to get a better match with the wind tunnel airflow.

Despite capturing the wind tunnel results trends and physics, the CFD simulations still need time investment and more testing to provide accurate data. They did not present an exact recreation of the wind tunnel as several components had to be suppressed. Moreover, CFD simulated a rigid body which did not match the experimental model behaviour. However, they proved to be useful in assessing how the geometry changes affect the aerodynamic performance of the car.

6.2 Future Work

Despite completing all the objectives proposed, some major issues affected the experimental tests. Some of them were related to the aerodynamic balance. On one hand, its accuracy could be improved by eliminating its looseness, which may imply the dismantling of the balance and a redesign process. On the other hand, the calibration process and the experimental tests procedure could be improved as well. Testing with an initial pre load may remove the balance looseness. Finally, a new calibration should be performed to provide a wider correlation range between the extensometers and the forces applied. Moreover, new load cases (pure forces and moments, combined forces, and combined forces and moments) should be considered to add data for the side force and the yaw and roll moments. Also, the calibration apparatus experienced significant deformations when applying greater loads. An aluminium profile with T slots would increase the apparatus rigidity and ease up the calibration process.

During the tests, the model pitch angle was not constant as it presented some motion that could not be reproduced in the numerical simulations. Since it only simulates rigid domains, it would be beneficial to perform sensitivity studies, not only on the pitch angle but also on the variables/behaviours that can not be simulated.

Another way to improve the validation capability would be to improve the wind tunnel testing facility. For instance, implementing pressure sensors to provide real time speed readings of the incoming airflow would be beneficial to threat experimental data. And coupled with the aerodynamic loads, the results would be more accurate.

The mesh convergence study revealed a high uncertainty of the numerical simulations. One of the major setbacks was the computational power available. However, some improvements can be made to lower their uncertainty. For instance, sharp edges should be eliminated from the geometry in study, and mesh studies should be performed to evaluate the boundary layer evolution and turbulence zones. In this way, the mesh refinement could be performed only on the necessary components.

The numerical uncertainty was considerably higher than the experimental uncertainty. However, the latter was calculated as the standard deviation of the data acquired, which is just a small contributor. Quantifying more accurately the experimental uncertainty would increase the confidence of the results. However, it would not only require studying how it propagates from the aerodynamic balance sensors to the data measured, but also how the external factors affect the results.

Bibliography

[1] History of formula student. Accessed: Oct 2021. url: https://www.imeche.org/events/formula-student/about-formula-student/history-of-formula-student.

[2] Fs rules 2021. Accessed: Oct 2021. url: https://www.formulastudent.de/fsg/rules/.

[3] D. G. Biswas. Historical perspectives of CFD and some applications. Department of Mechanical Engineering, Indian Institute of Technology Kanpur. Accessed: Nov 2021. url: https://www.iist.ac.in/sites/default/files/people/cfd_history.html.

[4] J. Tu, G. H. Yeoh, and C. Liu. *Computational Fluid Dynamics: A Practical Approach.* Butterworth-Heinemann, third edition, 2018. ISBN 978-0-08-101127-0.

[5] G. Hatton. Tech explained: Formula student aerodynamics. Racecar Engineering. Accessed: Oct 2021. url: https://www.racecar-engineering.com/articles/tech-explained-formula-student-aerodynamics/7/.

[6] B. Rembold. 3D flow measurement in the wind tunnel - a formula student case study. AirShaper. Accessed: Oct 2021. url: https://airshaper.com/blog/3d-flow-measurement-formula-student.

[7] T. Gilles, J. Routly, C. Sheffer, L. S. Theodore, A. Vithayathil, and A. Webster. Wind tunnel model and control system. DS6 - Design Show 6 University of Southampton. Accessed: Oct 2021. url: https://uosdesign.org/designshow2020/project/wind-tunnel-model-and-control-system/.

[8] J. B. Barlow, W. H. Rae, and A. Pope. *Low Speed Wind Tunnel Testing*. New York : Wiley, February 1999.

[9] Smoke and tufts. Accessed: Oct 2021. url: https://www.grc.nasa.gov/www/k-12/airplane/tunpart.html.

[10] B. Celis and H. H. Ubbens. Design and construction of an open-circuit wind tunnel with specific measurement equipment for cycling. *Procedia Engineering*, 147:98–103, 2016. doi: 10.1016/j.proeng.2016.06.196.

[11] Wind tunnel techniques. Accessed: Oct 2021. url: https://wttaerojjcet.blogspot.com/2014/01/, 2014.

[12] T. E. Farrell and D. L. S. Miller. Development of a new boundary layer control technique for automotive wind tunnel testing. *44th AIAA Aerospace Sciences Meeting and Exhibit*, 2006. doi: 10.2514/6.2006-356.

[13] B. Fago, H. Lindner, and O. Mahrenholtz. The effect of ground simulation on the flow around vehicles in wind tunnel testing. *Journal of Wind Engineering and Industrial Aerodynamics*, 38: 47–57, 1991.

[14] W. H. Hucho. *Aerodynamics of Road Vehicles*. Butterworth-Heinemann Ltd, 1987.

[15] Y. L. Shekhter. Hot-wire and hot-film anemometers. 2011. Accessed: Nov 2021. url: https://www.thermopedia.com/content/853/.

[16] M. Samardzic, Z. Anastasijević, D. Marinkovski, D. Ćuršić, and J. Isaković. External six-component strain gauge balance for low speed wind tunnels. 2014. Accessed: Dec 2021. url: http://www.vti.mod.gov.rs/ntp/rad2014/3-2014/6/6.pdf.

[17] J. Katz. *Race car aerodynamics : designing for speed*. Bentley Publishers, 1996. ISBN 978-0837601427.

[18] M. Gonzalez, J. M. Ezquerro, V. Lapuerta, A. Laveron, and J. Rodriguez. *Components of a Wind Tunnel Balance: Design and Calibration*, chapter 7. IntechOpen, November 2011. doi: 10.5772/21095.

[19] M. Kissai. *Optimal Coordination of Chassis Systems for Vehicle Motion Control*. PhD thesis, June 2019.

[20] A. Oliveira. Design, construction, calibration and testing of a wind tunnel force balance. Master's thesis, Instituto Superior Técnico, September 2020.

[21] Ni-9237. *National Instruments™*, . Accessed: Dec 2021. url: https://https://www.ni.com/pt-pt/support/model.ni-9237.html.

[22] M. Ferreira. Design of a six-component external wind tunnel balance. Master's thesis, Instituto Superior Técnico, July 2015.

[23] Smoke and tufts. Accessed: Nov 2021. url: https://www.grc.nasa.gov/www/k-12/airplane/tunvsmoke.html.

[24] R. Smedley. Testing explained: Rob smedley on flow-vis paint., 2019. Accessed: Oct 2021. url: https://www.formula1.com/en/latest/article.testing-explained-rob-smedley-on-flow-vis.7nU2VePGlVrhIGa8wgCoLE.html.

[25] Aeroacoustic wind tunnel. Accessed: Nov 2021. url: https://fenix.tecnico.ulisboa.pt/investigacao/cctae/tunel-aero-acustico.

[26] R. P. Bauman and R. Schwaneberg. Interpretation of bernoulli's equation. *The Physics Teacher*, 32(8):478–488, 1994. doi: 10.1119/1.2344087.

[27] *Model 1750 Constant Temperature Anemometer*. TSI Incorporated, 500 Cardigan Road, Shoreview, Minnesota 55126 USA, revision n edition, February 2008.

[28] Pcie-6321. *National Instruments™*, . Accessed: Dec 2021. url: https://www.ni.com/pt-pt/support/model.pcie-6321.html.

[29] Z. Sulaiman. Effect of open-jet shear layers on aeroacoustic wind tunnel measurements. November 2011.

[30] V. de Brederode. *Aerodinâmica Incompressível: Fundamentos*. IST Press, Av. Rovisco Pais, 1049-001 Lisboa, Portugal, first edition, September 2014.

[31] T. David. *Statistical Physics Interpretation of Southern Ocean Mesoscale Turbulence*. PhD thesis, August 2018.

[32] P. Spalart and C. Rumsey. Effective inflow conditions for turbulence models in aerodynamic calculations. *Aiaa Journal - AIAA J*, 45:2544–2553, October 2007. doi: 10.2514/1.29373.

[33] C. Baker, T. Johnson, D. Flynn, H. Hemida, A. Quinn, D. Soper, and M. Sterling. Chapter 4 - computational techniques. In C. Baker, T. Johnson, D. Flynn, H. Hemida, A. Quinn, D. Soper, and M. Sterling, editors, *Train Aerodynamics*, pages 53–71. Butterworth-Heinemann, 2019. ISBN 978-0-12-813310-1. doi: 10.1016/B978-0-12-813310-1.00004-6.

[34] O. Reynolds. On the dynamical theory of incompressible viscous fluids and the determination of the criterion. *Proceedings of the Royal Society of London. Series A: Mathematical and Physical Sciences*, 1995. doi: 10.1098/rspa.1995.0116.

[35] Simcenter *StarCCM+*® documentation. Siemens PLM Software, 2020. Version 2020.3.

[36] S. Bistafa. On the development of the navier-stokes equation by navier. *Revista Brasileira de Ensino de Física*, 40, November 2017. doi: 10.1590/1806-9126-rbef-2017-0239.

[37] F. R. Menter. Two-equation eddy-viscosity turbulence models for engineering applications. *Aiaa Journal - AIAA J*, 32:1598–1605, 1994. doi: 10.2514/3.12149.

[38] V. Peterson and C. A. Smith. Applied aerodynamics: Challenges and expectations. *AIAA 10th Applied Aerod. Conf.*, 1992.

[39] L. Eça and M. Hoekstra. The numerical friction line. *J Mar Sci Technol 13*, (13):328–345, 2008. doi: 10.1007/s00773-008-0018-1.

[40] X. Zheng, C. Liu, F. Liu, and C.-I. Yang. Turbulent transition simulation using the k – ω model. *International Journal for Numerical Methods in Engineering*, 42(5):907–926, 1998. doi: 10.1002/(SICI)1097-0207(19980715)42:5<907::AID-NME393>3.0.CO;2-T.

[41] L. Eça, R. Lopes, S. L. Toxopeus, and M. Kerkvliet. Transition from laminar to turbulent flow. Marin, 2021. Accessed: Oct 2021. url: http://user.engineering.uiowa.edu/~me_260/2021_Spring/Lecture%20note/Chapter%205/Chapter%205%20(7)/Chapter%205%20(7a).pdf.

[42] H. Mendis. Better meshing using ansys fluent meshing?, 2018. Accessed: Oct 2021. url: https://www.linkedin.com/pulse/better-meshing-using-ansys-fluent-hashan-mendis?trk=portfolio_article-card_title.

[43] M. Sosnowski1, J. Krzywanski, K. Grabowska1, and R. Gnatowska. Polyhedral meshing in numerical analysis of conjugate heat transfer. volume 180. EPJ Web Conferences, 2018. doi: 10.1051/epjconf/201818002096.

[44] M. Vallikivi, M. Hultmark, and A. J. Smits. Turbulent boundary layer statistics at very high reynolds number. *Journal of Fluid Mechanics*, 779:371–389, 2015. doi: 10.1017/jfm.2015.273.

[45] L. Eça. *Aerodinâmica Incompressível: Execícios*. IST Press, Av. Rovisco Pais, 1049-001 Lisboa, Portugal, first edition, December 2015.

[46] S.-C. Mou, Y.-X. Luan, W.-T. Ji, J.-F. Zhang, and W.-Q. Tao. An example for the effect of round-off errors on numerical heat transfer. *Numerical Heat Transfer, Part B: Fundamentals*, (1):21–32, 2017. doi: 10.1080/10407790.2017.1338096.

[47] J. Tu, G.-H. Yeoh, and C. Liu. Chapter 6 - CFD solution analysis: Essentials. In *Computational Fluid Dynamics*, pages 211–253. Butterworth-Heinemann, third edition, 2018. ISBN 978-0-08-101127-0. doi: 10.1016/B978-0-08-101127-0.00006-4.

[48] L. Eca, G. Vaz, S. L. Toxopeus, and M. Hoekstra. Numerical errors in unsteady flow simulations. *Journal of Verification, Validation and Uncertainty Quantification*, 2019. doi: 10.1115/1.4043975.

[49] L. Eça and M. Hoekstra. A procedure for the estimation of the numerical uncertainty of CFD calculations based on grid refinement studies. *Journal of Computational Physics*, 262:104–130, April 2014. doi: 10.1016/j.jcp.2014.01.006.

[50] Center of pressure. Accessed: Oct 2021. url: https://www.grc.nasa.gov/www/k-12/airplane/cp.html.

[51] *Ultimaker®*. Accessed: May 2021. url: https://ultimaker.com.

[52] J. Winslow, H. Otsuka, B. Govindarajan, and I. Chopra. Basic understanding of airfoil characteristics at low reynolds numbers (104–105). *Journal of Aircraft*, 55(3):1050–1061, 2018. doi:10.2514/1.C034415.

[53] Model 1750 constant temperature anemometer. *TSI Incorporated®*. Accessed: Aug 2021. url: https://docplayer.net/28306993-Instruction-manual-model-constant-temperature-anemometer.html.

Appendix A

Wind Tunnel Characterization

The five velocity profiles obtained during the wind tunnel characterization, one for each section, are presented here. The data was collected with the Model 1750 constant temperature anemometer. The velocity profiles are normalized with the center jet speed at that section.

A.1 Velocity Profiles

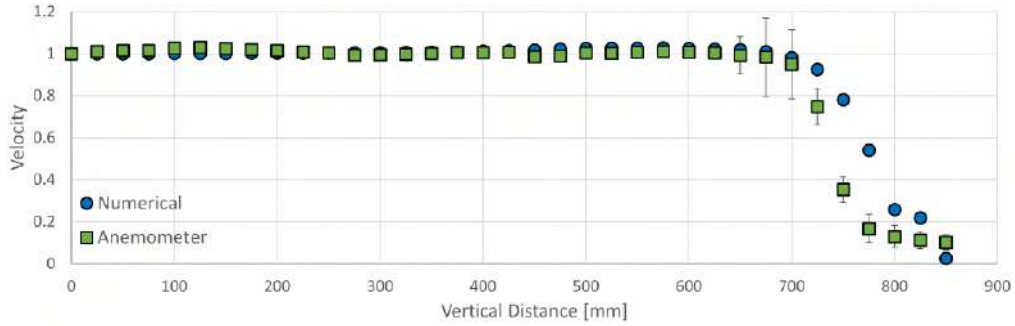

Figure A.1: Wind tunnel velocity profile at x = 315 mm from inlet.

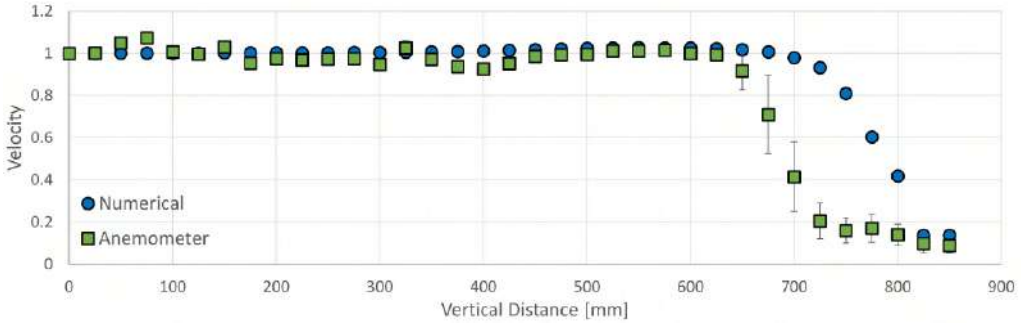

Figure A.2: Wind tunnel velocity profile at x = 415 mm from inlet.

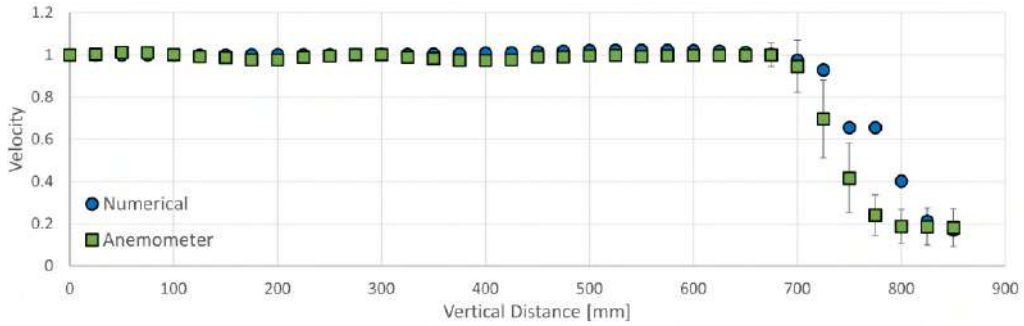

Figure A.3: Wind tunnel velocity profile at x = 515 mm from inlet.

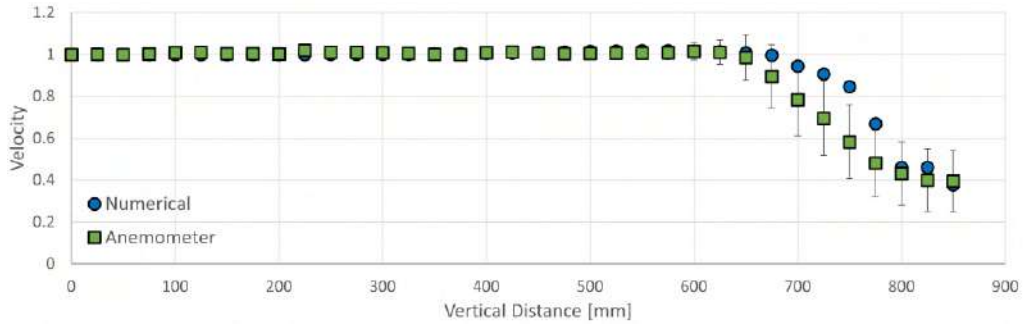

Figure A.4: Wind tunnel velocity profile at x = 1030 mm from inlet.

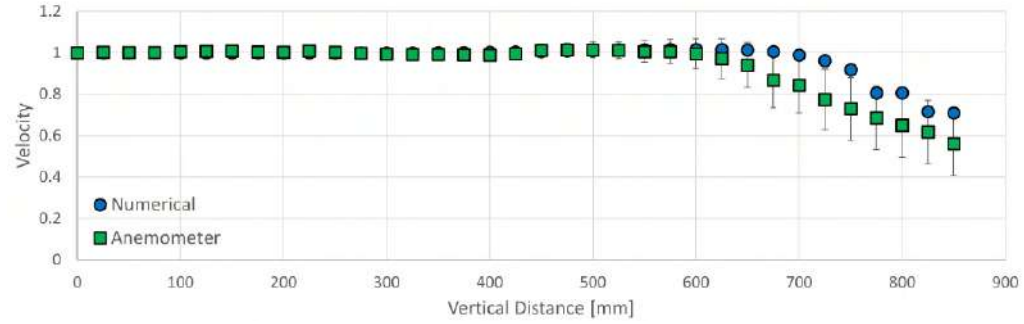

Figure A.5: Wind tunnel velocity profile at x = 2330 mm from inlet.

Appendix B

Wind Tunnel Frame Support

A steel frame structure was manufactured to support not only the aerodynamic balance used in this work but also any other apparatus that may be tested inside the wind tunnel. The steel frame structure was supported by four threaded rods built-in the concrete underneath the wind tunnel. In this way, vibrations should be reduced to a minimum.

The distance between the concrete under the wind tunnel and the base ground (where the frame support was supposed to be placed) of the wind tunnel was approximately $0.5\,\mathrm{m}$. Thus, the bending stresses could achieve high values, so a simplified and conservative mechanical analysis was performed. Since the structure would be supported by, at least, four threaded rods (Fig. B.2), the loads were divided by four. Moreover, the structure must be able to support the weight of the wind tunnel test apparatus and also the weight of two people, which usually are required to install it. Two distinct load cases were developed since it is not supposed to work inside the wind tunnel during experiments. Table B.1 represents the load cases considered in the analysis.

Table B.1: Structural load case.

Load case	$F_x\ [N]$	$F_y\ [N]$	$F_z\ [N]$	$M_x\ [Nm]$	$M_y\ [Nm]$	$M_z\ [Nm]$	Extra Weight $F_z\ [N]$	Apparatus Weight $F_z\ [N]$
Experimental Test	-415	115	-550	35	-25	-20	-	-1000
Experimental Preparation	-	-	-	-	-	-	-1700	-1000

The mechanical analysis was based on three distinct factors: the rod maximum stress (Eq. B.1), maximum deflection (Eq. B.2) and the critical buckling load (Eq. B.3). Finally, to size the diameter of the threaded rods, it was established a minimum safety factor (SF) (Eq. B.4) of 1.5.

$$\sigma = \frac{W}{A} + \frac{M_i y}{I} \quad \text{(Maximum stress)} \qquad \text{(B.1)}$$

$$\delta_{max} = \frac{W l^3}{3EI} \quad \text{(Maximum deflection)} \qquad \text{(B.2)}$$

$$P_{cr} = \frac{\pi^2 EI}{(\underbrace{K}_{=2}\, l)^2} \quad \text{(Critical buckling load)} \qquad \text{(B.3)}$$

$$SF = \frac{\overbrace{S_u}^{ultimate\ stress}}{\underbrace{\sigma}_{actual\ stress}} \quad \text{(Safety Factor)} \qquad \text{(B.4)}$$

Threaded Rod					Experimental Tests		Experimental Preparation		Buckling		Deflection [mm]
M	Pitch [mm]	Minimum Diameter [mm]	I [m^4]	A [m^2]	Stress [MPa]	Safety Factor	Stress [MPa]	Safety Factor	Fz max [N]	Safety Factor	
8	1	6.92	1.12E-10	3.76E-05	14588.64	0.03	10403.58	0.04	221.86	0.33	384.61
10	1.5	8.38	2.42E-10	5.51E-05	4773.44	0.08	5861.93	0.07	476.97	0.71	178.90
12	1.8	10.05	5.01E-10	7.93E-05	2763.22	0.14	3393.74	0.12	989.04	1.47	86.28
14	2	11.83	9.63E-10	1.10E-04	1693.32	0.24	2079.98	0.19	1900.92	2.82	44.89
16	2	13.83	1.80E-09	1.50E-04	1060.37	0.38	1302.69	0.31	3549.84	5.26	24.04
20	2.5	17.29	4.39E-09	2.35E-04	543.24	0.74	667.55	0.60	8666.59	12.84	9.85
24	3	20.75	9.10E-09	3.38E-04	314.57	1.27	386.65	1.03	17971.04	26.62	4.75
27	3	23.75	1.56E-08	4.43E-04	209.91	1.91	258.06	1.55	30841.10	45.69	2.77

Figure B.1: Mechanical analysis.

The minimum SF (above 1.5) was achieved with a M27 threaded rod (SF = 1.55 for the maximum stress). This road would have a maximum deflection of $2.8\,\mathrm{mm}$, which would be reasonable for the experimental tests. In fact, the deflection is considerably less since the frame structure is supported by all four rods (which are only around $0.2\,\mathrm{m}$ outside of the concrete instead of the $0.5\,\mathrm{m}$ initially expected) and has been considerably upgraded, as seen in Fig. B.2.(b).

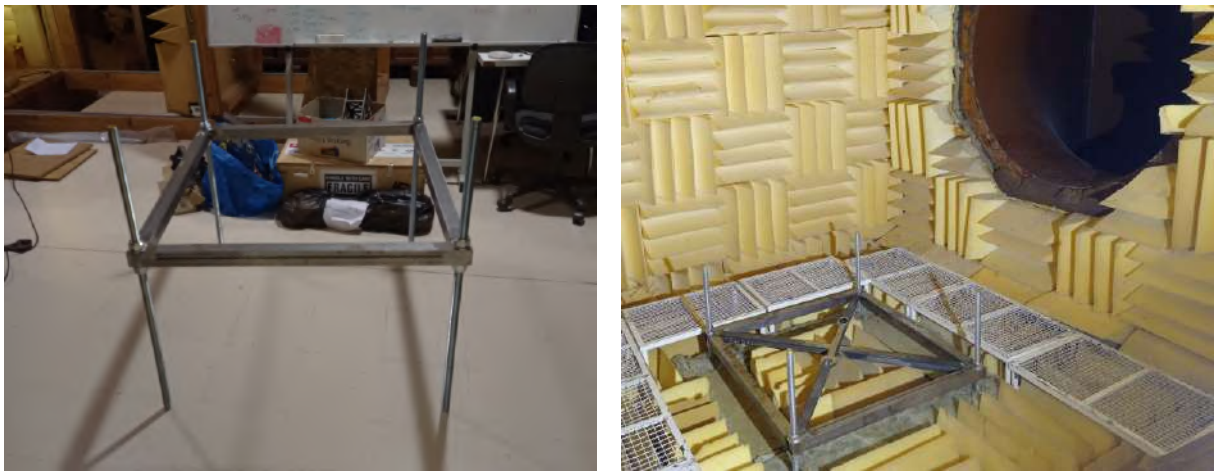

(a) Frame support. (b) Wind tunnel facility.

Figure B.2: Wind tunnel frame support.

Appendix C

Balance Calibration

C.1 Calibration Equations

The correlation between the resultant forces R = (F_x,F_y,F_z,M_x,M_y,M_z) and the force supported by each bar (r1,r2,r3,r4,r5,r6) is presented in Fig. C.1.

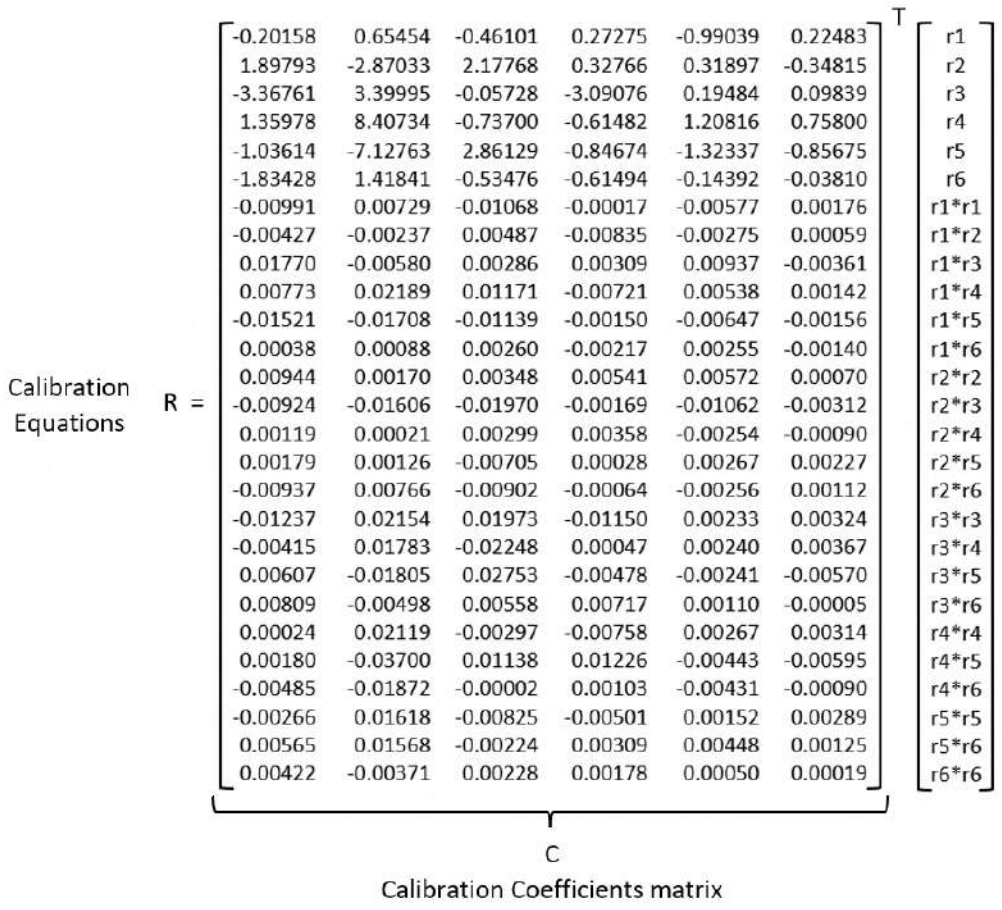

Figure C.1: Balance calibration equations.

C.2 Calibration Load Cases

Load Case	No.	Fx [N]	Fy [N]	Fz [N]	Mx [Nm]	My [Nm]	Mz [Nm]
	1	0.00	0.00	-7.56	0.00	0.00	0.00
	2	-1.01	0.00	-7.56	0.00	0.00	0.00
	3	-11.02	0.00	-7.56	0.00	0.00	0.00
	4	-21.03	0.00	-7.56	0.00	0.00	0.00
	5	-31.03	0.00	-7.56	0.00	0.00	0.00
1	6	-41.04	0.00	-7.56	0.00	0.00	0.00
Fx-	7	-51.05	0.00	-7.56	0.00	0.00	0.00
	8	-61.06	0.00	-7.56	0.00	0.00	0.00
	9	-71.06	0.00	-7.56	0.00	0.00	0.00
	10	-81.07	0.00	-7.56	0.00	0.00	0.00
	11	-91.08	0.00	-7.56	0.00	0.00	0.00
	12	-101.09	0.00	-7.56	0.00	0.00	0.00
	13	0.00	0.00	-7.56	0.00	0.00	0.00
	14	0.00	-1.02	-7.56	0.00	0.00	0.00
	15	0.00	-11.02	-7.56	0.00	0.00	0.00
	16	0.00	-16.07	-7.56	0.00	0.00	0.00
2	17	0.00	-26.07	-7.56	0.00	0.00	0.00
Fy-	18	0.00	-31.12	-7.56	0.00	0.00	0.00
	19	0.00	-41.12	-7.56	0.00	0.00	0.00
	20	0.00	-51.13	-7.56	0.00	0.00	0.00
	21	0.00	-61.14	-7.56	0.00	0.00	0.00
	22	0.00	-71.15	-7.56	0.00	0.00	0.00
	23	0.00	0.00	-7.56	0.00	0.00	0.00
	24	0.00	1.02	-7.56	0.00	0.00	0.00
	25	0.00	11.02	-7.56	0.00	0.00	0.00
	26	0.00	16.07	-7.56	0.00	0.00	0.00
3	27	0.00	26.07	-7.56	0.00	0.00	0.00
Fy+	28	0.00	31.12	-7.56	0.00	0.00	0.00
	29	0.00	41.12	-7.56	0.00	0.00	0.00
	30	0.00	51.13	-7.56	0.00	0.00	0.00
	31	0.00	61.14	-7.56	0.00	0.00	0.00
	32	0.00	71.15	-7.56	0.00	0.00	0.00
	33	0.00	0.00	-7.56	0.00	0.00	0.00
	34	0.00	0.00	-11.53	0.00	0.00	0.00
	35	0.00	0.00	-51.56	0.00	0.00	0.00
	36	0.00	0.00	-91.56	0.00	0.00	0.00
	37	0.00	0.00	-111.58	0.00	0.00	0.00
	38	0.00	0.00	-131.59	0.00	0.00	0.00
4	39	0.00	0.00	-172.12	-0.19	0.00	0.00
Fz-	40	0.00	0.00	-192.13	-0.19	0.00	0.00
	41	0.00	0.00	-212.15	-0.19	0.00	0.00
	42	0.00	0.00	-232.16	-0.19	0.00	0.00
	43	0.00	0.00	-252.18	-0.19	0.00	0.00
	44	0.00	0.00	-291.97	-0.18	0.00	0.00
	45	0.00	0.00	-331.98	-0.18	0.00	0.00
	46	0.00	0.00	-372.00	-0.18	0.00	0.00
	47	0.00	0.00	-7.56	0.00	0.00	0.00
	48	0.00	0.00	-7.56	0.24	0.00	0.00
	49	0.00	0.00	-7.56	0.48	0.00	0.00
	50	0.00	0.00	-7.56	0.72	0.00	0.00
	51	0.00	0.00	-7.56	0.96	0.00	0.00
	52	0.00	0.00	-7.56	1.20	0.00	0.00
4	53	0.00	0.00	-7.55	1.43	0.00	0.00
Mx +	54	0.00	0.00	-7.55	1.67	0.00	0.00
	55	0.00	0.00	-7.55	2.88	0.00	0.00
	56	0.00	0.00	-7.55	4.09	0.00	0.00
	57	0.00	0.00	-7.55	6.50	0.00	0.00
	58	0.00	0.00	-7.55	8.90	0.00	0.00
	59	0.00	0.00	-7.55	11.30	0.00	0.00
	60	0.00	0.00	-7.55	13.70	0.00	0.00
	61	0.00	0.00	-7.56	0.00	0.00	0.00
	62	0.00	0.00	-7.56	-0.24	0.00	0.00
	63	0.00	0.00	-7.57	-0.48	0.00	0.00
	64	0.00	0.00	-7.56	-0.72	0.00	0.00
	65	0.00	0.00	-7.57	-0.96	0.00	0.00
	66	0.00	0.00	-7.57	-1.20	0.00	0.00
5	67	0.00	0.00	-7.57	-1.43	0.00	0.00
Mx-	68	0.00	0.00	-7.58	-1.67	0.00	0.00
	69	0.00	0.00	-7.57	-2.88	0.00	0.00
	70	0.00	0.00	-7.57	-4.09	0.00	0.00
	71	0.00	0.00	-7.57	-6.50	0.00	0.00
	72	0.00	0.00	-7.57	-8.90	0.00	0.00
	73	0.00	0.00	-7.57	-11.30	0.00	0.00
	74	0.00	0.00	-7.57	-13.70	0.00	0.00

Load Case	No.	Fx [N]	Fy [N]	Fz [N]	Mx [Nm]	My [Nm]	Mz [Nm]
	75	0.00	0.00	-7.56	0.00	0.00	0.00
	76	0.00	0.00	-7.56	0.00	0.24	0.00
	77	0.00	0.00	-7.56	0.00	1.45	0.00
	78	0.00	0.00	-7.56	0.00	2.66	0.00
	79	0.00	0.00	-7.56	0.00	3.14	0.00
6	80	0.00	0.00	-7.56	0.00	3.62	0.00
My+	81	0.00	0.00	-7.56	0.00	4.09	0.00
	82	0.00	0.00	-7.56	0.00	5.29	0.00
	83	0.00	0.00	-7.56	0.00	6.49	0.00
	84	0.00	0.00	-7.56	0.00	8.90	0.00
	85	0.00	0.00	-7.56	0.00	11.30	0.00
	86	0.00	0.00	-7.56	0.00	13.70	0.00
	87	0.00	0.00	-7.56	0.00	0.00	0.00
	88	0.00	0.00	-7.56	0.00	-0.24	0.00
	89	0.00	0.00	-7.56	0.00	-1.45	0.00
	90	0.00	0.00	-7.56	0.00	-2.66	0.00
	91	0.00	0.00	-7.56	0.00	-3.14	0.00
7	92	0.00	0.00	-7.56	0.00	-3.62	0.00
My-	93	0.00	0.00	-7.56	0.00	-4.09	0.00
	94	0.00	0.00	-7.56	0.00	-5.29	0.00
	95	0.00	0.00	-7.56	0.00	-6.49	0.00
	96	0.00	0.00	-7.56	0.00	-8.90	0.00
	97	0.00	0.00	-7.56	0.00	-11.30	0.00
	98	0.00	0.00	-7.56	0.00	-13.70	0.00
	99	0.00	0.00	-7.56	0.00	0.00	0.00
	100	0.00	0.00	-7.56	0.00	0.00	0.14
	101	0.01	0.00	-7.56	0.00	0.00	0.28
	102	0.00	0.00	-7.56	0.00	0.00	0.42
	103	0.00	0.00	-7.56	0.00	0.00	0.56
	104	0.01	0.00	-7.56	0.00	0.00	0.70
8	105	0.01	0.00	-7.56	0.00	0.00	0.84
Mz+	106	0.02	0.00	-7.56	0.00	0.00	0.98
	107	0.01	0.00	-7.56	0.00	0.00	1.68
	108	0.01	0.00	-7.56	0.00	0.00	2.39
	109	0.01	0.00	-7.56	0.00	0.00	3.79
	110	0.01	0.00	-7.56	0.00	0.00	5.19
	111	0.01	0.00	-7.56	0.00	0.00	6.59
	112	0.01	0.00	-7.56	0.00	0.00	7.99
	113	0.00	0.00	-7.56	0.00	0.00	0.00
	114	0.00	0.00	-7.56	0.00	0.00	-0.14
	115	0.01	0.00	-7.56	0.00	0.00	-0.28
	116	0.00	0.00	-7.56	0.00	0.00	-0.42
	117	0.00	0.00	-7.56	0.00	0.00	-0.56
	118	0.01	0.00	-7.56	0.00	0.00	-0.70
9	119	0.01	0.00	-7.56	0.00	0.00	-0.84
Mz-	120	0.02	0.00	-7.56	0.00	0.00	-0.98
	121	0.01	0.00	-7.56	0.00	0.00	-1.68
	122	0.01	0.00	-7.56	0.00	0.00	-2.39
	123	0.01	0.00	-7.56	0.00	0.00	-3.79
	124	0.01	0.00	-7.56	0.00	0.00	-5.19
	125	0.01	0.00	-7.56	0.00	0.00	-6.59
	126	0.01	0.00	-7.56	0.00	0.00	-7.99
	127	0.00	0.00	-7.56	0.00	0.00	0.00
	128	-5.00	0.00	-11.53	0.00	0.00	0.00
	129	-15.05	0.00	-51.56	0.00	0.00	0.00
	130	-25.39	0.00	-91.56	0.00	0.00	0.00
10	131	-35.40	0.00	-111.58	0.00	0.00	0.00
Fx-	132	-45.40	0.00	-151.59	0.00	0.00	0.00
Fz -	133	-55.30	0.00	-191.61	0.00	0.00	0.00
	134	-65.31	0.00	-231.62	0.00	0.00	0.00
	135	-75.31	0.00	-251.64	0.00	0.00	0.00
	136	-85.32	0.00	-271.65	0.00	0.00	0.00
	137	-95.33	0.00	-291.67	0.00	0.00	0.00

Figure C.2: Balance calibration load cases.

Load Case	No.	Fx [N]	Fy [N]	Fz [N]	Mx [Nm]	My [Nm]	Mz [Nm]
11 Fx- Mz+	138	0.00	0.00	-7.56	0.00	0.00	0.00
	139	-1.02	0.00	-7.56	0.00	0.00	0.07
	140	-11.02	0.00	-7.56	0.00	0.00	0.77
	141	-21.03	0.00	-7.56	0.00	0.00	1.47
	142	-31.04	0.00	-7.56	0.00	0.00	2.17
	143	-41.04	0.00	-7.56	0.00	0.00	2.87
	144	-51.05	0.00	-7.56	0.00	0.00	3.57
	145	-61.06	0.00	-7.56	0.00	0.00	4.27
	146	-71.07	0.00	-7.56	0.00	0.00	4.97
	147	-81.07	0.00	-7.56	0.00	0.00	5.68
	148	-91.08	0.00	-7.56	0.00	0.00	6.38
	149	-101.09	0.00	-7.56	0.00	0.00	7.08
12 Fx- Mz-	150	0.00	0.00	-7.56	0.00	0.00	0.00
	151	-1.02	0.00	-7.56	0.00	0.00	-0.07
	152	-11.02	0.00	-7.56	0.00	0.00	-0.77
	153	-21.03	0.00	-7.56	0.00	0.00	-1.47
	154	-31.04	0.00	-7.56	0.00	0.00	-2.17
	155	-41.04	0.00	-7.56	0.00	0.00	-2.87
	156	-51.05	0.00	-7.56	0.00	0.00	-3.57
	157	-61.06	0.00	-7.56	0.00	0.00	-4.27
	158	-71.07	0.00	-7.56	0.00	0.00	-4.97
	159	-81.07	0.00	-7.56	0.00	0.00	-5.68
	160	-91.08	0.00	-7.56	0.00	0.00	-6.38
	161	-101.09	0.00	-7.56	0.00	0.00	-7.08
13 Fz- Mx+	162	0.00	0.00	-7.56	0.00	0.00	0.00
	163	0.00	0.00	-10.56	0.19	0.00	0.00
	164	0.00	0.00	-90.88	0.30	0.00	0.00
	165	0.00	0.00	-170.91	0.31	0.00	0.00
	166	0.00	0.00	-191.92	0.42	0.00	0.00
	167	0.00	0.00	-212.92	0.54	0.00	0.00
	168	0.00	0.00	-233.93	0.66	0.00	0.00
	169	0.00	0.00	-234.92	0.85	0.00	0.00
	170	0.00	0.00	-235.92	1.04	0.00	0.00
	171	0.00	0.00	-236.91	1.24	0.00	0.00
	172	0.00	0.00	-241.95	2.20	0.00	0.00
	173	0.00	0.00	-247.00	3.17	0.00	0.00
	174	0.00	0.00	-252.00	4.13	0.00	0.00
	175	0.00	0.00	-257.00	5.09	0.00	0.00
	176	0.00	0.00	-262.01	6.05	0.00	0.00
	177	0.00	0.00	-272.01	7.97	0.00	0.00
	178	0.00	0.00	-282.02	9.90	0.00	0.00
14 Fz- Mx-	179	0.00	0.00	-7.56	0.00	0.00	0.00
	180	0.00	0.00	-10.56	-0.19	0.00	0.00
	181	0.00	0.00	-90.88	-0.30	0.00	0.00
	182	0.00	0.00	-170.91	-0.31	0.00	0.00
	183	0.00	0.00	-191.92	-0.42	0.00	0.00
	184	0.00	0.00	-212.92	-0.54	0.00	0.00
	185	0.00	0.00	-233.93	-0.66	0.00	0.00
	186	0.00	0.00	-234.92	-0.85	0.00	0.00
	187	0.00	0.00	-235.92	-1.04	0.00	0.00
	188	0.00	0.00	-236.91	-1.24	0.00	0.00
	189	0.00	0.00	-241.95	-2.20	0.00	0.00
	190	0.00	0.00	-247.00	-3.17	0.00	0.00
	191	0.00	0.00	-252.00	-4.13	0.00	0.00
	192	0.00	0.00	-257.00	-5.09	0.00	0.00
	193	0.00	0.00	-262.01	-6.05	0.00	0.00
	194	0.00	0.00	-272.01	-7.97	0.00	0.00
	195	0.00	0.00	-282.02	-9.90	0.00	0.00
15 Fx- Fz+ My+	196	0.00	0.00	-7.56	0.00	0.00	0.00
	197	-1.01	0.00	-6.55	0.00	0.19	0.00
	198	-11.03	0.00	-6.55	0.00	0.19	0.00
	199	-21.36	0.00	-6.55	0.00	0.19	0.00
	200	-31.37	0.00	-6.55	0.00	0.19	0.00
	201	-41.38	0.00	-6.55	0.00	0.19	0.00
	202	-51.39	0.00	3.46	0.00	2.12	0.00
	203	-61.39	0.00	8.51	0.00	3.08	0.00
	204	-71.40	0.00	13.55	0.00	4.05	0.00
	205	-81.41	0.00	18.59	0.00	5.02	0.00
	206	-91.42	0.00	23.63	0.00	5.99	0.00
	207	-101.42	0.00	33.63	0.00	7.91	0.00

Load Case	No.	Fx [N]	Fy [N]	Fz [N]	Mx [Nm]	My [Nm]	Mz [Nm]
16 Fx- Fz- My-	208	0.00	0.00	-7.56	0.00	0.00	0.00
	209	-1.01	0.00	-8.58	0.00	-0.19	0.00
	210	-11.03	0.00	-8.58	0.00	-0.19	0.00
	211	-21.36	0.00	-8.58	0.00	-0.19	0.00
	212	-31.37	0.00	-8.58	0.00	-0.19	0.00
	213	-41.38	0.00	-8.58	0.00	-0.19	0.00
	214	-51.39	0.00	-18.58	0.00	-2.12	0.00
	215	-61.39	0.00	-23.63	0.00	-3.08	0.00
	216	-71.40	0.00	-28.67	0.00	-4.05	0.00
	217	-81.41	0.00	-33.71	0.00	-5.02	0.00
	218	-91.42	0.00	-38.75	0.00	-5.99	0.00
	219	-101.42	0.00	-48.76	0.00	-7.91	0.00
17 Fx- Fz- My+	220	0.00	0.00	-7.56	0.00	0.00	0.00
	221	-5.00	0.00	-10.56	0.00	0.19	0.00
	222	-25.02	0.00	-51.25	0.00	0.08	0.00
	223	-45.03	0.00	-95.92	0.00	1.04	0.00
	224	-55.04	0.00	-140.97	0.00	2.01	0.00
	225	-65.05	0.00	-186.03	0.00	2.97	0.00
	226	-68.03	0.00	-231.09	0.00	3.94	0.00
	227	-71.01	0.00	-236.10	0.00	4.90	0.00
	228	-73.99	0.00	-241.10	0.00	5.86	0.00
	229	-76.96	0.00	-246.10	0.00	6.83	0.00
	230	-86.97	0.00	-251.11	0.00	7.79	0.00
18 Fx- Fz- My-	231	0.00	0.00	-7.56	0.00	0.00	0.00
	232	-5.00	0.00	-10.56	0.00	-0.19	0.00
	233	-25.02	0.00	-51.25	0.00	-0.08	0.00
	234	-45.03	0.00	-95.92	0.00	-1.04	0.00
	235	-55.04	0.00	-140.97	0.00	-2.01	0.00
	236	-65.05	0.00	-186.03	0.00	-2.97	0.00
	237	-68.03	0.00	-231.09	0.00	-3.94	0.00
	238	-71.01	0.00	-236.10	0.00	-4.90	0.00
	239	-73.99	0.00	-241.10	0.00	-5.86	0.00
	240	-76.96	0.00	-246.10	0.00	-6.83	0.00
	241	-86.97	0.00	-251.11	0.00	-7.79	0.00
19 Fx- Fz-	242	0.00	0.00	-7.56	0.00	0.00	0.00
	243	-0.97	0.00	-9.59	0.00	0.00	0.00
	244	-0.97	0.00	-49.62	0.00	0.00	0.00
	245	-0.97	0.00	-89.62	0.00	0.00	0.00
	246	-0.97	0.00	-129.63	0.00	0.00	0.00
	247	-0.97	0.00	-169.65	0.00	0.00	0.00
	248	-0.97	0.00	-189.66	0.00	0.00	0.00
	249	-20.98	0.00	-189.66	0.00	0.00	0.00
	250	-40.99	0.00	-189.66	0.00	0.00	0.00
	251	-50.99	0.00	-189.66	0.00	0.00	0.00
	252	-61.00	0.00	-189.66	0.00	0.00	0.00
	253	-71.01	0.00	-189.66	0.00	0.00	0.00
	254	-81.02	0.00	-189.66	0.00	0.00	0.00
	255	-91.03	0.00	-189.66	0.00	0.00	0.00
20 Fx- Fz-	256	0.00	0.00	-7.56	0.00	0.00	0.00
	257	-0.97	0.00	-9.59	0.00	0.00	0.00
	258	-0.97	0.00	-89.62	0.00	0.00	0.00
	259	-0.97	0.00	-169.65	0.00	0.00	0.00
	260	-0.97	0.00	-189.66	0.00	0.00	0.00
	261	-0.97	0.00	-229.68	0.00	0.00	0.00
	262	-40.99	0.00	-229.68	0.00	0.00	0.00
	263	-50.99	0.00	-229.68	0.00	0.00	0.00
	264	-61.00	0.00	-229.68	0.00	0.00	0.00
	265	-71.01	0.00	-229.68	0.00	0.00	0.00
	266	-81.02	0.00	-229.68	0.00	0.00	0.00
	267	-91.03	0.00	-229.68	0.00	0.00	0.00

Figure C.3: Balance calibration load cases.

Appendix D

Sensors Specifications

D.1 Model 1750 Constant Temperature Anemometer

The Model 1750 Constant Temperature Anemometer does not include a signal conditioner, its specifications are presented in Tab. D.1.

Table D.1: Model 1750 Constant Temperature Anemometer specifications.

Specifications	
Input power	+ 15VDC $\pm$ 10%, 250 m/A
Output range	-12 VDC to +12 VDC, BNC output or terminal strip
Sensor current	Up to 2 mA
Gain	Continuous from 50 to 1000
Frequency response	Up to 1 kHz

Further specifications can be accessed at *TSI Incorporated*® [53].

D.2 Pressure Sensor - *Schlumberger*®

D.2.1 Pressure Sensor Specifications

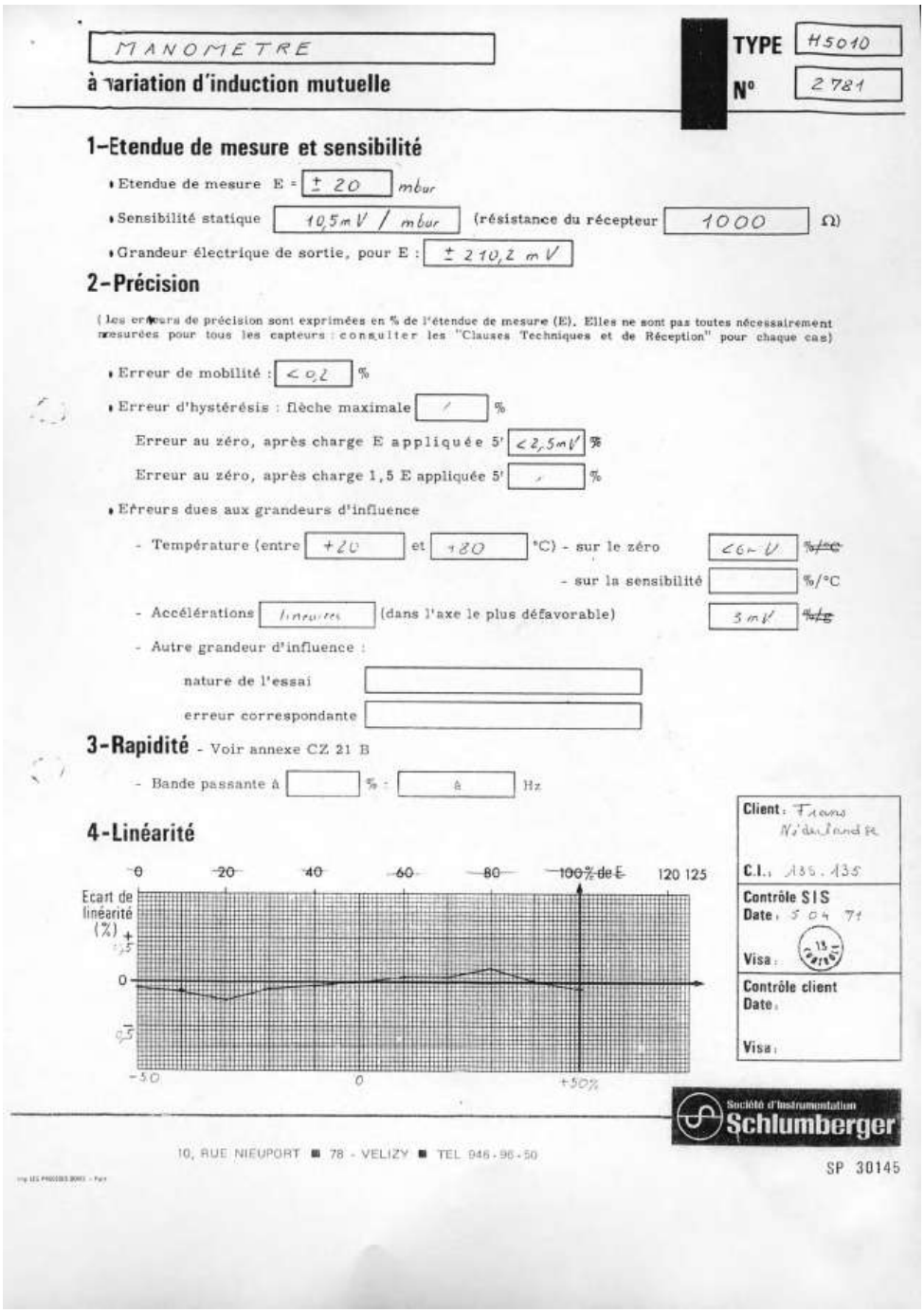

MANOMETRE

à variation d'induction mutuelle

TYPE H5010

N° 2781

1-Etendue de mesure et sensibilité

- Etendue de mesure E = ± 20 mbar
- Sensibilité statique 10,5 mV / mbar (résistance du récepteur 1000 Ω)
- Grandeur électrique de sortie, pour E : ± 210,2 mV

2-Précision

(Les erreurs de précision sont exprimées en % de l'étendue de mesure (E). Elles ne sont pas toutes nécessairement mesurées pour tous les capteurs : consulter les "Clauses Techniques et de Réception" pour chaque cas)

- Erreur de mobilité : < 0,2 %
- Erreur d'hystérésis : flèche maximale / %

Erreur au zéro, après charge E appliquée 5' < 2,5 mV %

Erreur au zéro, après charge 1,5 E appliquée 5' / %

- Erreurs dues aux grandeurs d'influence

- Température (entre +20 et +80 °C) - sur le zéro < 6 mV ~~%/°C~~

- sur la sensibilité %/°C

- Accélérations linéaires (dans l'axe le plus défavorable) 5 mV ~~%/g~~

- Autre grandeur d'influence :

nature de l'essai

erreur correspondante

3-Rapidité - Voir annexe CZ 21 B

- Bande passante à % : à Hz

4-Linéarité

Client : Fiens N'de Land Pt

C.I. : 135.135

Contrôle SIS

Date : 5 04 71

Visa :

Contrôle client

Date :

Visa :

Société d'Instrumentation Schlumberger

10, RUE NIEUPORT ■ 78 - VELIZY ■ TEL 946-96-50

SP 30145

Figure D.1: Pressure sensor specifications.

D.2.2 Pressure Sensor Signal Conditioner Specifications

Société d'Instrumentation Schlumberger

CEDEX 38
75 - PARIS BRUNE - tél. 735.31.40

NOTE D'INFORMATION TECHNIQUE

NIT	724	Juin 1969 EDITION 3	D
AUXILIAIRE pour un capteur à variation de mutuelle induction MISE EN SERVICE Association avec enregistreurs			D5484
CONSTRUCTEUR SOCIETE D'INSTRUMENTATION SCHLUMBERGER			A1322 A1500 A0300 A0303 A 4660

FONCTION

Elément embarquable groupant tous les circuits nécessaires à l'emploi d'un capteur à mutuelle induction variable (alimentation, démodulation, amplification et filtrage).
Il comporte :

- Un GENERATEUR électronique 1000 Hz fonctionnant à partir du réseau 27 V.
Puissance : 1 VA
Tension de sortie : 22 V, 1000 Hz à faible taux d'harmoniques.
- Un DEMODULATEUR à diodes suivi d'un FILTRE et d'un AMPLIFICATEUR à sensibilité réglable par valeurs discrètes de coefficients 1/2, 1, 2 et 4.

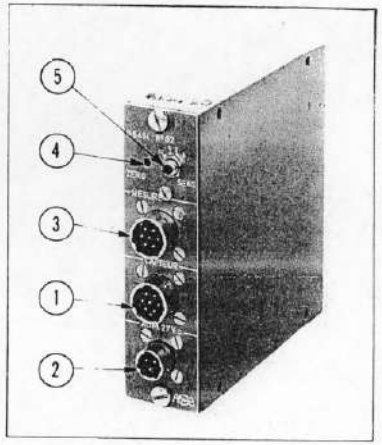

CARACTERISTIQUES

(Voir fiche technique DD - 049)

2 niveaux de sortie (A et B)

- A : sortie sur récepteur haute impédance pour télémesure ou enregistrement magnétique (les impédances internes correspondant aux 4 positions du commutateur de sensibilité sont respectivement) :

Position commutateur de sensibilité	Impédance interne
1/2	8 Ω
1	15 Ω
2	30 Ω
4	50 Ω

- B : sortie sur récepteur basse impédance pour enregistrement photographique (impédance interne 3350 Ω $\mp^{9}_{50}$ Ω)

Niveaux de sortie

Suivant type de capteur associé :
Niveaux maximaux :
- Configuration A : ± 1 V (capteurs symétriques) ou 0 à 1 V (capteurs asymétriques) sur 50 000 Ω.
- Configuration B : ± 250 μA ou 0 à 500 μA sur 650 Ω.

Niveaux pour capteurs à sortie normalisée :
- Configuration A : ± 840 mV ou 0 à 1680 mV sur 50 000 Ω
- Configuration B : ± 210 μA ou 0 à 420 μA sur 650 Ω

Bande passante à 10 %

0 à 200 Hz

MISE EN SERVICE

RACCORDEMENT (schéma ci-contre)

Capteur

Fiche Jaeger miniature 7 broches
réf. 530 272 (1)
Primaire : 1 et 2
Premier secondaire : 5 et 6
Deuxième secondaire : 3 et 4
Masse : 7

Alimentation

Raccordement au réseau 27 V par fiche Jaeger miniature 3 broches
réf. 530 232 (2)
0 V : broche 2
+ 27 V : broche 1

Sortie mesure

Fiche Jaeger miniature 7 broches
réf. 530 272 (3)
Configuration A : 3 et 5 ou 6
Configuration B : 4 et 5 ou 6

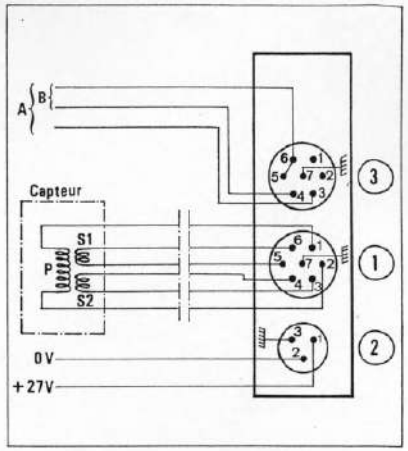

REGLAGES

Réglage du zéro

Le zéro du capteur est réglé au niveau du démodulateur incorporé à l'élément D 5484 par le potentiomètre④ accessible en face avant par fente tournevis (largeur maximale de la lame : 2,5 mm).
Latitude de réglage au gain 1 : ± 25 % de l'étendue de mesure du capteur (Tolérance : ± 5 %)

Emploi du commutateur de sensibilité (5)

Il comporte 4 positions repérées 1/2, 1, 2 et 4. Chaque position correspond à l'exploitation d'une fraction de l'étendue de mesure nominale du capteur repérée dans le tableau ci-dessous :

Position du commutateur	Fraction de l'étendue de mesure
1/2	2
1	1
2	0,5
4	0,25

La position 1/2 est utilisable dans tous les cas où les caractéristiques mécaniques de l'organe détecteur du capteur le permettent (voir fiches techniques individuelles). L'écart de linéarité du capteur utilisé dans ces conditions n'est généralement pas modifié.
Sur les positions 2 et 4 les erreurs de précision indiquées dans les fiches techniques des capteurs sont conservées. Toutefois, il ne faut pas perdre de vue qu'elles sont en valeur absolue ramenées à la plage de mesure considérée.
Exemple : H 5112 (0 à 4 mbar)

- L'influence d'une variation de température du capteur égale à 20°C se traduira par une dérive de zéro égale à : 0,4 % de la déviation du récepteur en position 1 (erreur : 2.10^{-4}/°C) et 1,6 % de la déviation du récepteur en position 4.
- Par contre, l'hystérésis se traduira par une variation plus faible de la déviation en position 4 (contrainte plus faible des membranes).

UTILISATION DE LA SORTIE A (haute impédance)

TELEMESURE OU ENREGISTREMENT MAGNETIQUE

On donne ci-dessous l'exemple de l'utilisation d'une chaîne comprenant un élément D 5484 avec sortie sur enregistreur magnétique A 4660 en modulation de fréquence.

Raccordement

Par fils 2 conducteurs blindés
Assurer les liaisons suivantes

	Sortie mesure D 5484 (3)	Enregistreur A 4660
Type d'embase	Jaeger miniature 7 broches réf. 533 273	Radiall BR 51 180 (étanche) ou BR 51 000 (non étanche)
Type de fiche mobile livrée	Jaeger miniature 7 broches ref. 530 371 avec serre-câble	Radiall BR 51 010
Raccordement	3	Point haut
	5 ou 6	Masse enregistreur (2e plot)
	Blindage à la masse des prises	

Configurations d'enregistrement utilisables

Vitesse minimale : 4,75 cm/s (bande passante : 0 à 625 Hz - fréquence centrale : 3375 Hz).
Vitesse normale d'utilisation : 9,5 cm/s (bande passante : 0 à 1250 Hz - fréquence centrale : 6750 Hz)
Vitesses supérieures utilisables.

UTILISATION DE LA SORTIE B (basse impédance)

LECTURE DIRECTE OU ENREGISTREMENT

Dans le tableau suivant est indiquée la fraction de l'étendue de mesure correspondant à la déviation normale de l'oscillographe. Elle correspond à une chaîne dont le capteur est à sortie normalisée et à un oscillographe de sensibilité nominale.

Utilisation d'un oscillographe type E 60, E 61, E 62 ou E 63

Bande passante : 0 à 80 Hz, résistance interne 650 Ω
L'oscillographe est raccordé directement à la sortie B.

Enregistreur	Déviation	Oscillographe	Commutateur de l'élément D 5484			
			1	2	4	1/2
A 1322	±40 mm	E 60	1,2	0,6	0,3	
A 1500	±26 mm	E 62	1,6	0,8	0,4	
A 0300 (U1)	±18 mm	E 61	1,6	0,8	0,4	
A 0300 (U2)	±36 mm	E 60	1,6	0,8	0,4	
A 0300 (U4A)	±72 mm	E 63	1	0,5	0,25	2
			Fraction de l'étendue de mesure du capteur			

Exemple : Capteur J 2230 - étendue de mesure : 0 à 120 m/s² associé à un oscillographe E 6011 (enregistreur A 1322).
La déviation sera 80 mm pour 0 à 36 m/s² en position 4 du commutateur de l'élément D 5484.

AUTRES ASSOCIATIONS REALISABLES

Les configurations d'utilisation décrites plus haut correspondent à l'emploi normal de l'élément D 5484. Toutefois, la faible résistance interne et la puissance disponible à la sortie permettent son utilisation dans d'autres conditions. Dans certains cas, l'emploi de la sortie A (haute impédance) pour l'enregistrement photographique permet d'obtenir un gain supplémentaire avec les oscillographes E 6 de bande passante 0 à 80 Hz. D'autre part, des oscillographes à bande passante plus élevée peuvent être utilisés (oscillographes «crayon» de bande passante 0 à 200 Hz).
Dans tous les cas, une adaptation simple des oscillographes à la sortie de l'élément D 5484 est nécessaire.

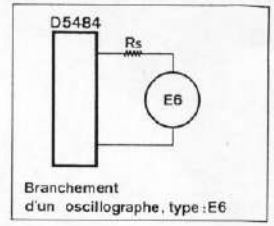

Branchement d'un oscillographe, type : E6

Dans les tableaux suivants (utilisation des oscillographes E 6 et SMI), on donne la fraction de l'étendue de mesure correspondant à la déviation normale de l'oscillographe pour une chaîne dont le capteur est à sensibilité normalisée et à un oscillographe de sensibilité nominale.

Utilisation des oscillographes E 6 sur la sortie A (haute impédance).

RESISTANCE INTERNE (Ω)	BANDE PASSANTE (Hz)	A 1322 E 60 : ±40 mm					A 1500 E 62 : ±26 mm					A 0300 (U1) E 61 : ±18 mm					A 0300 (U2) E 60 : ±36 mm					A 0300 (U4A) E 63 : ±72 mm				
		Rs (Ω)	POSITION DU COMMUTATEUR D5484				Rs (Ω)	POSITION DU COMMUTATEUR D5484				Rs (Ω)	POSITION DU COMMUTATEUR D5484				Rs (Ω)	POSITION DU COMMUTATEUR D5484				Rs (Ω)	POSITION DU COMMUTATEUR D5484			
			1	2	4	1/2		1	2	4	1/2		1	2	4	1/2		1	2	4	1/2		1	2	4	1/2
650	0 à 80	2700	1	0,5	0,25	2	2000	1	0,5	0,25	2	2000	1	0,5	0,25	2	2000	1	0,5	0,25	2	3200	1	0,5	0,25	2
3000	0 à 80	400	0,5	0,25	0,125	1	2000	1	0,5	0,25	2	2000	1	0,5	0,25	2	2000	1	0,5	0,25	2	1600	0,5	0,25	0,125	1
10 000	0 à 80	3300	1	0,5	0,25	2	100	1	0,5	0,25	2	100	1	0,5	0,25	2	100	1	0,5	0,25	2	5000	1	0,5	0,25	2

Exemple : Capteur J 2230 - étendue de mesure : 0 à 120 m/s² associé à un oscillographe E 6012 (enregistreur A 1322, résistance interne 3000 Ω, bande passante 0 à 80 Hz).
La déviation sera 80 mm pour 0 à 15 m/s² en position 4 du commutateur de l'élément D 5484, la résistance série étant 400 Ω.

Utilisation des oscillographes «crayon» type P

Leur bande passante est 0 à 200 Hz et leur résistance interne 115 Ω. L'oscillographe est shunté par 250 Ω et une résistance Rs est en série avec l'oscillographe shunté. Les fractions de l'étendue de mesure obtenues pour la déviation nominale sont données dans le tableau ci-dessous. Les déviations correspondantes sont :

. ± 35 mm (ou 0 à 70 mm) dans l'enregistreur A 0300
. ± 50 mm (ou 0 à 100 mm) dans l'enregistreur A 0303

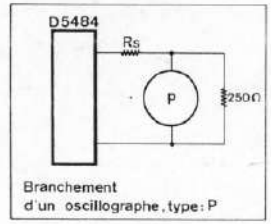

Branchement d'un oscillographe, type : P

Sortie D 5484	Rs (Ω)	Position commutateur D 5484			
		1	2	4	1/2
A Haute impédance	2000	0,4	0,2	0,1	0,8
B Basse impédance	750	0,8	0,4	0,2	1,6

Appendix E

CFD Mesh

StarCCM+® *surface wrapper* provides a clean geometry for meshing. Figure E.1 illustrates some surfaces after the *surface wrapper* feature being applied.

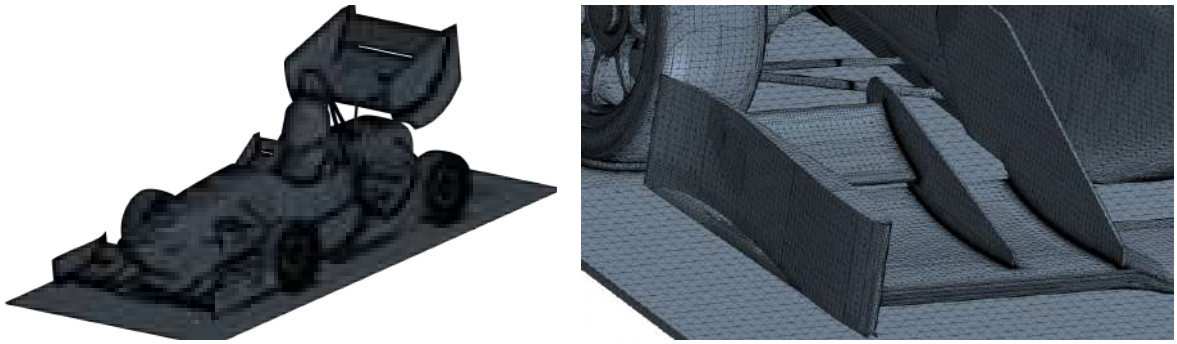

(a) Car (b) Front Wing and Wheel

Figure E.1: *Surface wrapper* Feature.

Figures E.2 show the surface mesh of the front wing, front tyres and rear wing.

(a) Front Wing and tyres. (b) Rear Wing.

Figure E.2: Surface mesh.

Appendix F

Balance Structural Integrity

Figure F.1 presents the points were the minimum and maximum stress was detected through the numerical model.

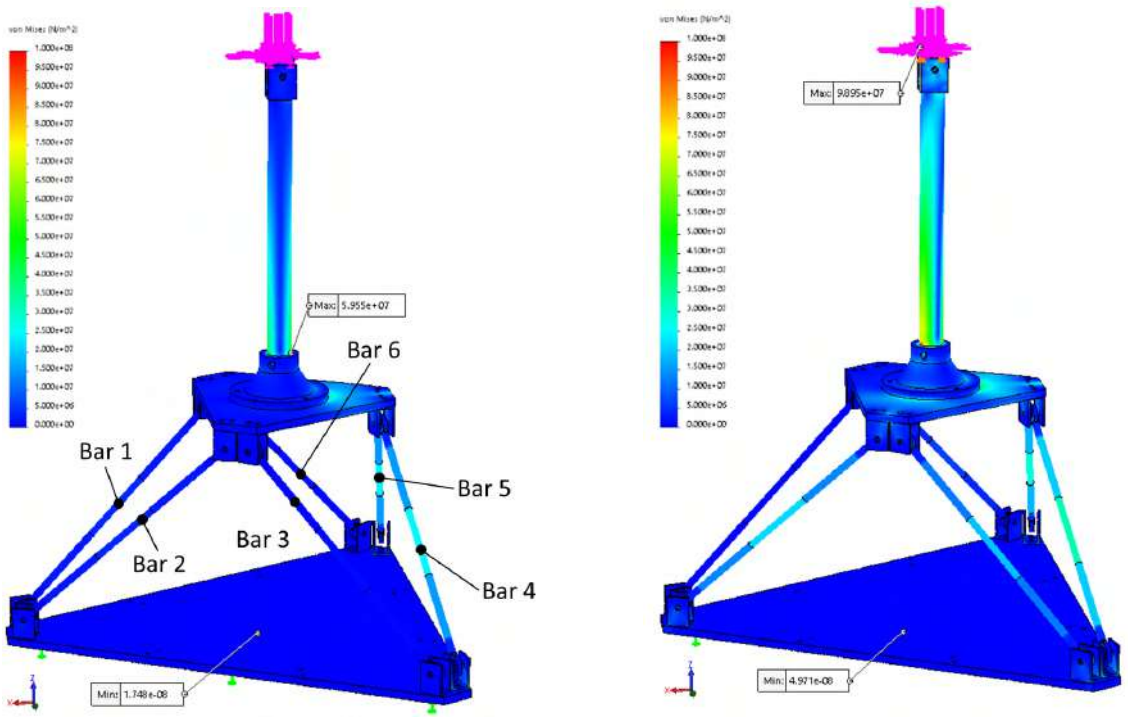

(a) Straight condition.

(b) Straight with lateral wind condition.

Figure F.1: Aerodynamic balance von mises stress.

Appendix G

Model Manufacturing Processes

G.1 CNC Machining

Figure G.1 describes the features of the CNC *InoCONTROL*® sofware.

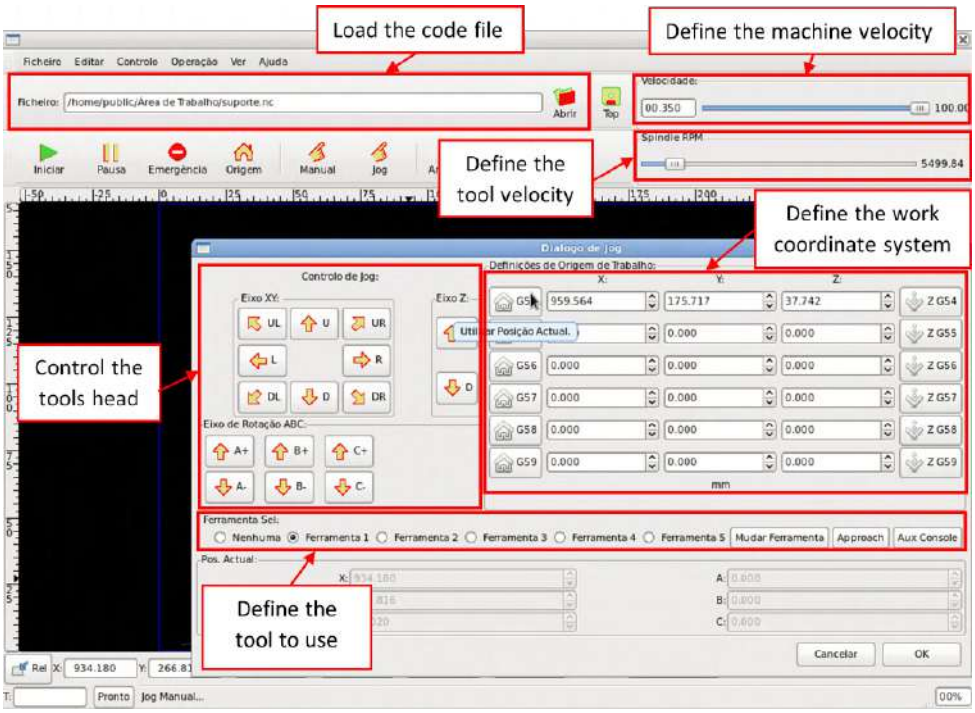

Figure G.1: *InoCONTROL*® sofware - CNC control software.

G.2 3D Print

Figure G.2 presents the user interface of the open source *Ultimaker Cura*™ (v.4.8.0) software.

Table G.1 presents the two different print profiles, aerodynamic components (Aero) and monocoque (Mono), used to manufacture the model.

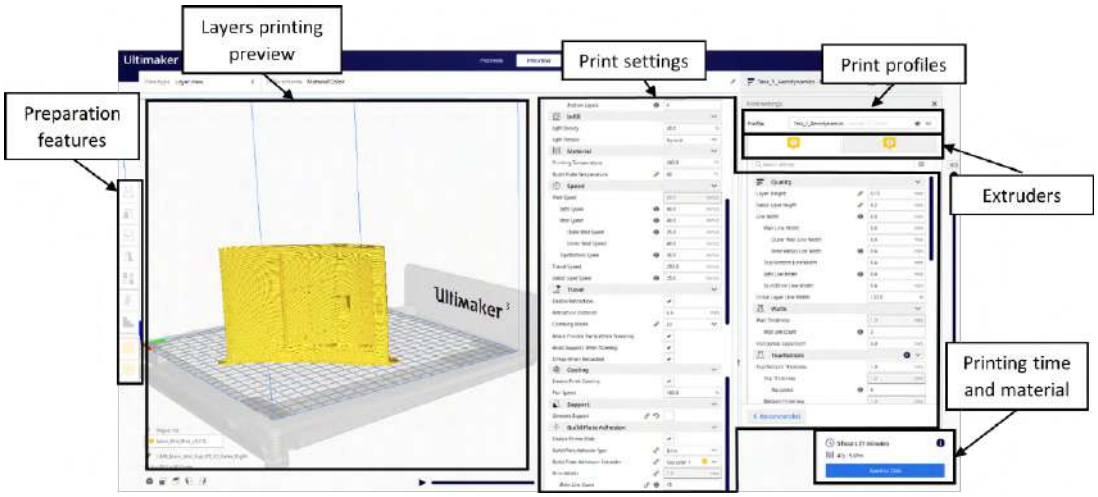

Figure G.2: *Ultimaker Cura*™ (v.4.8.0) - printing preparation.

Table G.1: 3D printing settings.

Print settings		Print profile		Units
		Aero	Mono	
Quality	Layer height	0.15	0.2 mm	
	Initial layer height	0.2	0.27	mm
	Wall line width	0.4	0.4	mm
	Infill line width	0.4	0.4	mm
Walls	Wall line count	3	3	
Top/Bottom	Top and bottom layers	4	3	
Infill	Type	Gyroid	Gyroid	
	Sparse density	20	15	
Speed	Print	60	60	$m\,s^{-1}$
	infill	40	50	$m\,s^{-1}$
	Outer wall	35	45	$m\,s^{-1}$
	Inner wall	40	45	$m\,s^{-1}$
	Top/Bottom	30	35	$m\,s^{-1}$
	Support	40	50	$m\,s^{-1}$
	Initial layer	25	25	$m\,s^{-1}$
Support	Structure	Tree	Tree	
	Brim line count	15	20	
	Support interface	Enable	Enable	
	Support roof	Enable	Enable	
	Top distance	0.1	0.1	mm
	Z distance	0.1	0.1	mm
Travel	Avoid supports	Enable	Enable	
Build plate adhesion	Type	Brim	Brim	
	Brim line count	40	50	